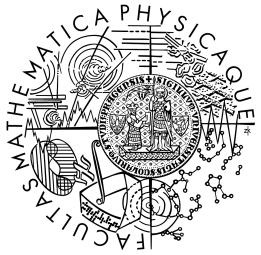

FACULTY
OF MATHEMATICS
AND PHYSICS
Charles University

## DOCTORAL THESIS

Kryštof Březina

# *Ab initio* and path integral molecular dynamics methodology for hydrogen-bonded systems in the condensed phase

Institute of Physics of Charles University

Supervisor of the doctoral thesis: RNDr. Ondřej Maršálek, Ph.D.
Advisor of the doctoral thesis: prof. Mgr. Pavel Jungwirth, CSc., DSc.
Study programme: Biophysics, chemical and macromolecular physics

Prague 2024

I declare that I carried out this doctoral thesis independently, and only with the cited sources, literature and other professional sources. It has not been used to obtain another or the same degree.

I understand that my work relates to the rights and obligations under the Act No. 121/2000 Sb., the Copyright Act, as amended, in particular the fact that the Charles University has the right to conclude a license agreement on the use of this work as a school work pursuant to Section 60 subsection 1 of the Copyright Act.

In Prague on March 20, 2024 .....

Author's signature

*„Už dnes se máme líp než zítra... pozítří... včera—no včera jsi to říkal, předsedo, ne?!“* is one of my favorite (and difficult to translate fully) Czech movie quotes and also a one that is quite fitting to convey the sentiment of excitement of not only being able to witness but also to contribute to an ever-developing field. I want to dedicate this work to everyone who contributed to making me the person I am today, professionally and personally. Namely, I would like to thank my supervisor, Ondřej, and my co-supervisor, Pavel, for their endless support, stimulating discussions, and, most importantly, for showing me what being a scientist means beyond classroom doors.

Title: *Ab initio* and path integral molecular dynamics methodology for hydrogen-bonded systems in the condensed phase

Author: Kryštof Březina

Institute: Institute of Physics of Charles University

Supervisor: RNDr. Ondřej Maršálek, Ph.D., Institute of Physics of Charles University

Abstract: *Ab initio* molecular dynamics simulations with imaginary-time path integral representation of atomic nuclei provide valuable insight into the physics and chemistry of condensed-phase hydrogen-bonded molecular systems at a high level of descriptive accuracy. At the same time, such simulations often represent a methodological and computational challenge, especially once advanced electronic structure theories are required. In this work, we present our contributions to integrating machine learning potentials into the simulation workflow, focusing on employing active learning in the training set selection and on an efficient generation of the training geometries themselves. With this methodology, we performed advanced simulations of three different molecular systems. First, we explored the behavior of the benzene radical anion dissolved in liquid ammonia: a system with pertinence to Birch reduction chemistry. Motivated by our findings, we then performed an extensive study of $\pi$-hydrogen bonding in solutions of benzene liquid water and liquid ammonia with a particular focus on structure, dynamics, and vibrational spectroscopy. Finally, we transferred to surface physics to model proton-transfer reactions in nitrogen-based benzoquinone derivatives in the gas phase and on a gold surface and to describe the reactivity-defining role of nuclear quantum effects. The research is contained in five publications attached to this thesis.

Keywords: *ab initio* molecular dynamics, imaginary-time path integrals, density-functional theory, machine learning potentials, hydrogen bonds, condensed phase, chemical reactivity

Název práce: Metodika *ab initio* a dráhově integrální molekulární dynamiky pro vodíkově vázané systémy v kondenzované fázi

Autor: Kryštof Březina

Ústav: Fyzikální ústav Univerzity Karlovy

Školitel: RNDr. Ondřej Maršálek, Ph.D., Fyzikální ústav Univerzity Karlovy

Abstrakt: Simulace *ab initio* molekulární dynamiky s atomovými jádry reprezentovanými dráhovými integrály v imaginárním čase poskytují cenný vhled do fyziky a chemie kondenzovaných vodíkově vázaných systémů na vysoké úrovni přesnosti popisu. Zároveň tyto simulace představují metodologickou a výpočetní výzvu zejména v případě, kdy jsou vyžadovány pokročilé metody teorie elektronové struktury. V této práci ukazujeme naše příspěvky ohledně začlenění potenciálů na bázi strojového učení do simulačních postupů s důrazem na použití aktivního učení pro tvorbu tréninkové sady a na efetivní generaci tréninkových geometrií samotných. S touto metodologií jsme provedli pokročilé simulace tří různých molekulárních systémů. Jako první jsme prozkoumali chování radikál-aniontu benzenu rozpuštěného v kapalném amoniaku: tento systém je významný v kontextu chemie Birchovy redukce. Motivováni našimi zjistěními jsme pokračovali rozsáhlou studií $\pi$-vodíkových vazeb v roztocích benzenu v kapalné vodě a amoniaku s důrazem na strukturu, dynamiku a vibrační spektroskopii. Nakonec jsme se přesunuli do oblasti fyziky povrchů, kde jsme se věnovali modelování reakcí s přenosem protonu v dusíkatých derivátech benzochinonu v plynné fázi a na povrchu zlata a popisu klíčové role jaderných kvantových jevů pro tuto reaktivitu. Provedený výzkum je obsažen v pěti publikacích přiložených k této práci.

Klíčová slova: *ab initio* molekulární dynamika, dráhové integrály v imaginárním čase, teorie funkcionálu hustoty, potenciály na bázi strojového učení, vodíkové vazby, kondenzovaná fáze, chemická reaktivita

# Contents

# 1 | Introduction

This thesis summarizes and discusses the main results of the research conducted between 2019 – 2024 during the time of my doctoral studies at the Institute of Physics of Charles University under the supervision of Dr. Ondřej Maršálek. The research is based on simulations of *ab initio* molecular dynamics (AIMD) of hydrogen-bonded systems. It consists of a part focusing on developing and advancing computational methods, and another part, where we model and study specific molecular systems overarched by the common theme of hydrogen bonding. The studied systems mainly include liquids and solutions, but we also touch on surface-bound and gas-phase systems.

The ensuing preamble in the rest of Chapter 1 provides a general overview of the physical and computational context of the work as well as an introduction to the specific research projects that will be discussed in the following Chapters. Chapter 2 summarizes the employed theory and methodology. Chapters 3–6 focus on the scientific results, and finally, Chapter 7 concludes the thesis.

## 1.1 | Hydrogen bonds as a key phenomenon in nature

The official definition of the hydrogen bond by the International Union of Pure and Applied Chemistry states that *"The hydrogen bond is an attractive interaction between a hydrogen atom from a molecule or a molecular fragment X–H in which X is more electronegative than H, and an atom or a group of atoms in the same or a different molecule, in which there is evidence of bond formation"*.[1] Since the phenomenon of hydrogen bonding is the common denominator connecting all the research projects discussed in this work, it makes sense to open the discussion by breaking this definition down and explaining the key terminology. First of all, it is worth noting that the definition is rather general and allows essentially any oriented interaction between a polarized $X^{\delta-}$–$H^{\delta+}$ bond (called the *donor*), which exhibits a localization of positive charge on the hydrogen atom, and any arbitrary group of atoms (called the *acceptor*) to pass as a hydrogen bond. This general formulation is needed to cover certain exotic cases (as we will witness, for example, in Chapter 5 that focuses on $\pi$-hydrogen bonding); however, in practice, the term hydrogen bond is typically reserved more selectively for interactions of the type X–H $\cdots$ X', where X and X' represent either nitrogen, oxygen or a fluorine atom, possibly embedded in a larger molecular structure (as an example, the hydrogen bond network in liquid water is shown in Figure 1.1). In those

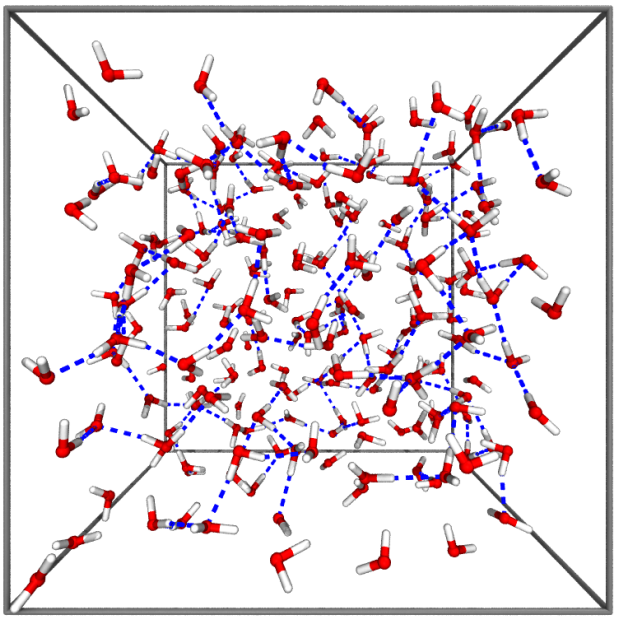

Figure 1.1: A snapshot from an AIMD simulation of liquid water sample at 300 K with instantaneous hydrogen bonds, determined by predefined, fixed criteria on H$\cdots$O' distances and O–H$\cdots$O' angles, shown in blue dashed lines. Periodic boundary conditions (see Chapter 2 for details) apply at the box faces.

cases, the polarization of the donor molecule is strong enough that the bond formation is dominated by polarizable electrostatics, which sets it apart from weaker dispersion interactions that arise due to instantaneous charge fluctuations only.[2] However, more subtle effects like dispersion[3,4] and charge transfer[5] across the hydrogen bond remain important ingredients to the full picture.

Without exaggeration, one can say that with no hydrogen bonding, there would be no life as we know it on Earth since this quintessential non-covalent interaction is present in nearly all materials that constitute a living organism and in many other materials that surround us on a daily basis. Indeed, hydrogen bonds are crucial for the structure of biopolymers,[6] notably in the formation and stability of the secondary, tertiary, and quaternary structures of proteins and the structure of the double-stranded DNA helix. As such, they have fundamental implications for vitally important processes such as biosignaling, enzymatic catalysis, cellular replication, and pharmaceutics binding, to name a few. Outside of the biological context, hydrogen bonds give properties to numerous common and important solid materials, including various molecular crystals[7] and piezoelectrics,[8] polymers such as cellulose[9] and nylon,[10] and inorganic zeolites[11] and also have a profound effect on the properties of liquids. For instance, they are the reason why water ($H_2O$) exists as a liquid at ambient conditions and has a

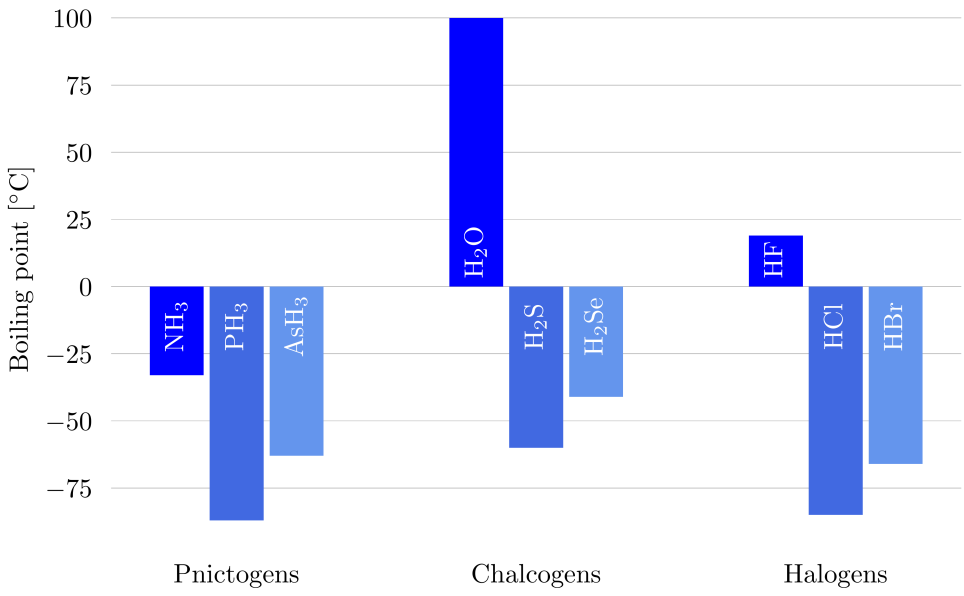


Figure 1.2: Boiling points of pnictogen (group V-A), chalcogen (group VI-A), and halogen (group VII-A) hydrides over periods 2–4.

boiling point as high as 100.0 °C despite its very low molar mass. Looking down the VI-A group of the periodic table, $H_2S$ does not form hydrogen bonds according to the above definition, has nearly double the molar mass of water, and has a boiling point of −59.5 °C. The effect on liquid water properties is spectacular and is a result of a constructive combination of a relatively high hydrogen bond strength and the number of hydrogen bonds that a water molecule can engage in at a time (this was estimated using indirect interpretation of experiments on average from 2.2 to 3.3 bonds per molecule[12,13] and using *ab initio* simulations from 3.61 to 3.77 bonds per molecule[14]) that hold the liquid together, but a similar effect is observed between liquid $NH_3$ and $PH_3$ with boiling points of −33.3 and −87.7 °C and HF and HCl with +19.5 and −85.0 °C, respectively. This effect, also additionally compared to the third-period hydrides that do not form hydrogen bonds and thus follow the expected trend of increasing boiling points, is shown in Figure 1.2.[15] Solvents with strong hydrogen bonds represent an important class with special properties owing to their highly polar character. This creates an ideal solution environment for polar and ionic species such as seen, for instance, in the cellular matrix, in seawater, and in numerous industrial and everyday applications.

Alongside the fundamental role of hydrogen bonds in soft matter structuring, they can be viewed as a useful probe into the quantum nature of the atomic nuclei in hydrogen-bonded systems. This is perhaps slightly in contrast with the traditional chemist's view of molecules as formed by quantum electrons orbiting around classical, point-like nuclei. However, quantum-mechanical effects,[16,17]

such as zero-point energy or quantum delocalization and tunneling, indeed represent an integral part of the behavior at the nuclear level, challenging the classical picture: this is most pronounced for hydrogen nuclei due to their light mass. Clearly, directly quantifying nuclear quantum effects (NQEs), defined as the deviation of the real, quantum-behaving system from its classical reference,[18] in an experimental setting is not possible because there is no experimentally available classical reference to compare to. Therefore, quantum effects are experimentally accessed indirectly using isotope substitution,[19,20] which changes the mass of an atomic nucleus, most often hydrogen. According to classical mechanics, this should not affect any thermodynamic properties, since they do not depend on mass, but it does affect them under the quantum description. A noteworthy manifestation of an isotope effect can be observed in the so-called Ubbelohde effect,[21,22] which refers to the change in the X–X' equilibrium distance upon deuteration of hydrogen-bonded molecular crystals and which has (classically forbidden) measurable implications for macroscopic thermodynamic properties such as phase behavior: for example, the differences in thermodynamic properties between $H_2O$ and $D_2O$ are measurable and well-known.[23] Still, the insight into the bare NQE origin of the effect must rely on theoretical methods, where the ability to model a quantum system implies the ability to model a simpler classical one. Using simulations of molecular dynamics (MD) for a wide pool of hydrogen-boned systems, the origin of the changes in the X–X' distance upon the inclusion of NQEs was explained by the principle of competing quantum effects[19,22,24] that affect both the stretching and bending motion in the hydrogen bond. The two quantum effects combine to a general result that causes classically strong hydrogen bonds to become stronger and weak ones to become weaker by the inclusion of NQEs, providing a non-trivial and system-specific overall behavior.[22] In general, due to the relatively large mass of nuclei, NQEs usually manifest as a correspondingly small perturbation to the classical picture, which is normally able to give a thorough understanding of the physics of most systems at close-to-ambient conditions. Interestingly, liquid water exhibits a large degree of cancellation between the competing quantum effects, which makes the total NQEs quite small, and the classical approximation comes close to the quantum reality.[25] The fine balance between this cancellation can be changed by modifying the environment or the thermodynamic state. However, NQEs become progressively more pronounced as the temperature is lowered, and their inclusion becomes critical at ultra-cold conditions both explicitly in molecular simulations and in interpreting experimental data.[26]

## 1.2 | Describing molecular systems *in silico*

There are numerous approaches to simulating a molecular system using computers in order to predict its physical properties. Describing the electronic structure of atoms and molecules at 0 K with clamped (*i.e.*, classical) nuclear configurations is the domain of quantum chemistry calculations,[2] which mainly give insight into electronic properties and only offer limited and approximate access to thermal nuclear effects building on the harmonic vibrational analysis. Ther-

mal motion of nuclei can be robustly included by studying thermal statistical ensembles of nuclear configurations at non-zero temperatures. Such simulations normally fall into two categories known as Monte Carlo (MC) and molecular dynamics (MD) simulations. Since these are not used in this work, we note only in passing that Markov-chain MC simulations[27] rely on a sequence of random moves of atoms that are accepted or rejected in a way that ensures that the desired ensemble is sampled. As such, MC simulations give robust convergence of thermodynamic properties but do not yield meaningful dynamical information due to their stochastic nature. In contrast, MD simulations build on dynamical equations of motion to achieve the same goal of sampling statistical ensembles, in principle yielding dynamical properties alongside correct static thermodynamics. Generally speaking, MD simulations are becoming extremely relevant as an *in silico* complement to various experimental methods in studying molecular systems. As a standalone tool, they possess predictive qualities that can give access to the computational estimate of experimentally available results. In tandem with experiments, they provide atomistic resolution and the possibility to identify individual phenomena that take place concurrently in the studied systems and of which the experiment typically only sees the overall effect. As such, they can be instrumental in interpreting and disentangling experimental results. This is especially true in the context of hydrogen-bonded systems where an indirect exploration through various spectroscopies only shows convoluted imprints of the effect of the hydrogen-bonded environment and a direct one by structure-mapping methods such as scanning tunneling microscopy (STM) or X-ray diffraction typically lacks the resolution to resolve the structure of individual hydrogen atoms.[28,29]

For this introduction, a brief context of the employed computational methodology is provided, while the detailed technical discussion is postponed to Chapter 2. In this work, we pick AIMD as the primary simulation method of choice. The name of MD in AIMD originates in the fact that such simulations use fundamental classical equations of motion to numerically propagate the atomic nuclei in a representative microscopic sample of the studied system at an atomistic resolution through time, given a differentiable many-body potential that describes the interactions and forces between the atomic nuclei.[27] Note that at this moment, the only way electrons come into the simulation is through this potential, often known as the potential energy (hyper)surface (PES). Methods of statistical mechanics are then applied to the obtained trajectory to extract static and dynamic properties. NQEs are typically not included by switching from using the classical description to a quantum one based on the Schrödinger equation and performing full quantum dynamics, but rather rely on the Feynman path integral formalism in imaginary time.[30] This approach is generally called path integral molecular dynamics (PIMD) and exploits a computationally tractable isomorphism between the full quantum system and an extended classical one.[31] The term *ab initio* (Latin for "from the beginning") then refers to the way electrons are treated in such simulations: AIMD uses a full quantum electronic structure calculation to describe the many-body potential under the framework of the Born–Oppenheimer approximation[32] and, therefore, keeps explicit electrons in the system at every

simulation step. This normally results in superior accuracy and flexibility of the simulations over predefined, empirical interaction PESs, otherwise known as force fields.[27] Since the repeated evaluation of *ab initio* energies and forces is computationally challenging for realistically big systems,[33] not every electronic structure method is suited for use in AIMD, and one must compromise between accuracy and computational cost. For this reason, most AIMD simulations are based on density functional theory (DFT),[34] which offers correlated electronic energies at a price lower or comparable to Hartree–Fock electronic structure. Since most density functionals, including those used in this work, describe the interaction between electrons at a local or a semilocal level, they cannot describe non-local dispersion interactions on their own. This is typically rectified by adding empirical dispersion corrections, making the method practical for condensed hydrogen-bonded systems without raising its cost beyond the affordable limits.

## 1.3 | Context and aims of this work

At this point, we turn our attention from the general framing to the four distinct research projects that constitute the body of this thesis. In the following subsections, each project will be introduced and discussed in the context of previous related research with the aim of situating it into a bigger picture.

### 1.3.1 Streamlining computational methodology

Recently, the world of AIMD simulations underwent a minor revolution when machine learning techniques were introduced to mitigate the computational requirements for the explicit quantum mechanical calculations in AIMD. In this work, we oftentimes rely on the so-called machine learning potentials,[35] specifically on Behler–Parrinello high-dimensional neural network potentials (NNPs),[36] to circumvent the part of the calculation where the electronic energy and forces are evaluated on the fly from nuclear configurations using standard quantum mechanics. The NNP, technically a type of an artificial neural network (NN),[37] acts as a flexible and accurate fit to the underlying *ab initio* structure-to-energy relationship, which allows us to run simulations at a fraction of the original computational cost while maintaining simulation accuracy. Of course, one cannot avoid *ab initio* calculations altogether: *ab initio* data is needed for the training (*i.e.*, fitting) of the NNP. However, this typically represents a much smaller number of energy evaluations than the one needed to converge statistics using traditional AIMD simulations. Consequently, the approach can be expected to offer a computational speed-up of several orders of magnitude. Employing NNPs, unprecedented length and time scales of simulations became available for routine use.[38]

A balanced and robust training set is a key ingredient to a highly accurate NNP. Still, an NNP approximates the reference PES, meaning that it will always be burdened by some degree of generalization error when predicting new output for previously unseen data. Having trained an NNP on a given training set, disregarding its quality for now, the predictive action of the NNP can be divided

into two regimes. First, in the interpolation regime, the NNP is required to predict outcomes on data that fall inside the subspace spanned by the original training set. In that situation, the predictions are expected to be reliable with low generalization errors unless a large part of the coverage by training points in the relevant subspace was initially missing. Outside of this subspace, NNPs must rely on extrapolation, which is typically accompanied by larger generalization errors due to the fact that the NNP has never seen similar data and "does not know" what the associated output should be. Ideally, during a simulation using NNPs, one wants to stay in the interpolation regime with good coverage of the underlying space. However, it was recently argued that in the high-dimensional space of molecular geometry inputs, the NNPs always rely on extrapolation in practice, since the probability that a new geometry will fall into the smallest polygon enclosing the training set, *i.e.*, the convex hull, gets increasingly smaller due to the curse of dimensionality.[39] Perhaps a better rationale in this case then is, loosely speaking, that the NNP can extrapolate but should not venture too far into the unknown.

In any case, achieving a well-balanced training set through optimizing the selection of training points from a wider candidate set to maximize the efficiency of the training process and the resulting accuracy is no simple task. While initially approached by simpler methods such as random point sampling[3] or farthest point sampling,[40] it is becoming more and more recognized these days that active learning methods, in which the model itself is used to screen for the next most relevant training point, offer finer control over the data selection and faster, robust convergence to high-accuracy models. This is enabled by assembling an ensemble of NNPs trained for the same purpose, known as a committee NNP (C-NNP).[41] Given that the individual committee members have some degree of variance among them (achieved either by training to subsets of the full training set or by providing different initial conditions at the entry to the training process), one can easily evaluate the standard deviation of the C-NNP prediction, known in our line of work as the committee disagreement.[42] This quantity can be used as a measure of the prediction quality of the models for a particular input: its value remains low when the model is predicting in a well-trained region but goes up when the members start to diverge as they move to an undertrained region or start heavily extrapolating. Alongside the disagreement, the average of the committee prediction is known to be a better estimate of the output than that of the individual NNPs, which also makes C-NNPs immediately useful at simulation run time.

In this work, we will discuss two publications that engage in the development of computational methodology related to NNPs. The first paper[43] introduces our C-NNPs workflow, which relies on committee disagreement to build an active learning procedure to generate the training set known as query by committee (QbC),[44,45] but also to monitor the quantity during simulation to control the generalization error and to use it to bias the system to stabilize it when extending the model to new, unexplored regions of the configuration space. To validate the model, we perform classical and path-integral MD simulations of liquid water with the obtained C-NNPs and discuss its performance. The second paper[46]

recognizes that having AIMD simulations as the traditional source of *ab initio* training data can be prohibitive in certain computationally demanding systems and suggests a new methodology, which we call transition tube sampling (TTS), that generates thermal training geometries using computationally much more affordable premises than AIMD and thus opens the door to systems that would be difficult to model otherwise, including systems with chemical reactions. The published work illustrates the initial application of TTS to obtain C-NNP models for several gas-phase molecules, including some with intramolecular hydrogen bonds, followed by inference simulations. Possible generalizations of the method into the condensed phase are discussed in Chapter 3, and first steps towards its realization for a surface-bound system is presented in Chapter 6.

### 1.3.2 Radical anions in hydrogen-bonded liquid environments

The origins of this research date back at least to the year 2015, when Mason and coworkers[47,48] set out to understand the chemistry behind the well-known dangerous explosions of alkali metals in liquid water. Using high-speed imaging and spectroscopic methods, they observed the formation of blue hydrated electrons after placing a drop of liquid NaK alloy on a water surface and identified the reason for the following explosion as electrostatic positive supercharging of the remaining metal drop, otherwise known as a Coulombic explosion. To eliminate the explosive behavior and thus to allow oneself to study the intriguing physical properties of solvated electrons as inherently quantum-behaving solutes, the aqueous environment can be exchanged for liquid ammonia, which leads to the formation of deep blue solutions of solvated electrons that exhibit long-term stability.[49–51]

To set the ground for a study of these systems, we first opted to explore the neat liquid ammonia solvent, employing a new experimental and computational strategy.[52] On the experimental front, the chosen method was liquid microjet X-ray photoelectron spectroscopy (XPS) due to its ability to provide a detailed insight into the electronic structure of liquids (for more insight into this experimental methodology, see the comment in Appendix B).[53–56] From the computational standpoint, we approached the issue using a combination of classical AIMD simulations using a semi-local density functional (this was before our group began to use NNPs on a regular basis) for the thermal sampling of both gas and liquid ammonia followed by a $G_0W_0$ correction[57] of the electronic structure to obtain physically meaningful electron binding energies (the need for $G_0W_0$ calculations over density functional theory orbital energies will be discussed in detail in Chapter 2). This provides the electronic density of states (EDOS), which can be directly compared to experimental XPS spectra, albeit with certain reservations that will be discussed in Chapter 4. The gas and liquid ammonia valence spectra obtained using this combination of methods are reported in Reference 52 and plotted for convenience in Figure 1.3. In the measured gas-phase XPS spectrum (Figure 1.3, top panel, blue), we can notice a distinct three-peak feature over the studied energy range that characterizes the three distinct electron binding

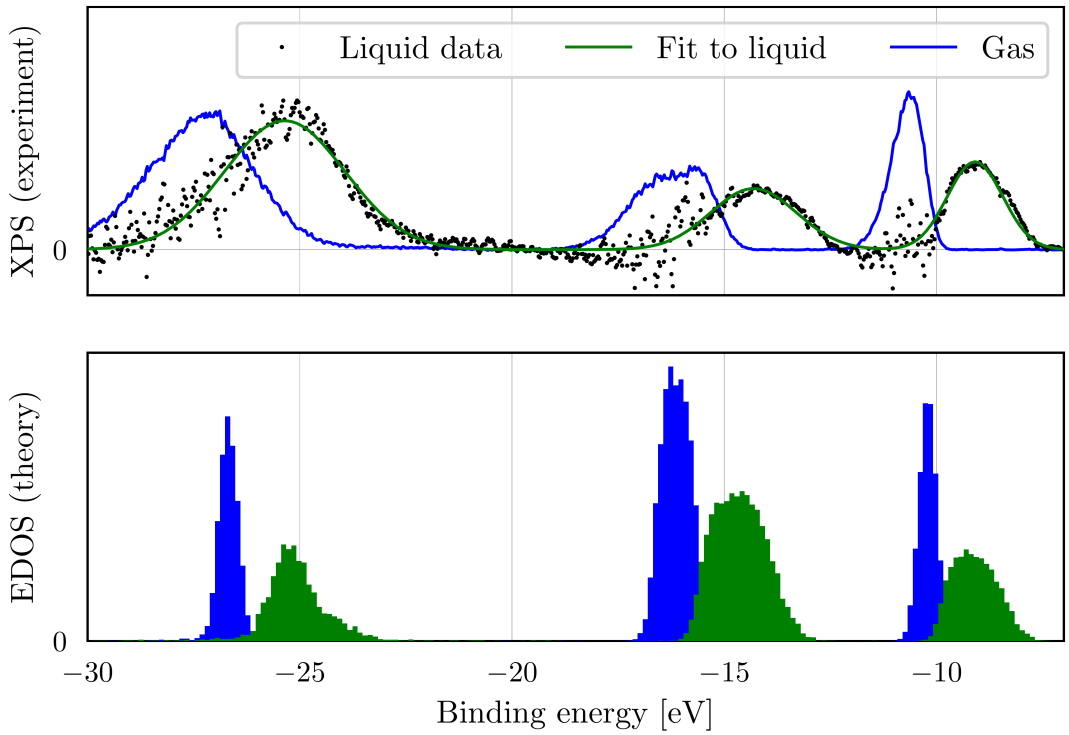


Figure 1.3: Gas and liquid ammonia XPS spectra and EDOS.[52] Top panel: Pure raw liquid-phase data (black points) spectra and their Gaussian fit (green) obtained by subtracting the gas-phase spectrum from the combined microjet gas-and-liquid spectrum. Bottom panel: calculated EDOS for gaseous and liquid ammonia.

energy levels in the ammonia molecule at approximately −11, −16 and −27 eV. Using simple molecular orbital theory, these levels can be connected to spatial orbitals with $3a_1$, $1e$, and $2a_1$ symmetries, which accommodate all 8 valence electrons in the $NH_3$ molecule since the $1e$ label represents a degenerate pair. The corresponding liquid spectrum obtained from the microjet measurements can be seen in the top panel of Figure 1.3 as raw experimental data in black and fitted with Gaussians in green. It can be immediately noticed that the whole spectrum retains its general shape but is shifted to higher binding energies by ∼2 eV, *i.e.*, the electrons in the liquid sample are bound more weakly. This is a general effect seen in gas-to-liquid transitions that is a consequence of the dielectric screening by the condensed environment; we will revisit it in the discussion part of this thesis in terms of a simple model based on a Born–Haber cycle in Chapter 4.[58] The computational prediction reliably reproduces the experimental peak positions for both the gas and the liquid phase, suggesting that our computational approach captures the relevant physics underlying the XPS experiment. Note that the intensity in the middle peak of the EDOS, which corresponds to the doubly degenerate state, is higher than that of the remaining ones (that the area under the peaks in question is exactly twice larger can be shown rigorously by integration).

The microscopic structure of the blue dilute solvated electron solutions in liq-

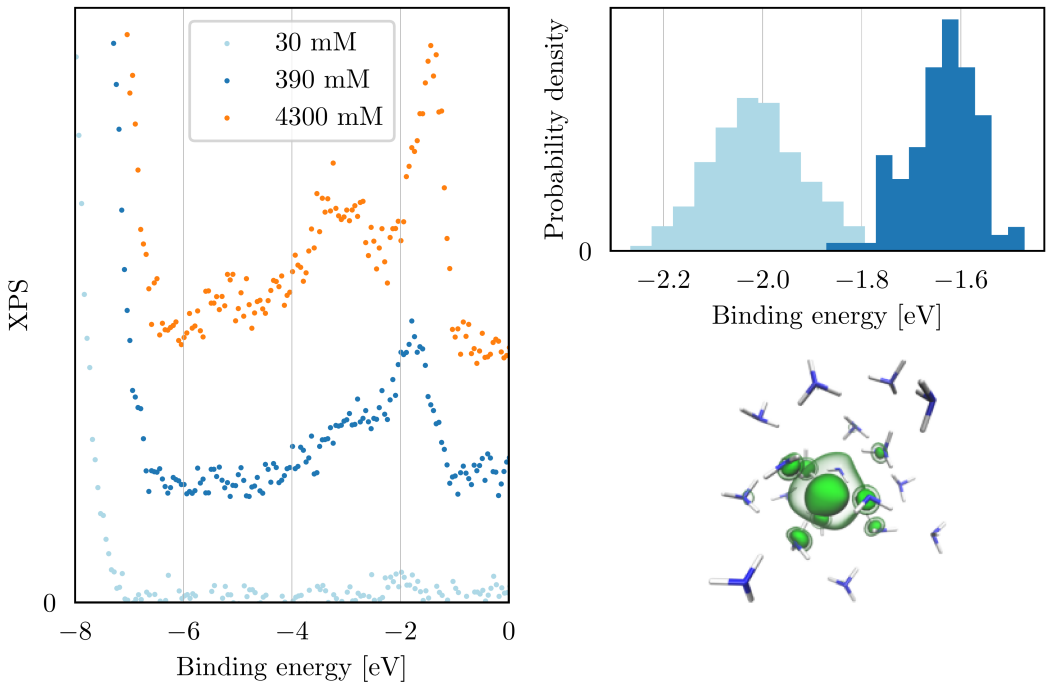


Figure 1.4: Measured and calculated binding energies of excess electrons in liquid ammonia.[62] Left panel: Measured XPS spectra at three different concertations of Li metal corresponding to the single electron (light blue), dielectron (blue), and metallic regimes (orange). Top right: Calculated distribution of electron binding energies for solvated electrons (light blue) and dielectrons (blue). Bottom right: Snapshot from the single electron AIMD simulation showing the excess electron density (green, two different contours) and its closest solvent molecules.

uid ammonia has been for a long time a matter of debate, wavering over the *radical anion picture*[59] on one hand where the excess electron is localized over several solvent molecules forming solvated $(NH_3)_n^-$ clusters, and the *cavity picture*[60] on the other, in which the excess electron resides in a hollow cavity formed within the solvent structure. Today, there is a general consensus that favors the validity of a combined picture[61] with most of the excess electron localized in a cavity away from solvent molecules with an off-nuclear density maximum but also with non-zero excess electron population on the atoms belonging to the first solvent shell of the cavity. Gradually, as the metal concentration is increased, the solution first becomes nearly black and opaque and enters the *dielectron* regime, which features spin-singlet electron pairs still inside cavities and then turns golden in color and a characteristic metallic sheen appears accompanied by a large change in conductivity, suggesting that the system has acquired properties of a metal.

The immediate next step in our research thus was to introduce excess electrons in liquid ammonia with the aim to map the intriguing electrolyte-to-metal transition through the changes in electronic structure.[62] Using the liquid microjet technique applied to these solutions, we found that in the low concentration regime, a new XPS feature appears at approximately −2.0 eV alongside what initially was the neat ammonia spectrum, which corresponds to the ionization of

the solvated excess electron (Figure 1.4). As the dielectron regime is reached, this feature moves to −1.6 eV due to the mutual electrostatic destabilization of the dielectron but does not change in character. However, the shape of the spectrum changes dramatically with the gold solutions, where manifestly metallic features appear that include both a Fermi edge and multiple plasmon peaks (Figure 1.4), suggesting that the localized solvated electron state has transformed into a Bloch-like delocalized state. Tackling the solvated electron in liquid ammonia computationally is much more daunting than the pure solvent. At the level of AIMD simulations, this is primarily connected to the open-shell nature of the system as well as stringent requirements on the employed density functionals and basis sets. Specifically, the system must be described at a hybrid density functional theory level to suppress delocalization issues pertaining to self-interaction error[63] and, at the same time, requires an augmentation of the basis set[64,65] in order to be able to describe cavities. Still, running such simulations is possible with sufficient computational resources, and several ps-long simulations of a solvated electron and dielectron were obtained.[62] Most importantly, these simulations point to the stability of cavities (Figure 1.4) over the studied time frame, corroborating previous indirect observations. The $G_0W_0$ approach was not applicable in this case as it produced results that significantly deviated from the experiment: this was likely due to an unfortunate combination of the notoriously difficult convergence of $G_0W_0$ with basis set size[66] and the elevated basis set requirements for this system. Therefore, the EDOS over the whole energy range was not calculated in Reference 62, but an alternative approach based on extraction of open thermal clusters from the bulk AIMD simulations followed by explicit vertical ionization calculations in a non-equilibrium polarizable continuum[67] was used to model the highest binding energy peak in the single electron and dielectron concentration regime (Figure 1.4). This is in excellent agreement with the measured binding energies, giving further credibility to the simulated cavity picture. The simulation of the metallic system and the transition to it is a subject of ongoing research.

Apart from the intriguing physical properties of alkali-metal–ammonia solutions, one should not forget that they can also act as useful chemical reagents. One of the most well-known applications of the blue solutions of solvated electrons in organic chemistry is the so-called Birch reduction[68] of six-membered aromatic rings to 1,4-cyclohexadienes using sodium in liquid ammonia, which has gained enormous popularity in small-scale synthetic applications[69] due to its versatility and has been employed at an industrial scale, for instance, in the delicate synthesis of steroid derivatives.[70] The widely accepted mechanism of the Birch reduction is initiated by the attachment of the solvated electron to the aromatic species to form a radical anion, which is then further reduced and protonated by a viable proton source in several subsequent steps into the final product. Taking benzene ($C_6H_6$) as the prototype example, we perform AIMD simulations of the corresponding benzene radical anion intermediate to gain insight into the initial stages of the Birch reduction and understand problems like the microscopic structure and solvation of the anion and its comparison to the neutral solute, and the spatial distribution of the excess electron and its comparison to the solvated electron case. The analysis and discussion of these simulations are described in

two attached papers.[71,72] Reference 71 focuses mainly on the issues of molecular geometry while shedding light on issues such as the dynamic Jahn–Teller distortion of the geometry of the benzene radical anion, solvation structure, vibrational spectroscopy and $\pi$-hydrogen bonding (see the following Section for further details on this topic). Reference 72 then focuses on electronic structure aspects of the system in question and shows computational predictions of XPS spectra, effects of the solvent environment and on the electronic part of the Jahn–Teller problem. Apart from these two first-author publications, the project gave rise to three other publications[73–75] co-authored by me to a lesser extent that are not attached to this thesis, but their important findings will be mentioned in the discussion in Chapter 4 to provide a more complete picture of the presented research.

### 1.3.3 $\pi$-hydrogen bond: an exotic case

$\pi$-hydrogen bonds are an illustrative example of an exotic type of hydrogen bond that benefits from the very general definition given at the beginning of this Chapter: while the donor, in this case, is the usual solvent molecule, the acceptor is an aromatic substrate, in particular, the elevated negative charge density over the aromatic ring due to its $\pi$-electron cloud. Our finding that neutral benzene and benzene radical anion likely form $\pi$-hydrogen bonds in ammonia in our work in Reference 71 in combination with our general, group-wide focus on hydrogen bonding systems triggered a follow-up research study on this topic to provide a rounded understanding of the phenomenon not only in liquid ammonia but also in water. The aqueous solution can be understood as a prototypical system aiming to model notably the solvation of the exposed aromatic residues in proteins in an aqueous environment or the water-miscible, benzene-rich fraction[76] of oil that dissolves in seawater after oil spills. Pertaining to the latter, the solubility of benzene in water at ambient conditions is more than 20 mM[77] and in ammonia at $-50$ °C even more than 10 times higher.[74]

While that is perhaps a considerably high attainable concentration of a toxic substance for aquatic life, it is not particularly high by the standards of the resolution of most experimental methods. Therefore, a limited number of published studies focus on $\pi$-hydrogen bonding in bulk water, with most works focusing on cold cluster systems in the gas phase and isolated matrices.[79] An exception to this is represented by the key work of Gierszal and coworkers,[80] who report spectroscopic evidence of $\pi$-hydrogen bonding in an aqueous solution of benzene using ultra-low noise Raman scattering. The work relies on a postprocessing method known as Raman multivariate curve resolution,[81] which allows for the extraction of solute-correlated components of the total measured spectrum, capturing the vibrational features of the solute and the effect of its nearest surroundings. Such spectra clearly show a new vibrational feature at 3610 $cm^{-1}$, which is remarkably higher than any natural frequency of the solute and which is therefore attributed to the effect of the vibration of the $\pi$-hydrogen bonded molecule on it. This particular frequency belongs to the high-frequency end of the inhomogeneously broadened water stretch peak (approximately 2800 – 4000 $cm^{-1}$ in the

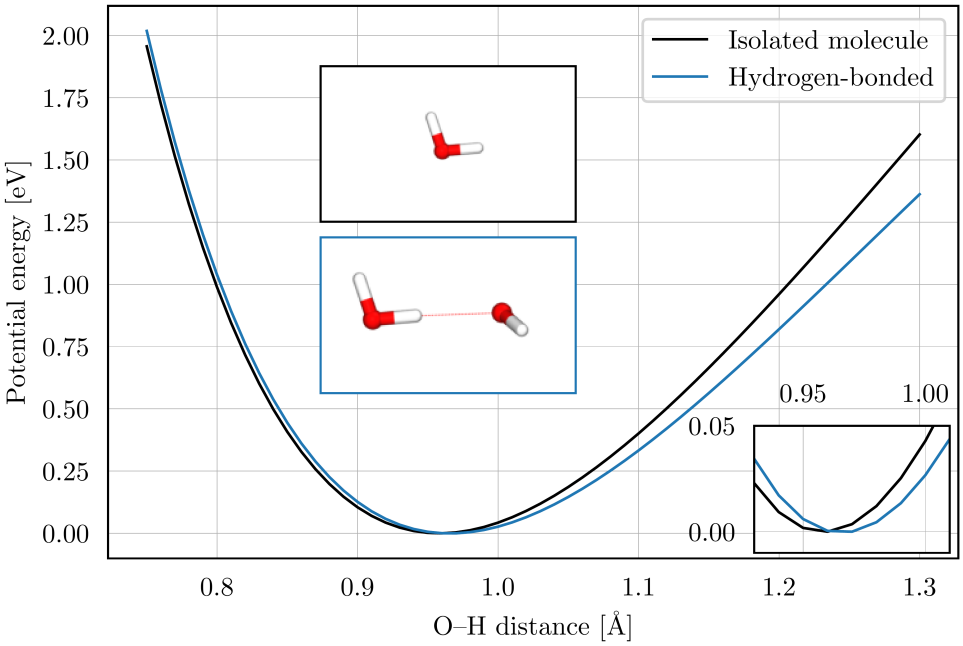


Figure 1.5: Effect of hydrogen bonding on the potential energy of the covalent O–H bond in the water dimer. The black curve shows the change in potential energy as the length of one of the O–H bonds of the isolated water monomer varies. The blue curve shows the same quantity upon variation of the length of the hydrogen-bond-forming O–H bond in the water dimer at a fixed, optimal O $\cdots$ O' distance of 2.95 Å. Both curves were obtained as a rigid scan of the covalent O–H bond length using the $\omega$B97M-V[78] range-separated hybrid density functional (see Chapter 2 for details on electronic structure theory). Note that not only the potential at larger O–H distances is softer in the dimer, but also the optimal bond length gets slightly larger (inset, bottom right).

water Raman spectrum), suggesting $\pi$-hydrogen bonds are weaker than water–water hydrogen bonds and that molecules that participate in them are essentially comparable to isolated molecules in the vibrational sense. To see why that is the case, the observed effect should be understood as a reverse blueshift of a preexisting redshift of this stretching frequency. This initial redshift is arguably one of the most important spectroscopic manifestations of the hydrogen-bonding environment in liquid water and is caused by the softening of the potential of the O–H bond due to the presence of the attractive interaction when forming the relatively strong water–water hydrogen bond (the explicitly calculated effect in the water dimer is shown in Figure 1.5). A softer, more open potential indicates closer spacing of vibrational levels and, consequently, a lowered characteristic frequency of the vibration. As such, the whole stretching peak is redshifted in liquid water compared to an isolated molecule in the gas phase. In addition, the effect explains the above-mentioned inhomogeneity of the stretch peak broadening as the breadth comes from contributions due to various temporally and spatially localized environments affecting individual O–H bonds.[82] From here, the observed effect can be explained simply by appreciating the fact that a benzene hydrogen

bond acceptor, a much less polar molecule than water, does not have the ability to open up the vibrational potential as much as a water acceptor and, therefore, induces, if any, only a minor redshift. Consequently, the $\pi$-hydrogen bonded water molecule appears blueshifted in comparison to the water bulk.

Theoretical investigations of $\pi$-hydrogen bonding in liquid water are uncommon and do not provide a complete picture of the phenomenon. Allesch and coworkers have performed simulations[83] of liquid benzene–water mixtures and report solvation structure that is consistent with our results presented later in this work; however, their main focus is the comparison of description of the $\pi$-hydrogen bonding phenomenon using very short classical AIMD simulations with a generalized-gradient approximation (GGA) density functional and longer simulations with empirical force fields, which they find to perform poorly for the purpose.[84] This immediately raises concerns pertaining to the common use of empirical force fields in biochemical MD simulations, where the interaction between liquid water and aromatic moieties in solvated proteins is abundant. Turning our attention to the issues of dynamics and spectroscopy, a noteworthy contribution is the simulation work of Choudhary and Chandra,[85] which, among other findings, addresses the lifetimes of $\pi$-hydrogen bonds to find that they are shorter than those in the bulk solvent, suggesting an interaction that is weaker than the average water–water hydrogen bond. At the GGA level of electronic structure theory and using an approximate approach to model the vibrational frequency spectrum based on wavelet transforms,[86] they capture the trend of the blueshift qualitatively consistent with the implication of the above-mentioned Raman experiment.

Our work aims to provide a well-rounded picture of the phenomenon in terms of structure, dynamics, and vibrational spectroscopy. Since the publication of the previous theoretical studies, it was well recognized that GGA density functionals are not entirely appropriate for the description of structure and dynamics of hydrogen-bonded liquids and that the use of hybrid functionals leads to a much more physically motivated and closer real-world correspondence, especially with a path-integral description of the nuclei.[4] In that light, we perform simulations of benzene in liquid water and liquid ammonia at a hybrid DFT level of theory while also addressing the need to include NQEs using the path integral approach. Recognizing that the convergence of statistical sampling in the similar radical anion simulations anion systems simulated using traditional classical AIMD was sufficient, but perhaps borderline on noisiness,[71] we prepared C-NNP models for both systems to facilitate the simulation. Analyzing the obtained trajectories, we gain insight into the structure of the solvation environment of benzene in the two solvents and identify clear evidence for the formation of $\pi$-hydrogen bonds in these systems. Using these results, we set up criteria on $\pi$-hydrogen bond existence, which we use to address the issue of dynamics and lifetimes. We also discuss the cooperativity of $\pi$-hydrogen bonds (since a single benzene molecule simultaneously offers two binding sites for the solvent molecules), where we find limitations that challenge the accuracy of the C-NNP description, despite the initially inconspicuous-seeming nature of the studied system. Therefore, we address the cooperativity issue using *ab initio* simulations. Finally, these are also

used for the simulation of infrared (IR) spectra, where molecular dipole moments must be known but cannot be obtained directly from the NNP. The main results of this work are presented in Reference 87 and summarized and discussed in Chapter 5.

### 1.3.4 Hydrogen-bonded supramolecules on Au(111)

In the last project, we will depart from the disordered liquid realm that dominated the previous projects in favor of metal-surface-bound molecules that feature hydrogen bonding in both the intra- and intermolecular sense. Such systems have played the role of protagonists in many very active fields of research. This includes nanoscale applications in electronics and motors[88,89] and surface catalysis;[90] they are instrumental in biofilm formation,[91] and in the sense of going towards the hydrogen-bonded liquid–metal interface,[92] they are key in questions of clean energy generation and storage. Clearly, there is a great need to understand the microscopic processes happening in such systems, which is a suitable application for molecular simulations. However, simulating these systems with sufficient extent both in time and space and with enough accuracy can be prohibitive even with modern-day computational options.

Here, the initial motivation to study a hydrogen-bonded surface system using advanced theoretical methods stems from scanning tunneling microscopy (STM) and atomic force microscopy (AFM) findings of Cahlík and coworkers,[93] who studied the assembly of supramolecular structures of 2,5-diaminobenzoquinone-1,4-diimine (DABQDI) molecules (molecular structure shown in Figure 1.6) on Au(111) surface at liquid helium temperatures. These molecules are generally observed to aggregate into one-dimensional hydrogen-bonded chains, where the hydrogen bonding is enabled by interactions between the amine groups ($-NH_2$, as the donor) and the imine groups (=NH, as the acceptor) along the chain. However, the particular properties of the chains depend on the conditions at the deposition of the molecules on the surface before the sample is cooled down for the ensuing microscopy. Specifically, molecules deposited at liquid helium temperatures lead to the formation of linear chains which are robust and laterally manipulable without breaking and possess a *straight* geometry where each monomer is aligned with the chain axis (Figure 1.7, left). In contrast, depositing the molecules at room temperature gives rise to brittle chains that cannot be laterally manipulated without breaking, and which adopt an occasional "zigzag" deviation from linearity and which possess a *canted* geometry where the monomers are oriented at an angle with the axis of the chain (Figure 1.7, right). Accompanying DFT optimizations show that the classical PES minimum exhibits the canted geometry with slanted individual monomers, and the symmetry of the problem suggests that two equivalent minima must exist, each canted to one side and connected by a complete proton exchange reaction across the conjugated chain of hydrogen bonds.

The existence of the straight chains is interpreted as an NQE. Effectively, the symmetric system can be represented by a double-well potential, in which each well corresponds to one classical minimum, and the observed straight chain can

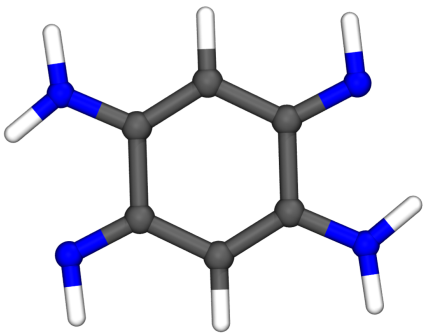

Figure 1.6: Molecular structure of the DABQDI (2,5-diaminobenzoquinone-1,4-diimine) monomer.

be explained as a delocalized quantum state over both wells or a superposition thereof that dynamically evolves between the two wells, yielding a symmetric microscopic image with concerted proton tunneling. The origin of the canted chains is not discussed in depth in the original publication; the authors claim that in that case, the superposition between states localized in the individual wells is not possible "*due to an external constraint*" caused by the conditions at the deposition of the molecules onto the substrate. As such, the canted chains are understood as frozen in one of the wells, yielding a structure consistent with the classical minimum-energy configurations. It is important to note, however, that the canted chains cannot be understood as fundamentally classically behaving. The above understanding has a good degree of computational support in the form of path integral umbrella sampling free energy calculations,[27] which predict the free energy along a suitably chosen collective variable (CV) that describes the proton-sharing reaction. These point to the fact that NQEs substantially lower the barrier for the reaction compared to the classical picture and that concerted proton tunneling is indeed the preferred mechanism at 10 K.[93] However, in order to reduce the computational cost of the extensive simulations and to make them accessible in a reasonable time frame, they were performed at a QM/MM level combining a semi-empirical Fireball PES[94] for the DABQDI chains and a fully empirical van-der-Waals representation of the gold surface (*i.e.*, the surface does not explicitly enter the electronic structure calculation, but only acts as an external force on the surface-bound molecules). Such methodology might be sufficient to successfully corroborate the interpretation of the experiment, but it cannot be considered state of the art, certainly not for metal-surface-bound systems, which are known to require very accurate electronic structure methods[95] on top of the above-discussed requirements on the quality of the DFT description of hydrogen bonding itself.

Therefore, our primary goal in this project was to deliver a state-of-the-art description of these systems using advanced *ab initio* electronic structure to validate and extend the existing results. Clearly, performing these simulations, which require an explicit representation of several hundreds of heavy atoms, naively using traditional AIMD methods is a futile effort, and an NNP description is necessary. However, as it was alluded to in Section 1.3.1, even obtaining enough *ab initio* data for the NNP training might be difficult or impractical, especially for

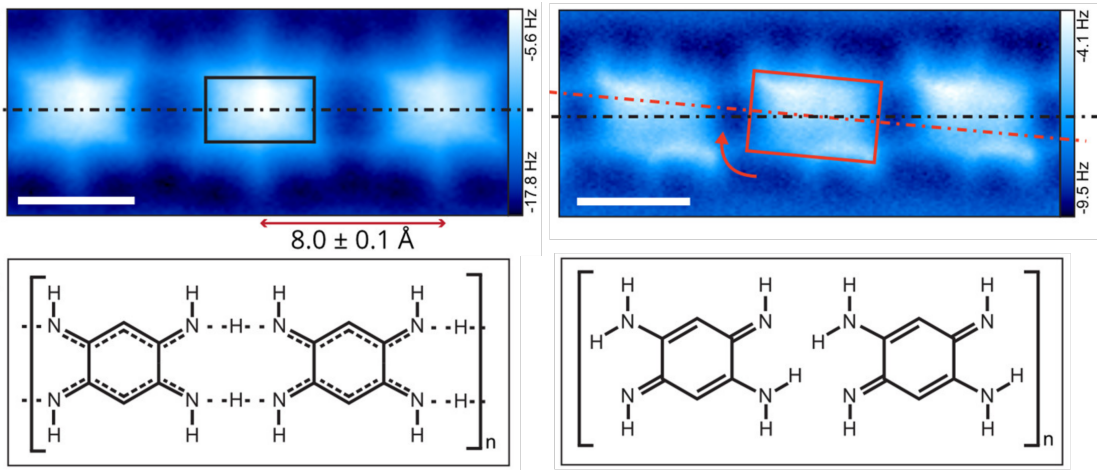


Figure 1.7: Supramolecular structure of DABQDI chains.[93] Top left: AFM detail of the straight DABQDI chain. The black dashed line shows the axis of the chain that is collinear with the long axis of the individual monomers. Bottom left: Proposed molecular structure for the straight DABQDI chain with the exchangeable hydrogen atoms symmetrically shared between the chain units. Top right: AFM detail of the canted DABQDI chain. The black dashed line has the same meaning as above; the monomer axis, which now deviates from collinearity with the chain axis, is shown in red. Bottom right: Proposed molecular structure of the canted DABQDI chain with all hydrogen atoms localized on their respective monomers. This corresponds to the DFT-optimized minimum geometry. Reprinted (adapted) with permission from Reference 93. Copyright 2021 American Chemical Society.

systems where a reaction must be well described, as is the case here. This issue motivated us to start working on the above-mentioned TTS methodology, as it should be, in principle, able to generate reactive training sets for such a system at a significantly reduced cost compared to the traditional approach using AIMD.

While the TTS method itself is described in Chapter 3, we discuss our unpublished explorations of the physics and chemistry of various DABQDI-based systems in Chapter 6. These calculations pave the way to the big simulations of systems that directly relate to the experiments — these, however, remain an open task at this moment. We approach the problem from the gas phase and address the PESs of the isolated monomer and a few of the shortest chains to understand the available configurations and the classically allowed proton-transfer mechanism. At the level of the monomer, which itself is also a proton-sharing system and can be understood as a chain consisting of only a single unit and two proton transfers, we then introduce NQEs using ring polymer instanton rate theory,[96] which allows us to calculate the thermal rate of tunneling through the proton-sharing barrier and estimate the relevance of different proton-sharing mechanisms as a function of temperature. For the surface-bound systems, we present several minimum-energy geometries, estimate the surface–molecule coupling, and proceed to take the first steps towards a C-NNP model for the surface-bound monomer using TTS with no AIMD simulations performed at any stage of the model generation.

# 2 | Theory and methodology

The following chapter contains a brief perspective on the fundamental theory relevant to the methods developed and applied in this work. The first section opens briefly with the key concepts of the time evolution of quantum systems and introduces a crucial tool of theoretical chemical physics: the Born–Oppenheimer approximation,[2,32,97] which splits the molecular problem into independent electronic and nuclear parts. The second section discusses practical approaches to the solution of the electronic Schrödinger equation while focusing on methods relevant to this work. In the third section, we then turn our attention to the dynamics of nuclei and the application of statistical mechanics to calculate the static and dynamic properties of molecular systems.

## 2.1 | Quantum dynamics of molecular systems

In the following, we will discuss the way from the fully general non-relativistic quantum-mechanical time evolution down to the Born–Oppenheimer approximation, which provides a framework for the practical computational methods used to study molecular systems that are at the heart of this work, including MD simulations.

One of the pivotal postulates in quantum mechanics is that a quantum system, described at a given initial moment in time $t_0$ by the ket $|\Psi(t=t_0)\rangle$ defined on a Hilbert space $\mathcal{H}$, undergoes unitary evolution in time.[17,98] The requirement of unitarity, *i.e.*, a mathematical property of a transformation to preserve the norm of the ket on which it is acting,[17] comes about rather naturally to fulfill the fundamental law of matter conservation in the system. The mathematical core of the postulate is the following equation

$$|\Psi(t)\rangle = e^{-\frac{\mathrm{i}}{\hbar}(t-t_0)\widehat{H}}\,|\Psi(t_0)\rangle \equiv \widehat{U}(t-t_0)\,|\Psi(t_0)\rangle\,, \tag{2.1}$$

where the complex exponential defines the evolution operator $\widehat{U}$, $\widehat{H}$ is the Hermitian (and here, for simplicity time-independent) Hamiltonian, i is the imaginary unit, and $\hbar$ is the reduced Planck constant. A fully equivalent statement of the same is the time-dependent Schrödinger equation

$$\mathrm{i}\hbar\frac{\mathrm{d}}{\mathrm{d}t}\,|\Psi(t)\rangle = \widehat{H}\,|\Psi(t)\rangle\,, \tag{2.2}$$

which can be obtained by differentiation of the previous equation with respect to

time and which represents the equation of motion of quantum mechanics.[a] Generally speaking, the exact solution of the equation is complicated and analytically feasible for only a few of the simplest systems. An exception to this, which is quite significant in quantum physics, pertains to quantum states known as stationary states. Highly non-trivial dynamics of a general state can be expressed as a linear combination of dynamics of stationary states, which themselves evolve trivially in time. Specifically, these states are not fixed but rather undergo evolution where only a complex phase factor is allowed to rotate with a given frequency, technically modifying a fixed vector part but not changing the ray in the underlying Hilbert space. As such, all observables calculated over stationary states do not change in time. It is clear from Equation 2.1 that such states coincide with the eigenstates of the Hamiltonian and, therefore, comply with a different, time-independent formulation of the Schrödinger equation

$$\widehat{H}\left|\Psi_n\right\rangle = E_n\left|\Psi_n\right\rangle, \tag{2.3}$$

where $E_n$ is the corresponding energy eigenvalue. The knowledge of stationary states is of major importance in quantum mechanics: they form an orthonormal basis to the underlying Hilbert spaces and thus allow for the expression of any arbitrary state as a superposition. At the same time, the energy spectrum carries much information on the system and allows us to compare computational models to experimental data.

In this work, we are primarily concerned with describing the properties and dynamics of systems that contain atoms and molecules, and therefore, it is natural to look for an approximation that would allow us to simplify the dynamic Schrödinger equation while accurately describing all components of the system. For applications in chemical physics, two assumptions are usually made for the atomic nuclei. First, the individual nuclei are typically considered pointlike particles because one is seldom interested in questions that touch on nuclear processes at this level of study. Second, due to the relatively large mass of atomic nuclei, particle indistinguishability is often neglected since it normally does not play a significant role, except for very light and very cold systems such as superfluid helium.[31,99,100] On the other hand, the electrons are treated as indistinguishable fermions in full agreement with the Pauli principle. The state vectors describing molecular systems thus exist on a Hilbert space that is formed by the direct product of the nuclear and electronic subspaces

$$\mathcal{H} = \mathcal{H}_{\mathrm{n}} \otimes \mathcal{H}_{\mathrm{e}}. \tag{2.4}$$

The molecular Hamiltonian

$$\widehat{H} = \widehat{T}_{\mathrm{n}} + \widehat{T}_{\mathrm{e}} + \widehat{V}_{\mathrm{ee}} + \widehat{V}_{\mathrm{en}} + \widehat{V}_{\mathrm{nn}} \tag{2.5}$$

consists of the kinetic energies $\widehat{T}$ for the nuclei and electrons and all their various, appropriately indexed interactions $\widehat{V}$ and acts on $\mathcal{H}$. Ideally, the Hamiltonian

[a] Note that the subtle quantum prefactor $\mathrm{i}\hbar$ that appears in the Schrödinger equation carries significant physical meaning: the imaginary nature of the equation is the consequence of the requirement on the unitarity of the time evolution and the Planck constant $\hbar = h/2\pi \approx 1.055 \cdot 10^{-34}$ J·s is a scale for the quantum-mechanical effects that is a fundamental property of nature.

would be expressible as a sum of operators on the relevant subspaces, which would, in turn, cast the exact molecular state vector into a separable tensor-product form. However, this is not possible due to the presence of the electron–nuclear interaction operator $\widehat{V}_{\mathrm{en}}$. This renders the Hamiltonian inseparable and does not allow us to address the dynamics of nuclei and electrons in an exact yet uncoupled way. To exploit the separable form of the state vector anyway, which is the main goal of the Born–Oppenheimer approximation, we must ask under what conditions this represents a reasonable treatment.

To begin, we group the molecular Hamiltonian into the standalone nuclear kinetic energy operator

$$\widehat{T}_{\mathrm{n}} = \sum_{I=1}^{N} \frac{\widehat{\mathbf{P}}_I^2}{2M_I} = -\sum_{I=1}^{N} \frac{\hbar^2}{2M_I} \boldsymbol{\nabla}_I^2 \tag{2.6}$$

and into an electronic Hamiltonian

$$\widehat{H}_{\mathrm{e}} = \sum_{i=1}^{n} \frac{\widehat{\mathbf{p}}_i^2}{2m_{\mathrm{e}}} + \frac{e^2}{4\pi\varepsilon_0} \left( \sum_{j<i} \frac{1}{|\widehat{\mathbf{r}}_i - \widehat{\mathbf{r}}_j|} - \sum_{i,I} \frac{Z_I}{|\widehat{\mathbf{r}}_i - \widehat{\mathbf{R}}_I|} + \sum_{J<I} \frac{Z_I Z_J}{|\widehat{\mathbf{R}}_I - \widehat{\mathbf{R}}_J|} \right) \tag{2.7}$$

that contains all the remaining operators.[b] In these expressions, $\widehat{\mathbf{p}}_i$, $\widehat{\mathbf{r}}_i$, $\widehat{\mathbf{P}}_I$ and $\widehat{\mathbf{R}}_I$ are respectively the momentum and position operators of the $i$-th electron and $I$-th nucleus in the system, $e$ is the elementary charge, $\varepsilon_0$ is the vacuum permittivity, $m_{\mathrm{e}}$ is the electron mass and $Z_I$ and $M_I$ are the charge and mass of the $I$-th nucleus. We have included the position representation of the kinetic energy operator using the del operator in Equation 2.6. With such grouping, the nuclear kinetic energy operator, which clearly only acts on $\mathcal{H}_{\mathrm{n}}$, is separated from the electronic Hamiltonian that keeps acting on full $\mathcal{H}$. However, the action of the electronic Hamiltonian on the nuclear degrees of freedom is trivial in the sense that all dependence on them is through a simple Coulomb law function of the position operator. With this in mind, one can make a convenient basis set choice for $\mathcal{H}_{\mathrm{n}}$ by picking the position basis $|\mathbf{R}\rangle$ where $\mathbf{R}$ denotes the nuclear configuration — the one-dimensional vector of all nuclear coordinates $\{\mathbf{R}_I\}_{I=1}^{N}$. With this choice, the action of the electronic Hamiltonian on a state defined as a product of a vector from the nuclear position basis and an arbitrary vector in $\mathcal{H}_{\mathrm{e}}$ would be trivial on $\mathcal{H}_{\mathrm{n}}$, essentially parametrizing the electronic Hamiltonian with a sharp value of $\mathbf{R}$ and reducing its domain into $\mathcal{H}_{\mathrm{e}}$ only, where its action remains non-trivial.[c] This new, reduced electronic Hamiltonian is further denoted as $\widehat{H}_{\mathrm{e}}(\mathbf{R})$ to emphasize its parametrization.

[b] Note that including the internuclear interaction operator in the electronic Hamiltonian is slightly counter-intuitive but gives a nicer equation in the end and does not alter any physics whatsoever.

[c] Using the position basis on the nuclear subspace is merely a convenient choice for performing the Hilbert space algebra, not a move towards a classical description. In fact, it is a common misconception that a classical treatment of the nuclei is necessary for the Born–Oppenheimer approximation. On the contrary, the Born–Oppenheimer approximation represents a fully quantum-mechanical approach.

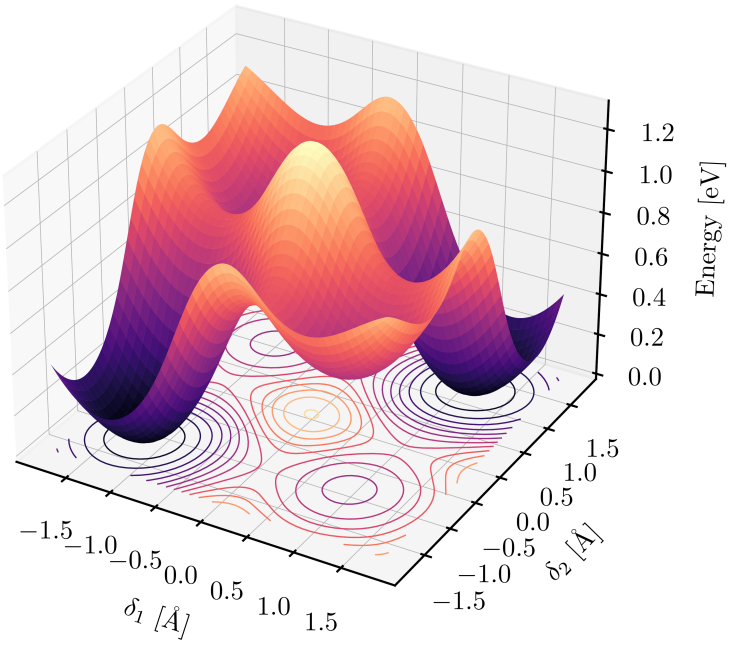


Figure 2.1: A real-world example of a PES. Here, the energy is shown as a function of geometric parameters $\delta_1$ and $\delta_2$, which describe collective motion of atomic nuclei in a molecular system. The surface and the contours are colored according to the value of the energy: the lighter the color, the higher the energy. We will return to this particular surface, used here only as an illustration, in detail in Chapter 6.

At this point, one can define the separate stationary electronic problem for the given nuclear configuration as

$$\widehat{H}_{\mathrm{e}}(\mathbf{R})\,|n(\mathbf{R})\rangle = E_n(\mathbf{R})\,|n(\mathbf{R})\rangle \tag{2.8}$$

and assume that we can solve it for the eigenstates $|n(\mathbf{R})\rangle$, which form an orthonormal basis for $\mathcal{H}_{\mathrm{e}}$ for each individual choice of $\mathbf{R}$.[d] On its own, this is a very complicated task that requires approximate numerical treatment for realistic systems, some of which are discussed in Section 2.2. Since the Hamiltonian was parametrized by the nuclear configuration, this parametrization translates accordingly into the energy eigenvalue $E_n(\mathbf{R})$ (see example in Figure 2.1). This function plays a key role in the Born–Oppenheimer framework and is known as the potential energy (hyper)surface (PES).

With all this in mind, one can re-express the molecular state vector using the usual product-basis form by combining the electronic eigenstates and the nuclear position basis as

$$|\Psi(t)\rangle = \sum_n \int \mathrm{d}\mathbf{R}\; c_n(\mathbf{R},t)\,|n\rangle \otimes |\mathbf{R}\rangle\,, \tag{2.9}$$

[d] In the following, we will write $|n\rangle$ in place of $|n(\mathbf{R})\rangle$ to keep the notation clean, but the parametric dependence of the electronic states on the nuclear configuration is of key importance.

where the time dependence has been absorbed into the set of linear combination coefficients $c_n$ without loss of generality. This expression is fully flexible and can describe an arbitrary molecular state vector since all constituent bases are complete.

Substituting the above Ansatz into the time-dependent Schrödinger equation 2.2 and multiplying by an arbitrary electronic bra $\langle m|$ to integrate out the electronic degrees of freedom gives the following rather complicated set of dynamical equations for the nuclei

$$\begin{aligned} &\mathrm{i}\hbar \int \mathrm{d}\mathbf{R}\ \frac{\mathrm{d}}{\mathrm{d}t} c_m(\mathbf{R},t)\,|\mathbf{R}\rangle = \\ &-\frac{\hbar^2}{2}\sum_{I,n}\frac{1}{M_I}\int \mathrm{d}\mathbf{R}\ \left(\langle m|\,\boldsymbol{\nabla}_I^2\,|n\rangle + \langle m|\,\boldsymbol{\nabla}_I\,|n\rangle\cdot\boldsymbol{\nabla}_I\right) c_n(\mathbf{R},t)\,|\mathbf{R}\rangle \\ &+\int \mathrm{d}\mathbf{R}\ \widehat{T}_{\mathrm{n}} c_m(\mathbf{R},t)\,|\mathbf{R}\rangle \\ &+\int \mathrm{d}\mathbf{R}\ E_k(\mathbf{R}) c_m(\mathbf{R},t)\,|\mathbf{R}\rangle\,, \end{aligned} \tag{2.10}$$

which couples the dynamics on all PESs in a non-trivial way through the coupling coefficients in the first term on the right-hand side. These coefficients arise due to the parametric dependence of the electronic states on the nuclear configuration. Technically, the Born–Oppenheimer approximation amounts to neglecting these coefficients.[e] This leaves one with an effective time-dependent Schrödinger equation for the nuclei only

$$\mathrm{i}\hbar\frac{\mathrm{d}}{\mathrm{d}t}\,|\phi_m(t)\rangle = \left(\widehat{T}_{\mathrm{n}} + \widehat{E}_m\right)|\phi_m(t)\rangle\,, \tag{2.11}$$

where $|\phi_m(t)\rangle = \int \mathrm{d}\mathbf{R}\ c_m(\mathbf{R},t)\,|\mathbf{R}\rangle$ is the nuclear state vector of the $m$-th PES (note that its position representation is given by the coefficient $c_m(\mathbf{R},t)$) and $\widehat{E}_m$ is the Hilbert space operator abstraction of the PES. As such, the Born–Oppenheimer approximation allows one to describe the dynamics of the molecular system in a decoupled way where the nuclei move in a potential given by a single, well-defined PES.

So, what are the physical conditions under which we can neglect the coupling coefficients to make the Born–Oppenheimer approximation a valid concept? First, a general observation can be made about the proportionality of the coupling terms in comparison to the total energy $\widehat{T}_{\mathrm{n}}+\widehat{E}_m$. Specifically, the couplings are inversely proportional to the mass of the nuclei, whereas the total energy is proportional to $1/m_{\mathrm{e}}$ — the cumbersome exact proof was delivered in the original contribution by Born and Oppenheimer,[32] but it can be alluded to easily by building on the premise of tight-binding electrons.[101] Therefore, the ratio between the masses of electrons and nuclei between $10^{-4}$ and $10^{-5}$ is enough to claim that the couplings are generally small unless a specific configuration causes the individual coupling matrix elements to blow up. To see when this may happen, let us have a closer

[e] Alternatively, the *adiabatic* approximation only neglects the off-diagonal terms and keeps the diagonal ones as static corrections to the Born–Oppenheimer PES.

look at the definition of the coupling coefficients. In fact, out of the two types of coefficients — a scalar one with the Laplacian $\boldsymbol{\nabla}_I^2$ and a vectorial one featuring the gradient $\boldsymbol{\nabla}_I$ — it is only needed to discuss the vectorial one since the scalar can be expressed in its terms.[102] By differentiating the electronic Schrödinger equation 2.8 with respect to $\mathbf{R}$, we easily find for $m \neq n$ that

$$\langle m| \boldsymbol{\nabla}_I |n\rangle = \frac{\langle m| \boldsymbol{\nabla}_I \widehat{H}_\mathrm{e}(\mathbf{R}) |n\rangle}{E_n(\mathbf{R}) - E_m(\mathbf{R})}, \tag{2.12}$$

which defines the conditions under which the coupling constant remains small. In particular, due to the nature of the numerator, we require the change of the electronic Hamiltonian with nuclear configuration to be vanishing, and, due to the form of the denominator, we require a large energy separation between the individual PESs. As such, the Born–Oppenheimer approximation is challenged when the nuclear dynamics happens on a rapidly changing PES or when different PES sheets come close or intersect. Systems that exhibit such behavior must be modeled using methods of non-adiabatic dynamics:[97,103] a typical example of this is dynamics at conical intersections. However, for most molecular systems, including the ones discussed in this work, the Born–Oppenheimer approximation represents a widely applicable and very useful simplification that allows for highly efficient simulation methods.

## 2.2 | The electronic problem

The most important conclusion of the above section is that one can approximate, often very accurately, the evolution of a molecular system by evolving the nuclei on a fixed PES given by the electrons. The way to the PES thus relies on the solution of the electronic problem along the lines of Equation 2.8. Obviously, this is no easy task on its own, as one is challenged with a correlated many-body problem, which does not generally have a full, exact solution available at hand. Therefore, we are forced to turn to approximate schemes once again to be able to perform practical electronic structure calculations. In the following paragraphs, we present and discuss three families of electronic structure methods relevant to this work. We will begin, perhaps in a bit unusual way for works in this field, by discussing the Green's function (GF) perspective. This leads to the appearance of the so-called Dyson equation, the value of which lies in the fact that it provides a unified context for simple one-electron methods by formalizing the concept of a one-electron state in a correlated many-body system. We will use this perspective to discuss two commonplace methods used in quantum chemistry: the Hartree–Fock (HF) approximation and Kohn–Sham (KS) DFT. These, combined together into a single method known as hybrid DFT, represent the primary electronic structure methodology used in the present research. Finally, we introduce the GW approximation — a particularly suitable method for the calculation of condensed-phase XPS spectra employed widely in this work — and discuss important practical aspects of electronic structure calculations.

### 2.2.1 Green's functions in molecular quantum mechanics

The concept of a GF originates in the mathematics of differential equations where it represents an impulse response of a differential operator.[17] In quantum mechanics of a single particle, it is straightforward to show[17] that the GF for the dynamic Schrödinger equation is given by the following matrix element

$$G(\mathbf{x},\mathbf{x}',t-t_0) = -\frac{\mathrm{i}}{\hbar}\Theta(t-t_0)\,\langle\mathbf{x}|\,e^{-\frac{\mathrm{i}}{\hbar}(t-t_0)\widehat{H}}\,|\mathbf{x}'\rangle \tag{2.13}$$

and, as such, represents the amplitude of propagation of the particle from spatial and spin coordinate $\mathbf{x} \equiv (\mathbf{r}, s)$ to point $\mathbf{x}'$ in time $t$ for all $t > t_0$ (ensured by the Heaviside step function $\Theta$). In the single-particle case, the knowledge of the GF and the solution of the Schrödinger equation are equivalent.

Similarly, the many-body generalization of the single particle GF, usually known as the one-particle GF $G^{(1)}$, measures how much adding or removing a single electron from an $n$-electron system disrupts the dynamics of the system in comparison to the undisturbed case. Mathematically, it is defined using the Heisenberg picture[98] as

$$G^{(1)}(\mathbf{x},\mathbf{x}',t-t_0) = -\frac{\mathrm{i}}{\hbar}\,\langle\psi_0|\,\mathfrak{T}\left[\widehat{\psi}(\mathbf{x}',t)\widehat{\psi}^{\dagger}(\mathbf{x},t_0)\right]|\psi_0\rangle\,, \tag{2.14}$$

where $|\psi_0\rangle$ is the exact correlated ground state, $\widehat{\psi}^{\dagger}(\mathbf{x},t)$ and $\widehat{\psi}(\mathbf{x},t)$ are the Heisenberg-represented field creation and annihilation operators[17] and $\mathfrak{T}$ is the so-called time ordering superoperator which orders the operators from the left by ascending time and includes a sign change when a flip is needed,

$$\mathfrak{T}\left[\widehat{\psi}(\mathbf{x}',t)\widehat{\psi}^{\dagger}(\mathbf{x},t_0)\right] = \Theta(t-t_0)\widehat{\psi}(\mathbf{x}',t)\widehat{\psi}^{\dagger}(\mathbf{x},t_0) - \Theta(t_0-t)\widehat{\psi}^{\dagger}(\mathbf{x},t_0)\widehat{\psi}(\mathbf{x}',t). \tag{2.15}$$

The inclusion of the time ordering superoperator into the definition is crucial for the emergence of the complete picture: note that this breaks the GF into two terms where the first one describes *forward* propagation with the addition of a *particle* and the second *backward* propagation with the removal of a particle, or equivalently, the addition of a *hole*. This sheds light on the seemingly little-motivated inclusion of the step function into the definition of the single particle GF above, where the hole part does not exist and the GF naturally remains zero for all backward propagation.

Perhaps a more intriguing quantity than the time-dependent version of $G^{(1)}$ from the point of view of spectroscopy is its Fourier transform, which is derived in Appendix A and is known as the Lehmann representation,[104,105]

$$\begin{aligned} G^{(1)}(\mathbf{x},\mathbf{x}',\omega) = &\sum_k \frac{\langle\psi_0|\,\widehat{\psi}(\mathbf{x}')\,|\psi_k^+\rangle\,\langle\psi_k^+|\,\widehat{\psi}^{\dagger}(\mathbf{x})\,|\psi_0\rangle}{\hbar\omega - \epsilon_k^+ + \mathrm{i}\eta} \\ &+ \sum_l \frac{\langle\psi_0|\,\widehat{\psi}^{\dagger}(\mathbf{x})\,|\psi_l^-\rangle\,\langle\psi_l^-|\,\widehat{\psi}(\mathbf{x}')\,|\psi_0\rangle}{\hbar\omega - \epsilon_l^- - \mathrm{i}\eta}. \end{aligned} \tag{2.16}$$

Here, we have introduced a complete set of states $|\psi_k^+\rangle$ of the system augmented by one particle in the particle term and a complete set of states $|\psi_l^-\rangle$ of the

system missing one particle in the hole term and their corresponding eigenenergies through $\epsilon_k^+ \equiv E_k^+ - E_0$ and $\epsilon_l^- \equiv E_0 - E_l^-$. Two important observations can be made immediately after inspecting the Lehmann representation. First, it diverges at frequencies corresponding to the differences in total electronic energies between the studied system with $n$ electrons ($E_0$) and the auxiliary systems with $n \pm 1$ electrons where the propagation occurs ($E_i^\pm$). Formulated alternatively, the simple poles of the GF can be found at values corresponding to the exact electron addition and removal (binding) energies $\epsilon_i^\pm$, which makes the GF very relevant in the context of the theoretical description of various spectroscopies that are based on electron addition and removal, including XPS. Second, note that the matrix elements in the numerators represent states in the one-particle Hilbert space

$$\chi_k^+(\mathbf{x}) = \langle \mathbf{x} | \chi_k^+ \rangle = \langle \psi_k^+ | \, \widehat{\psi}^\dagger(\mathbf{x}) \, | \psi_0 \rangle \tag{2.17}$$

and

$$\chi_l^-(\mathbf{x}) = \langle \mathbf{x} | \chi_l^- \rangle = \langle \psi_l^- | \, \widehat{\psi}(\mathbf{x}) \, | \psi_0 \rangle \tag{2.18}$$

that are known as *Dyson* (or *quasiparticle*) *orbitals* and represent a parallel of the single particle eigenstates, but now within the many-body setting where they denote the attachment and ionization amplitudes for the added or removed electron. An insightful physical interpretation of the Dyson orbitals is presented in Reference 57 where the authors identify these one-particle states as those that best describe the corresponding excited $(n \pm 1)$-particle states as single particle additions or removals to the original ground state and define the quasiparticle norm as a measure of the validity of this approximation.

Similarly to the single-particle case, where the knowledge of the GF is equivalent to the solution Schrödinger equation, the one-particle GF can be shown to encode many properties of the studied system. However, since we are only considering the one-particle GF, one cannot expect it to be sufficient to access all observables as one would with the knowledge of the full state vector. Rather, the one-particle GF can be shown to give access to all observables in the ground state due to one-body operators and, as a special exception, to the total energy in case the Hamiltonian only contains two-body interactions as shown by the Galitskii–Migdal relations, which relate observables to the residues of the GF.[104] As such, the one-particle GF does not directly imply the full Schrödinger equation but implies a set of one-particle Schrödinger-like eigenvalue equations for the Dyson orbitals. The way to these equations begins by considering a perturbation expansion of the correlated GF. This relies on the separation of the Hamiltonian into a non-interacting one-electron part $\widehat{H}_0$ which gives rise to the non-interacting GF $G_0^{(1)}$ and a two-body interaction $\widehat{V}$ and allows us to write the Dyson equation

$$\begin{aligned} &G^{(1)}(\mathbf{x}, \mathbf{x}', \omega) = \\ &G_0^{(1)}(\mathbf{x}, \mathbf{x}', \omega) + \int\int \mathrm{d}\mathbf{x}'' \mathrm{d}\mathbf{x}''' \; G_0^{(1)}(\mathbf{x}, \mathbf{x}'', \omega) \Sigma(\mathbf{x}'', \mathbf{x}''', \omega) G^{(1)}(\mathbf{x}''', \mathbf{x}', \omega), \end{aligned} \tag{2.19}$$

which intrinsically represents an infinite summation that allows for expressing the full GF in terms of its non-interacting counterpart[104] and the quantity $\Sigma$. This is

known as the irreducible self-energy[f], which contains a multitude of various terms that systematically combine $G_0^{(1)}$ and $\widehat{V}$. In the many-body case, the explicit expression of the perturbation series is extremely cumbersome. In fact, even the lowest-order contributions are so complicated that a new pictorial representation in the form of the so-called Feynman diagrams was developed to simplify the theory and make it easier to navigate. The treatment using diagrammatic expansion is unnecessary in this work; the interested reader is referred to the excellent material in Reference 104. From here, it is straightforward to show that the Dyson equation can be transformed into an eigenvalue equation for the individual Dyson orbitals by inspecting the residues $\lim_{\hbar\omega\to\epsilon_n^{\pm}}(\hbar\omega-\epsilon_n^{\pm})G^{(1)}$ at each corresponding simple pole of the GF for both sides of the Dyson equation. For example, for the hole quasiparticle states, this gives

$$\widehat{H}_0\chi_l^-(\mathbf{x})+\int \mathrm{d}\mathbf{x}'\;\Sigma(\mathbf{x},\mathbf{x}',\epsilon_l^-/\hbar)\chi_l^-(\mathbf{x})=\epsilon_l^-\chi_l^-(\mathbf{x}). \tag{2.20}$$

The electron binding energies seen in the Lehmann representation have been identified as the eigenvalues of these so-called quasiparticle equations; the self-energy plays the role of a non-local energy-dependent interaction potential. It is clear at this point that a multitude of practical computational methods can be created by approximating the exact self-energy.

### 2.2.2 Hartree–Fock method and the correlation energy

One of the simplest yet very important electronic structure methods, which belongs to the family of so-called wavefunction methods, is the Hartree–Fock (HF) approximation. While it can be systematically derived from the diagrammatic expansion of $\Sigma$ (see, for instance, the material in Chapter 10 of Reference 104), here we will adopt the traditional chemist's point of view, discuss its appearance as a consequence of symmetry requirements of the state vector and observe that it eventually yields equations consistent with the Dyson equation. Specifically, the HF method is obtained when the $n$-electron ground state vector is assumed to be expressible in the following form

$$|\psi_{\mathrm{HF}}\rangle=\widehat{a}_n^{\dagger}\widehat{a}_{n-1}^{\dagger}\ldots\widehat{a}_1^{\dagger}\,|0\rangle\,, \tag{2.21}$$

where the operators $\widehat{a}_i^{\dagger}$ represent the fermionic creation operators for each of the $n$ electrons in the system and $|0\rangle$ is the Fock vacuum.[98] This form of the state vector is known as the Slater determinant, and it is the simplest many-body form that respects the Pauli principle by exploiting an antisymmetrized product of auxiliary spin orbitals, $|\chi_i\rangle=\widehat{a}_i^{\dagger}\,|0\rangle$. Since we are using an approximate *Ansatz* of the wave function, the variational principle $E_{\mathrm{HF}}=\langle\psi_{\mathrm{HF}}|\widehat{H}_{\mathrm{e}}|\psi_{\mathrm{HF}}\rangle\geq E_0$ applies and an optimal set of orthonormal spin orbitals can be found by minimizing

[f]The formal explanation of the irreducibility of $\Sigma$ goes well beyond the scope of this thesis. In brief, it is called that way because it only contains the so-called irreducible Feynman diagrams, unlike the related reducible $\Sigma$ which contains all possible diagrams.

the HF energy. This procedure leads to a set of one-body Schrödinger-like Fock equations[106]

$$\widehat{F}\,|\chi_i\rangle \equiv (\widehat{H}_0 + \widehat{V}_{\mathrm{HF}})\,|\chi_i\rangle = \epsilon_i\,|\chi_i\rangle\,, \tag{2.22}$$

where the electron–electron interaction is treated in an effective, mean-field manner through the Fock operator $\widehat{F}$ with $\epsilon_i$ being its eigenvalues which approximate the exact electron addition and removal energies. This operator encompasses all the one-electron terms $\widehat{H}_0$ as well as a new, effective one-electron potential $\widehat{V}_{\mathrm{HF}}$ known as the mean field which approximates the role of $\Sigma$ in the HF theory. Its matrix element is defined as

$$\langle\chi_i|\,\widehat{V}_{\mathrm{HF}}\,|\chi_j\rangle = \sum_{k=1}^{n}\left[\langle\chi_k\chi_i|\,\widehat{V}_{\mathrm{ee}}\left(\widehat{1} + \widehat{P}\right)|\chi_k\chi_j\rangle\right] \tag{2.23}$$

with $\widehat{P}$ being the hermitian two-fermion permutation operator, the action of which is defined as $\widehat{P}\,|\chi_k\chi_j\rangle = -\,|\chi_j\chi_k\rangle$. Since electrons are indeed charged fermions, this effective potential felt by each electron consists not only of the electrostatic (Hartree) repulsion from the remaining electrons (first term in Equation 2.23 corresponding to $\widehat{1}$), but also an additional term known as exchange energy (second term in Equation 2.23 corresponding to $\widehat{P}$) that represents an energy contribution which arises due to the required antisymmetric form of the state vector ansatz. Equations 2.22 and 2.23 constitute the computational engine of the HF method. Note that they represent a self-consistent problem since the Fock operator $\widehat{F}$ has a dependence on the spin-orbitals, but it is also used to calculate them. This kind of solution is known in the theory as self-consistent field (SCF). Formally speaking, the same kind of iterative solution will be encountered in KS-DFT, but the problem is computationally more challenging in the present case because the mean-field part of the Fock operator changes when acting on each orbital individually through the exchange term in Equation 2.23 (*cf.* Equation 2.33).

Finally, the total energy of the $n$-electron system is not simply equal to the sum of the individual eigenvalues of the Fock equations due to the fact that in each of these eigenvalues, the interaction of an electron with all remaining ones is accounted for and a plain sum over them leads to double counting. However, it can be straightforwardly shown[17] to be equal to the following corrected expression

$$E_{\mathrm{HF}} = \sum_{i=1}^{n}\left(\epsilon_i - \frac{1}{2}V_{\mathrm{HF},ii}\right). \tag{2.24}$$

Additional correlation between the electrons that goes beyond the exchange effect is fully neglected by the HF method owing to the use of the mean field. This quality can thus be used to precisely define a quantity known as the correlation energy

$$E_{\mathrm{c}} \equiv E_0 - E_{\mathrm{HF}}. \tag{2.25}$$

The aim to capture as much of $E_{\mathrm{c}}$ as possible is the purpose of correlated electronic structure methods. On one hand, these are represented by advanced (or post-HF) wavefunction methods that do so by systematically mixing excited Slater determinants into the HF ground state. On the other hand, DFT attempts to describe correlation effects by using approximate functionals of electron density, as will be discussed next.

### 2.2.3 Density functional theory

The immediate connection of DFT to the one-electron framework stemming from the Dyson equation is not obvious. This is because in its formal foundation, it replaces the key role of the full ground state vector by the ground state electron density, which is a much simpler and computationally more tractable quantity, and as such remains a many-body theory without any need to invoke one-particle states.[107,108] The following integral of the square modulus of the ground state wavefunction defines the electron density due to the $n$ electrons

$$\rho(\mathbf{r}) \equiv n \sum_{s_1=-1/2}^{+1/2} \int \mathrm{d}\mathbf{x}_2 \ldots \mathrm{d}\mathbf{x}_n \; |\psi_0(\mathbf{x}_1, \ldots, \mathbf{x}_n)|^2. \tag{2.26}$$

and, therefore, is proportional to the probability density of finding any electron at a given position, unlike the square modulus of the wave function that keeps track of the identities of the individual electrons in the correctly antisymmetrized state.

How is it possible that one can replace the wave function with the electron density and still obtain a formally exact theory when information is clearly lost by tracing out dimensions? It was first rigorously shown by Hohenberg and Kohn[34] that a one-to-one mapping exists between the ground state wave function and the electron density and that the wave function can be expressed, at least in principle, as a unique functional of the electron density. Consequently, all expectation values of observables, including the total ground state energy, can be expressed as functionals of electron density as well. Thus, in DFT, the solution of the time-independent Schrödinger equation for the ground state is transformed to a functional minimization problem

$$E_0 = \min_{\rho(\mathbf{r})} \; E[\rho] \tag{2.27}$$

again by exploiting the variational principle. The universal *density functional* $E[\rho]$ is of central importance in the theory and is the key to the exact solution of the electronic problem. However, its explicit analytical form cannot be extracted from the theory. In fact, there is no good reason for this to be possible in this particular case when other formally exact electronic structure theories (think, for instance, the GF framework or post-HF methods such as the configuration interaction[106]) also fail to express the exact solution in a closed form useful for practical calculations.

The best one can do at this point to go through with the present formulation of DFT is to break down the universal functional into the various contributions corresponding to the terms in the electronic Hamiltonian, express everything that can be expressed as an explicit functional of electron density, and approximate the rest. Specifically, this breakdown is

$$E[\rho] = T[\rho] + E_{\mathrm{Hartree}}[\rho] + E_{\mathrm{x}}[\rho] + E_{\mathrm{c}}[\rho] + E_{\mathrm{ext}}[\rho], \tag{2.28}$$

where $T[\rho]$ represents the kinetic energy, $E_{\mathrm{ext}}[\rho]$ is the interaction energy with the nuclei, and the electron–electron interaction has been expressed as a sum of a

classical (Hartree) self-repulsion term, an exchange term and a residual correlation energy term following the above discussion of the (post-)HF treatment of a many-electron system. In this expression, only the Hartree

$$E_{\text{Hartree}}[\rho] = \int\int \mathrm{d}\mathbf{r}\mathrm{d}\mathbf{r}' \; \frac{\rho(\mathbf{r})\rho(\mathbf{r}')}{|\mathbf{r}-\mathbf{r}'|} \equiv \int \mathrm{d}\mathbf{r} \; \rho(\mathbf{r}) V_{\text{Hartree}}(\mathbf{r}) \tag{2.29}$$

and external

$$E_{\text{ext}}[\rho] = \langle\psi_0|\, \widehat{V}_{\text{en}} + \widehat{V}_{\text{nn}} \,|\psi_0\rangle \equiv \int \mathrm{d}\mathbf{r} \; \rho(\mathbf{r}) V_{\text{ext}}(\mathbf{r}) \tag{2.30}$$

terms are analytically expressible as they arise due to the interaction of the electron density with multiplicative, position-dependent, local potentials. Various approximations to the remaining functionals are necessary to obtain practical computational methods.

#### 2.2.3.1 Kohn–Sham DFT

The dominant approach, known as KS-DFT,[109] is built on a mapping of the studied system onto an auxiliary one and subsequent restructuring of the exact density functional that internally also exploits the concept of single-electron orbitals. This allows for creating efficient, practical computational schemes despite the necessity to forfeit the simple and elegant formulation that relies on electron density only. In this approach, one maps the real many-body system onto a fictitious, non-interacting one localized in an effective potential which ensures that both systems share the same electron density. The fictitious KS system is described exactly by a Hartree product[g] of spin orbitals $|\chi_i\rangle$. The reason for this mapping is that the kinetic energy of the KS system is a good approximation to the real kinetic energy and it is straightforward to express it in the basis of the KS spin orbitals as

$$T_{\text{KS}} = \frac{1}{2m_{\text{e}}} \sum_{i=1}^{n} \langle\chi_i|\, \widehat{\mathbf{p}}_i^2 \,|\chi_i\rangle \,, \tag{2.31}$$

thus circumventing the need to know an explicit kinetic energy density functional. Everything unknown, including the correlated remainder of the kinetic energy as well as the exchange and other correlation contributions, is grouped into an overarching quantity known as the exchange–correlation functional

$$E_{\text{xc}}[\rho] \equiv (T[\rho] - T_{\text{KS}}[\rho]) + E_{\text{x}}[\rho] + E_{\text{c}}[\rho] \tag{2.32}$$

with the premise that it can be approximated well — these days, a wide selection of approximate exchange–correlation functionals is available. In order to match the density of the real and the KS system, one simply needs to set the effective KS

[g] Literature often requires the KS wavefunction to take on the form of a Slater determinant. While possible, it does not change any of the underlying algebra due to the missing interaction, adds complexity to the resulting wavefunction, and gives identical kinetic energy.

potential $V_{\mathrm{KS}}(\mathbf{r})$ to that obtained by variation of the sum of the external, Hartree and exchange–correlation functionals with respect to the electron density

$$V_{\mathrm{KS}}(\mathbf{r}) \equiv \frac{\delta E_{\mathrm{Hartree}}[\rho]}{\delta\rho} + \frac{\delta E_{\mathrm{ext}}[\rho]}{\delta\rho} + \frac{\delta E_{\mathrm{xc}}[\rho]}{\delta\rho} = V_{\mathrm{Hartree}}(\mathbf{r}) + V_{\mathrm{ext}}(\mathbf{r}) + V_{\mathrm{xc}}(\mathbf{r}) \quad (2.33)$$

This is trivial for the former two and can be done analytically for a particular choice of the exchange–correlation functional. With this potential, one then solves the KS system by solving a set of effective one-electron Schrödinger-like equations

$$\left(\widehat{T}_{\mathrm{KS}} + \widehat{V}_{\mathrm{KS}}\right) |\chi_i\rangle = \epsilon_i \, |\chi_i\rangle \, . \quad (2.34)$$

Once again, the KS equations take on a form consistent with the Dyson equations, where the role of $\Sigma$ is being taken by the local KS potential. A formal bridge that links KS-DFT with the exact self-energy operator is represented by the Sham–Schlütter equation, which relates the two quantities.[108,110] The obtained set of orbitals gives rise to an electron density

$$\rho(\mathbf{r}) = \sum_{s=-1/2}^{+1/2} \sum_{i=1}^{n} \langle \mathbf{x}|\chi_i\rangle \, \langle \chi_i|\mathbf{x}\rangle \, . \quad (2.35)$$

Note that also in this case, the KS equations represent an SCF-type of problem, since the KS potential can be obtained only with prior knowledge of the electron density. However, unlike in HF where one has to deal with the non-local mean field, here we are dealing with a local potential, which makes the calculation generally less demanding and, at the same time, allows us to estimate $E_{\mathrm{c}}$.

#### 2.2.3.2 Hierarchy of approximate functionals

The hierarchy of practical exchange–correlation functionals is often compared to the concept of Jacob's ladder,[111] in which various approximations are ordered by ascending accuracy. The relatively least accurate exchange–correlation functionals are fully local and are notably represented by the local density approximation (LDA) functionals[112] which treat a system as a locally constant-density homogeneous electron gas. A step higher is achieved by the family of semi-local exchange–correlation functionals,[113] which incorporate various differential quantities derived from the electron density to account for the effect of local surroundings. Semi-local functionals in the form of the GGA are widely used in molecular electronic-structure calculations with success, and their still relatively simple form has the advantage of high computational efficiency. To highlight a few notable GGA functionals, we should not forget to mention the Perdew–Burke–Erznerhof (PBE) functional,[114] its revPBE revision[115] and the Becke–Lee–Yang–Parr (BLYP) functional.[116,117] However, semi-local functionals are known to suffer from an effect known as *self-interaction error*:[63] in HF exchange (often referred to as *exact exchange* in the DFT context) the self-interaction energy of an electron exactly vanishes as $\langle \chi_i\chi_i| \, \widehat{V}_{\mathrm{ee}} \left(\widehat{1} + \widehat{P}\right) |\chi_i\chi_i\rangle = 0$, but the approximate exchange functional used semi-local DFT does not fully cancel with the exact contribution

from the Hartree term, leaving behind a spurious, non-physical self-interaction. This gives rise to noticeable artifacts such as, for example, the lengthening of covalent bonds[4] or over-delocalization of excess electrons in open-shell systems.[62,71] These shortcomings are significantly improved by hybrid functionals,[114] which incorporate a fraction of exact exchange into the semilocal exchange functional. These functionals come in two flavors:

1. *global* hybrids, where the target exchange energy is a simple linear combination of the semilocal and HF contributions

$$E_{\mathrm{x}}[\rho] = \alpha E_{\mathrm{x}}^{\mathrm{HF}}[\{|\chi_i\rangle\}] + (1-\alpha)E_{\mathrm{x}}^{\mathrm{GGA}}[\rho], \quad 0 \leq \alpha \leq 1 \tag{2.36}$$

2. *range-separated* hybrids,[118] where the interaction potential $V_{\mathrm{ee}}(r)$ (with $r = |\mathbf{r} - \mathbf{r}'|$) is split using an appropriate range-separating function, *e.g.*

$$V_{\mathrm{ee}}(r) = \mathrm{erfc}(\gamma r)V_{\mathrm{ee}}(r) + [1 - \mathrm{erfc}(\gamma r)]V_{\mathrm{ee}}(r), \tag{2.37}$$

   and one term is used to evaluate the exact exchange and the other to evaluate the remaining GGA contribution; $\gamma$ is a tunable range-separation parameter.

The hybrid generalizations of the aforementioned GGA functionals known as PBE0[119] and B3LYP[120] represent important examples of global hybrids. The inclusion of exact exchange makes calculations employing hybrid functionals significantly computationally more demanding than those at the GGA level.

#### 2.2.3.3 Dispersion in DFT

A major remaining shortcoming of hybrid DFT is its inability to include nonlocal correlation effects such as dispersion (London) forces, especially in weakly bonded systems where such interactions play a key role. The so-called London–Eisenschitz formula, obtained using second-order perturbation theory,[2] states that the asymptotic behavior of energy thanks to the dispersion interaction between two atoms (say 1 and 2) at long distances is

$$E_{\mathrm{D}}(R) = -\frac{3}{2}\frac{I_1 I_2}{I_1 + I_2}\alpha_1\alpha_2\frac{1}{R^6} \equiv -\frac{C_6^{(12)}}{R^6} < 0, \tag{2.38}$$

where $I_J$ and $\alpha_J$ denote the ionization potential and static polarizability of atom $J$ and $R$ the interatomic distance, giving the well-known $R^{-6}$ asymptotic behavior of the interaction scaled by the dispersion coefficient $C_6$. In practice, the description of non-covalent interactions is often treated empirically for general molecular systems. One of the most popular approaches to this end is the DFT-D class of methods,[121–123] where the total energy, including the contribution of dispersion interactions, is obtained by subtracting a correction to the raw KS energy

$$E_{\mathrm{DFT-D}}[\rho] = E[\rho] - E_{\mathrm{D}}(\mathbf{R}), \tag{2.39}$$

where the overall dispersion correction is obtained as a sum over pairwise dispersion interactions

$$E_{\mathrm{D}}(\mathbf{R}) = \sum_{IJ} \sum_{n} s_n f_n(R_{IJ}) \frac{C_n^{(IJ)}(\mathbf{R})}{R_{IJ}^n}, \quad n = 6, 8, 10 \ldots . \tag{2.40}$$

Here, $s_n$ is a density-functional-dependent scaling coefficient, and $f_n$ is the so-called damping function: both are employed to sanitize the numerical behavior of the correction at short distances since the $R^{-6}$ tail only holds for large separations. The dispersion coefficients are obtained from empirical mixing rules or using *ab initio* calculations. In the simpler DFT-D1[121] and DFT-D2[122] methods the coefficients are without dependence on the molecular geometry; the commonly used, newer DFT-D3[123] method introduces coefficients that depend on the chemical environment of individual atoms through coordination numbers. Specifically concerning this work, the so-called revPBE0-D3[124] global hybrid functional has been shown to perform very well for liquid condensed systems with hydrogen bonds and, as such, is the principal exchange–correlation functional of choice.

Apart from DFT-D, other possibilities to address dispersion interactions exist, such as the Tkatchenko–Scheffler[125] or the many-body dispersion (MBD)[126] methods, to name a few. A more systematic effort to describe these weak bonding interactions is seen, for instance, in the fully non-local van-der-Waals density functionals;[127–129] these are not used in this work.

### 2.2.4 Accurate electron binding energies and the GW approximation

As both the HF theory and KS-DFT formally represent approximations to the Dyson equation, the orbital energies appearing in those theories can be interpreted as approximations of electron binding energies.[130,131] However, an unfortunate practical experience remains that estimates of electron binding energies from HF and DFT orbital energies compared to experimental data are usually poor. Since a major part of this work is focused on the modeling of XPS spectra, we are in need of an electronic structure method that is able to give a more rigorous picture of the energetics of electron binding in molecular systems. One such method is known as the GW approximation[57,66,104,132] and takes us back to explicit attempts to approximate the irreducible self-energy within many-body perturbation theory. Its name is derived from the fact that it approximates $\Sigma$ as the following convolution

$$\Sigma(\mathbf{x}, \mathbf{x}', \omega) \approx \frac{i}{2\pi} \int \mathrm{d}\omega' \; G^{(1)}(\mathbf{x}, \mathbf{x}', \omega - \omega') W(\mathbf{x}, \mathbf{x}', \omega) \tag{2.41}$$

of the one-particle GF with the dynamically screened Coulomb interaction $W$. The root of this quantity lies deep within many-body perturbation theory,[132] and we will not be spending excessive time on the discussion of its exact origin since it goes beyond the presently relevant concept of one-particle GF. However, we note two important things about $W$

1. It can be calculated from the Dyson orbitals and, as such, carries information about electron correlation.[132]

2. It can be shown that employing the bare Coulomb potential $\widehat{V}_{\mathrm{ee}}$ instead of $W$ reduces the above $\Sigma$ exactly to $\widehat{V}_{\mathrm{HF}}$.[104,132]

As such, the GW theory can be understood as HF theory augmented by additional correlation effects.

Once again, we are standing in front of a self-consistent problem since the Dyson orbitals and their corresponding energies are not known at the entry to the calculation. This is approached trivially in the $G_0W_0$ variation[66] of the GW approximation, which exploits the knowledge of an easily accessible set of orbitals (typically KS orbitals) and treats the target quasiparticle energies using first-order perturbation theory and linearization of the Dyson equation. Specifically, one can clearly write

$$\Sigma(\mathbf{x},\mathbf{x}',\omega) = V_{\mathrm{KS}}(\mathbf{x}) + [\Sigma(\mathbf{x},\mathbf{x}',\omega) - V_{\mathrm{KS}}(\mathbf{x})] \tag{2.42}$$

and, assuming that the KS framework is an acceptable approximation to the true GW $\Sigma$, consider the term inside parentheses as a small perturbation. Then, the GW binding energy approached using the first order of perturbation theory is the following simple correction

$$\epsilon_i^{\mathrm{GW}} \approx \epsilon_i + \int\int \mathrm{d}\mathbf{x}\mathrm{d}\mathbf{x}'\ \chi_i^*(\mathbf{x}')\left[\Sigma(\mathbf{x},\mathbf{x}',\epsilon_i^{\mathrm{GW}}/\hbar) - V_{\mathrm{KS}}(\mathbf{x})\delta(\mathbf{x}-\mathbf{x}')\right]\chi_i(\mathbf{x}). \tag{2.43}$$

The problem with this expression is that it still contains a self-consistency issue, as one needs to evaluate the self-energy at a frequency given by the GW binding energy. This is approached by a local linearization of the energy dependence of the self-energy that is justified by the same argument as the use of perturbation theory itself: that the two energies are close enough. Then,

$$\Sigma(\mathbf{x},\mathbf{x}',\epsilon_i^{\mathrm{GW}}/\hbar) \approx \Sigma(\mathbf{x},\mathbf{x}',\epsilon_i/\hbar) + \left(\epsilon_i^{\mathrm{GW}} - \epsilon_i\right)\left.\frac{\partial\Sigma}{\partial\omega}\right|_{\omega=\epsilon_i/\hbar} \tag{2.44}$$

and by combining the last two expressions, one obtains

$$\epsilon_i^{\mathrm{GW}} \approx \epsilon_i + Z_i\int\int \mathrm{d}\mathbf{x}\mathrm{d}\mathbf{x}'\ \chi_i^*(\mathbf{x}')\left[\Sigma(\mathbf{x},\mathbf{x}',\epsilon_i/\hbar) - V_{\mathrm{KS}}(\mathbf{x})\delta(\mathbf{x}-\mathbf{x}')\right]\chi_i(\mathbf{x}). \tag{2.45}$$

where

$$Z_i = \frac{1}{1 - \int\int \mathrm{dx}\mathrm{dx}'\ \chi_i^*(\mathbf{x}')\frac{\partial\Sigma}{\partial\omega}\big|_{\omega=\epsilon_i/\hbar}\chi_i(\mathbf{x})} \tag{2.46}$$

is a normalization factor related to the quasiparticle norm discussed in Reference 57. Therefore, within a course of a DFT-based $G_0W_0$ calculation (usually denoted as $G_0W_0$@DFT), a set of KS orbitals is used to set up both $G_0$ and $W_0$. These are then used to construct the self-energy $\Sigma$ and approximate the corresponding quasiparticle energies. The slightly more advanced eigenvalue-iteration evGW method,[66] which iteratively converges the eigenvalues while leaving the orbitals untouched, as well as other flavors of GW that rely on a fully self-consistent treatment of both the quasiparticle states and the corresponding eigenenergies, are not used in this work.

### 2.2.5 Practical calculations with orbital-based methods

The main one-electron equations of the HF and KS methods and the energy corrections of the $G_0W_0$ method describe the essence of how the particular methods work. However, since in their above form, they are differential equations involving wave functions on a combined Hilbert space of the spatial and spin coordinates $\mathbf{x}$, they do not represent a practical prescription to employ those methods in a computational treatment using spatial wavefunctions.

#### 2.2.5.1 Treatment of the spin coordinate

To transform the one-electron equations into a practical form, a factorized form must be assumed for the spin orbitals $\{|\chi_i\rangle\}$. For bound states, the one-electron Hilbert space $\mathcal{H}_\mathrm{e}^{(1)}$ (with $\mathcal{H}_\mathrm{e} = \mathcal{H}_\mathrm{e}^{(1)} \otimes \cdots \otimes \mathcal{H}_\mathrm{e}^{(n)}$) is composed of the vector space of square-integrable spatial wavefunctions and a two-dimensional complex Euclidean space of spin states $\mathcal{L}^2(\mathbb{R}^3) \otimes \mathbb{C}^2$, where the latter has a simple basis $|\alpha\rangle \equiv (1,0)^T$ and $|\beta\rangle \equiv (0,1)^T$ that corresponds to the so-called spin-up and spin-down states. Since $\widehat{H}_\mathrm{e}$ contains no spin-dependent terms, it commutes with both the total spin operator $\widehat{\mathbf{S}}^2$ and the spin-projection $\widehat{S}_z$ in the $n$-electron system

$$\left[\widehat{H}_\mathrm{e}, \widehat{\mathbf{S}}^2\right] = \left[\widehat{H}_\mathrm{e}, \widehat{S}_z\right] = 0. \tag{2.47}$$

Together with the fundamental commutation $\left[\widehat{\mathbf{S}}^2, \widehat{S}_z\right] = 0$, this implies that all three operators share the same set of eigenstates and, therefore, the exact ground state is a spin-pure state with a well-defined value of quantum numbers $S$ and $M_S$ corresponding to $\widehat{\mathbf{S}}^2$ and $\widehat{S}_z$. As clarified above, the HF and KS approximations to this state are not exact eigenstates of the electronic Hamiltonian. Still, they can be constructed as an eigenstate of the two spin operators and, therefore, to comply with fundamental physical requirements. Doing so for the $\widehat{S}_z$ operator is straightforward as it only requires placing each electron into either $|\alpha\rangle$ or $|\beta\rangle$ spin state, which are themselves eigenstates on each individual single-particle subspace, and simultaneous $\widehat{\mathbf{S}}^2$-eigenstates are obtained by taking appropriate linear combinations over the corresponding degenerate subspaces. However, ensuring the eigenstate nature with respect to $\widehat{\mathbf{S}}^2$ places requirements on the spatial parts, although the operator is not explicitly dependent on it. Specifically, this requires *restricted* spin-orbitals

$$|\chi_i\rangle, |\chi_j\rangle \to |\varphi_k\rangle \otimes \begin{cases} |\alpha\rangle \\ |\beta\rangle, \end{cases} \quad k \in 1, \ldots, \frac{n}{2} \tag{2.48}$$

where a shared spatial part is populated by two electrons with opposite spins. For closed-shell systems, the single-determinant restricted ground state is always a $\widehat{\mathbf{S}}^2$-eigenstate. For systems with open-shells, the restricted open-shell ground state is a $\widehat{\mathbf{S}}^2$-eigenstate only if the unpaired electrons have parallel spins.[106] However, the imposed constraint in restricted spin orbitals may cause them to not be the optimal variational solution in open-shell systems. A state with a lower energy

can be obtained by using unrestricted spin orbitals

$$|\chi_i\rangle, |\chi_j\rangle \rightarrow \begin{cases} |\varphi_k^\alpha\rangle \otimes |\alpha\rangle \\ |\varphi_l^\beta\rangle \otimes |\beta\rangle, \end{cases} \quad k \in 1, \ldots, n_\alpha, l \in 1, \ldots, n_\beta \tag{2.49}$$

where spatial parts can vary freely. Unrestricted determinants are not exact $\widehat{\mathbf{S}}^2$-eigenstates. The measure of how much they deviate from the exact eigenstates is known as spin contamination and can be used to assess the quality of the unrestricted ground state.[106]

In the HF method, the use of restricted orbitals allows for integration over the spin subspace that leads to the following new, spatial-only formulation of the Fock equations

$$\left(\widehat{H}_0 + \widehat{V}_{\mathrm{HF}}\right) |\varphi_i\rangle = \epsilon_i |\varphi_i\rangle, \tag{2.50}$$

where the mean-field operator now reads

$$\langle\varphi_i| \widehat{V}_{\mathrm{HF}} |\varphi_j\rangle = \sum_{k=1}^{n/2} \langle\varphi_k\varphi_i| \widehat{V}_{\mathrm{ee}} \left(2 \cdot \widehat{1} - \widehat{P}\right) |\varphi_k\varphi_j\rangle. \tag{2.51}$$

A new factor of 2 appeared in the Hartree term due to the double occupation of each restricted HF (RHF) orbital. The lack of this factor in the exchange term is then because the exchange interaction only affects electrons with identical spins. The restricted formulation allows the optimization of only half the number of orbitals than there are electrons and, therefore, is rather computationally efficient, but, on the other hand, it is fundamentally restricted to closed-shell ground state calculations in this form (restricted open-shell calculations are possible, but more complicated[106]). Similarly, in an unrestricted HF (UHF) calculation, one needs to solve two sets of Fock equations for the $\alpha$, and $\beta$ spins, which are coupled through the dependence of the mean field on the orbitals with the opposite spin

$$\begin{aligned} \langle\varphi_i^{\alpha/\beta}| \widehat{V}_{\mathrm{HF}} |\varphi_j^{\alpha/\beta}\rangle = &\sum_{k=1}^{n_{\alpha/\beta}} \langle\varphi_k^{\alpha/\beta}\varphi_i^{\alpha/\beta}| \widehat{V}_{\mathrm{ee}} \left(\widehat{1} - \widehat{P}\right) |\varphi_k^{\alpha/\beta}\varphi_j^{\alpha/\beta}\rangle \\ &+ \sum_{k=1}^{n_{\beta/\alpha}} \langle\varphi_k^{\beta/\alpha}\varphi_i^{\alpha/\beta}| \widehat{V}_{\mathrm{ee}} |\varphi_k^{\beta/\alpha}\varphi_j^{\alpha/\beta}\rangle \end{aligned} \tag{2.52}$$

as the Hartree interaction between the different spin projections needs to be accounted for. This can be understood as partitioning the 2-factor seen in the RHF formulation between the spin subsystems that can now be populated unequally.

To allow for open-shell DFT calculations, the approximate functionals are usually formulated in terms of two densities $\rho_\alpha(\mathbf{r}) = \sum_{k=1}^{n_\alpha} |\varphi_k^\alpha(\mathbf{r})|^2$ and $\rho_\beta(\mathbf{r}) = \sum_{l=1}^{n_\beta} |\varphi_l^\beta(\mathbf{r})|^2$ constructed individually using the appropriate KS orbitals to correctly incorporate the spin-dependent exchange and correlation effects

$$E = E[\rho_\alpha, \rho_\beta]. \tag{2.53}$$

This formulation is known as spin-polarized DFT.[108] Clearly, the electron density in terms of these densities is just

$$\rho(\mathbf{r}) = \rho_\alpha(\mathbf{r}) + \rho_\beta(\mathbf{r}). \tag{2.54}$$

It is useful to define a new quantity at this point

$$\rho_{\mathrm{s}}(\mathbf{r}) \equiv \rho_{\alpha}(\mathbf{r}) - \rho_{\beta}(\mathbf{r}) \tag{2.55}$$

called the *spin density*, which is, like the electron density, a measurable observable and receives a considerable amount of attention later in the course of this work. $\rho(\mathbf{r})$ and $\rho_{\mathrm{s}}(\mathbf{r})$ are complementary quantities in the sense that spin-DFT can be formulated in their terms as an alternative to $\rho_{\alpha}(\mathbf{r})$ and $\rho_{\beta}(\mathbf{r})$. In the context of the restricted KS (RKS) theory, the partitioning is only formal, as clearly $\rho_{\alpha}(\mathbf{r}) = \rho_{\beta}(\mathbf{r}) = \frac{1}{2}\rho(\mathbf{r})$ and $\rho_{\mathrm{s}}(\mathbf{r}) = 0$ and the whole framework can be formulated in terms of the electron density and $n/2$ restricted spin-orbitals. In the unrestricted KS (UKS) version, one again solves two sets of KS equations for $n_{\alpha}$ and $n_{\beta}$ electrons, which are coupled by the total electron density $\rho(\mathbf{r})$ that is contained in both sets.

#### 2.2.5.2 Periodic systems

Up to this point, we have formulated the theory in terms of finite systems, which are characterized by a number of discrete quantum states with sharp energy eigenvalues. However, it is often appropriate to apply periodic boundary conditions (PBCs) either to naturally describe a crystal structure or to approximate the disordered condensed phase with a finite representation of the system. In the realm of electronic structure theory, this leads to the emergence of Bloch states and band structure, where one no longer has discrete energy levels but locally continuous regions of allowed energies, *i.e.*, bands, that contain an infinity of possible states.[17] This behavior is captured by the Bloch theorem, which clarifies that a state in a periodic potential (which in our case would correspond to an effective one-electron potential, such as $V_{\mathrm{KS}}$, where the periodicity would be given by the periodically repeated nuclear positions due to PBCs) has the form of

$$\varphi_{j\mathbf{k}}(\mathbf{r}) = e^{\mathrm{i}\mathbf{k}\cdot\mathbf{r}} u_{j\mathbf{k}}(\mathbf{r}), \tag{2.56}$$

where $j$ is the band index (which corresponds to the previous orbital labels), $u_{j\mathbf{k}}(\mathbf{r})$ is a spatial function with the same periodicity as the underlying potential and $\hbar\mathbf{k}$ is the so-called quasimomentum vector defined on the reciprocal space. In other words, each state can be expressed as a wave function that consists of a periodic part and a plane wave, which does not need to have the same periodicity as the underlying potential. Therefore, the complete wavefunction also does not need to have that same periodicity, specifically

$$\varphi_{j\mathbf{k}}(\mathbf{r} + \mathbf{a}_i) = e^{\mathrm{i}\mathbf{k}\cdot\mathbf{a}_i} \varphi_{j\mathbf{k}}(\mathbf{r}), \tag{2.57}$$

given a lattice vector $\mathbf{a}_i$, $i = 1, 2, 3$. This puts a bound on the extent of quasimomenta that need to be considered, as the only non-trivial contributions come from $\mathbf{k} \in [-2\pi/\mathbf{a}_i, 2\pi/\mathbf{a}_i]$: a polygon in reciprocal space known as the first Brillouin zone. In effect, all quantities previously expressed as a sum over orbitals in a finite system now need to be reformulated as a sum over bands together with an integral over the first Brillouin zone in a periodic system. In a practical

setting, the Brillouin zone is normally discretized into individual **k**-points, and the convergence of the target quantities with the **k**-point grid is observed. Taking only the most symmetric point in $\mathbf{k} = \mathbf{0}$ is known as a Γ-point calculation, which only features discrete states with no dispersion.

#### 2.2.5.3 Basis sets

Now that we removed the spin dependence from the spin orbitals, the next step is introducing a fixed basis set that transforms the differential character of the one-electron equations into a matrix-based formulation that is more suitable for computational treatment. First, let us assume a finite basis $\{|\alpha_n\rangle\,,\ n = 1, \ldots, n_{\text{basis}}\}$; specific choices will be discussed once the general framework is clarified. The basis is not necessarily orthonormal and, therefore, a non-trivial overlap matrix exists and is given by

$$S_{mn} = \langle \alpha_m | \alpha_n \rangle \,. \tag{2.58}$$

An orbital can be expanded using such basis as

$$|\varphi_i\rangle = \sum_{n=1}^{n_{\text{basis}}} |\alpha_n\rangle \langle \alpha_n | \varphi_i \rangle \equiv \sum_{n=1}^{n_{\text{basis}}} c_{ni} |\alpha_n\rangle \,. \tag{2.59}$$

Then, inserting this expansion into the respective HF or KS equations (formally, they take on the same form, so we shall discuss both in terms of a general one-particle Hamiltonian $\widehat{F}$ that we borrow for this purpose from the HF context) along with appropriate identities gives

$$\sum_{n=1}^{n_{\text{basis}}} F_{mn} c_{ni} = \epsilon_i \sum_{n=1}^{n_{\text{basis}}} S_{mn} c_{ni}, \tag{2.60}$$

which can be expressed equivalently in matrix form as

$$\mathbb{FC} = \mathbb{ESC}. \tag{2.61}$$

In the last expression, $\mathbb{F}$ represents the Fock or KS matrix, $\mathbb{S}$ is the overlap matrix, $\mathbb{C}$ is a column matrix

$$\mathbb{C} = (\mathbf{c}_1, \mathbf{c}_2, \ldots, \mathbf{c}_{n_{\text{basis}}}) \tag{2.62}$$

of coefficient vectors $\mathbf{c}_n$ that represent the orbitals, and $\mathbb{E}$ is the diagonal matrix of energies $\epsilon_i$. This matrix formulation of the one-electron equations is known, especially in the HF context, as the Roothaan–Hall equation.[106] It represents a bridge between the solution of the electronic problem and methods of linear algebra. Note that introducing a fixed basis set into the one-electron equations leads to the need to compute the so-called four-center electron repulsion integrals (ERIs) to evaluate the Hartree and, notably, the exchange term. These integrals adopt the following form in the position representation

$$\langle kl | mn \rangle \equiv \int\int \mathrm{d}\mathbf{r}\mathrm{d}\mathbf{r}' \ \alpha_k^*(\mathbf{r}) \alpha_l^*(\mathbf{r}') \frac{1}{|\mathbf{r} - \mathbf{r}'|} \alpha_m(\mathbf{r}) \alpha_n(\mathbf{r}')$$

and, due to the combinatorics of the four contributing indices, their number grows rapidly with increasing size of the basis set as $O(n_{\text{basis}}^4)$.[106] As such, they represent the reason for unfavorable scaling of methods where the evaluation of exact exchange energies is required.

Commonly, the basis expansion is formulated using the linear combination of atomic orbitals (LCAO) approach.[106,133] Here, the basis set comprises suitably defined functions localized on the individual atomic nuclei of the studied system. The choice of the specific form of the basis functions is to a certain degree arbitrary, since atoms (except hydrogen) do not have an exactly solvable set of atomic orbitals, and, after all, the basis itself has no physical meaning and only needs to cover the underlying Hilbert space well. However, practical basis sets are often motivated by the fundamental behavior of electrons hydrogen-like atoms since this provides a physically founded starting point and, therefore, an easier convergence to the desired result. A particularly computationally efficient variation of the exact hydrogen-type orbitals (also known as Slater-type orbitals) is the Gaussian-type orbitals. Here, each basis function is defined as a product of a radial part and a spherical harmonic function

$$\alpha_i(\mathbf{r}) = \alpha_i(r, \theta, \phi) \propto r^l e^{-\zeta r^2} Y_{lm}(\theta, \phi), \tag{2.63}$$

but the exact exponentially decaying radial part of the hydrogen atom[133] is replaced with a Gaussian with a width given by the exponent $\zeta$. Note that the origin of the spherical coordinate system for each basis function is located on a nucleus. This significantly simplifies the evaluation of the four-center integrals due to the simple rules of Gaussian multiplication and opens the door to efficient integral evaluation methods as, for instance, the Obara–Saika recursion scheme.[134] In comparison to hydrogen-type orbitals, the plain Gaussian basis tends to behave incorrectly at very large and very small distances from the nuclei.[106] This is often corrected by defining a single basis function as a *contraction*, or a linear combination, of several primitive Gaussians to better approximate the expected asymptotics. Another layer of flexibility in Gaussian basis sets is achieved by reserving more than one basis function to represent an orbital, typically in the valence region, which corresponds most strongly to chemical bonding. This design is known as a split-valence basis and is commonplace in modern practical calculations; the specific number of functions used for this purpose gives rise to the often-heard double–, triple-$\zeta$ nomenclature, or similar. LCAO basis sets can be implemented analytically in the sense of the above or numerically tabulated.

For calculations under PBCs, a plane wave basis set represents an efficient alternative choice to LCAO. Here, the Bloch state is expanded into a Fourier series of plane waves $e^{\mathrm{i}\mathbf{G}\cdot\mathbf{r}}$, $\mathbf{G} \in \mathbb{Z}$ with the lattice periodicity

$$\varphi_{j\mathbf{k}}(\mathbf{r}) = \frac{1}{\sqrt{\Omega}} \sum_{\mathrm{G}} c_{j\mathbf{k}}(\mathbf{G}) e^{\mathrm{i}(\mathbf{k}+\mathbf{G})\cdot\mathbf{r}}, \tag{2.64}$$

where $\Omega$ is the unit cell volume. Plane-wave basis sets are orthonormal and independent of the underlying molecular structure, which improves certain shortcomings of LCAO basis sets, such as the superposition error. In practice, the

basis set is truncated at a chosen maximum value of $\mathbf{G}$: typically, the control parameter is given as an energy value in Rydberg units, defined as

$$E_{\text{cutoff}} = \frac{h^2 c^2}{2} |\mathbf{G}_{\text{max}}|^2. \tag{2.65}$$

#### 2.2.5.4 Software choices

The main computational engine in this work is the CP2K software.[135] Through its Quickstep module,[136] it features a particularly efficient implementation of DFT electronic structure based on the Gaussian and plane waves (GPW) method. Here, one uses a dual basis of LCAO Gaussian basis set to represent the KS orbitals and plane waves to represent the electron density. This allows for an effectively linear-scaling performance for GGA functionals by avoiding the need to calculate ERIs while evaluating the Hartree energy by using fast Fourier transforms and solving the Poisson equation in reciprocal space. Hybrid DFT, which requires the evaluation of exact exchange energies, is also available as a highly efficient implementation.[137–139] CP2K also gives access to post-HF methods such as $G_0W_0$[66] and allows for calculations with C-NNPs. Due to its efficiency, CP2K is appropriate notably for *ab initio* calculations of extended periodic systems such as liquids and solids.[33]

To a lesser extent, we rely on the FHI-aims software[140] to perform calculations of molecules bound to metallic slabs. This package uses numerical atom-centered basis sets[140] and is designed for optimized calculations with this particular system geometry by allowing for thick vacuum regions with essentially no computational overhead and advanced dipole corrections for asymmetric surface slabs.[141]

## 2.3 | The nuclear problem

Once electronic structure methods have been established, one is, in principle, equipped to address the properties of the nuclei, which represents the second half of the Born–Oppenheimer approximation. While the need to address issues connected to the indistinguishable fermionic nature of the electrons is alleviated here since nuclei can normally be considered distinguishable at the range of temperatures of interest, a new complication appears that can be motivated experimentally. In electronic spectroscopy, which mainly probes the eigenvalue spectrum of the electronic Hamiltonian, a typical separation between the energy levels is at the eV level. This large magnitude of separation causes, even at ambient conditions, the equilibrium thermal population of excited electronic states to be negligible and makes the problem open to ground-state-only theories such as DFT. On the other hand, the nuclear (also known as vibrational) levels, as explored by vibrational spectroscopy and traditionally measured in $\text{cm}^{-1}$, exhibit separations smaller by one or several orders of magnitude. This makes the thermal populations of excited vibrational states non-negligible even at significantly colder than room temperatures. In turn, one must turn to statistical approaches to account for this new source of uncertainty.

### 2.3.1 Statistical mechanics

The central quantity in quantum statistical mechanics is the density matrix operator $\widehat{\rho}$.[17] The power of the density matrix formalism becomes apparent when dealing with a statistical mixture of states where the concept of a pure single state becomes insufficient. Here, the density matrix is defined as a sum of projectors on the states contributing to the statistical mixture

$$\widehat{\rho} \equiv \sum_i w_i \left|\phi_i\right\rangle \left\langle\phi_i\right| \tag{2.66}$$

weighted by their corresponding statistical probabilities $w_i$. As such, the density matrix can be understood as a generalization of the concept of a pure quantum state which seamlessly reduces to that concept when only a single state is statistically relevant. In a canonical ensemble, the only statistical ensemble treated explicitly in this work, the statistical probability $w_i$ of finding the $i$-th state in the mixture is given by the Boltzmann factor $e^{-\beta E_i}$ where $\beta$ is the inverse temperature $(k_\mathrm{B}T)^{-1}$. In turn, exploiting the eigenvalue decomposition of an operator reveals that the canonical density matrix can be written as

$$\widehat{\rho}(\beta) = \sum_i e^{-\beta E_i} \left|\phi_i\right\rangle \left\langle\phi_i\right| = e^{-\beta \widehat{H}} \tag{2.67}$$

This concept allows us to neatly address the expectation values of an observable $\widehat{A}$ in a mixed-state system as a Boltzmann-weighted average of the expectation value of $\widehat{A}$ in each contributing state

$$\langle A \rangle = \frac{\sum_i e^{-\beta E_i} \left\langle\phi_i\right| \widehat{A} \left|\phi_i\right\rangle}{\sum_i e^{-\beta E_i}} = \frac{\mathrm{Tr}\, \widehat{A}\widehat{\rho}(\beta)}{\mathrm{Tr}\, \widehat{\rho}(\beta)}. \tag{2.68}$$

The normalization of the Boltzmann probabilities

$$Q(\beta) \equiv \mathrm{Tr}\, \widehat{\rho}(\beta) \tag{2.69}$$

is the canonical quantum partition function, which provides a link to the macroscopic properties of the system through the usual thermodynamic relations.[31]

#### 2.3.1.1 Imaginary time path integral formulation

To prepare the ground for practical computational methods, we will now introduce an alternative formulation for the partition function $Q(\beta)$ using the Feynman path integral formalism. While this approach was originally formulated as a real-time method,[30] it was later shown[142] that it can be seamlessly recast for the density matrix using a Wick rotation between real and imaginary time, $t \to \tau \equiv it$, since the canonical density matrix is exactly equivalent to the imaginary time evolution operator

$$\widehat{\rho}(\beta) = \widehat{U}(-i\hbar\beta) \tag{2.70}$$

for $\tau = \hbar\beta$. Let us first express the trace-based definition of the partition function in the position basis as

$$Q(\beta) = \int \mathrm{d}\mathbf{R}^{(1)} \ \left\langle\mathbf{R}^{(1)}\right| e^{-\beta \widehat{H}} \left|\mathbf{R}^{(1)}\right\rangle = \int \mathrm{d}\mathbf{R}^{(1)} \ \left\langle\mathbf{R}^{(1)}\right| e^{-\beta(\widehat{T}+\widehat{E}_0)} \left|\mathbf{R}^{(1)}\right\rangle. \tag{2.71}$$

By employing the symbol $\widehat{E}_0$, we restrict the subsequent discussion to electronic ground state PESs. For reasons that will become clear shortly, we are calling the nuclear position vector $\mathbf{R}^{(1)}$ instead of the previous, more general $\mathbf{R}$. To proceed further, we note that the two terms of the Hamiltonian do not commute, and an appropriate factorization of the exponential, such as the symmetric Trotter formula,[143] is needed. Applying it, we obtain

$$Q(\beta) = \lim_{P\to\infty} \int \mathrm{d}\mathbf{R}^{(1)} \, \langle \mathbf{R}^{(1)} | \left( e^{-\frac{\beta \widehat{E}_0}{2P}} e^{-\frac{\beta \widehat{T}}{P}} e^{-\frac{\beta \widehat{E}_0}{2P}} \right)^P | \mathbf{R}^{(1)} \rangle \,, \tag{2.72}$$

which we extend further by inserting a position-represented identity relation $\int \mathrm{d}\mathbf{R}^{(i+1)} \, |\mathbf{R}^{(i+1)}\rangle \, \langle \mathbf{R}^{(i+1)}|$ between each $i$-th and $(i+1)$-th pair of the $P$ consecutive operators above. Each resulting integral is transformed by inserting another momentum-represented identity relation to an analytically solvable Gaussian integral. Performing the integration yields the following closed formula[31] for the partition function

$$Q(\beta) = \lim_{P\to\infty} \prod_{I=1}^{N} \left( \frac{M_I P}{2\pi\beta\hbar^2} \right)^{\frac{3P}{2}} \int \mathrm{d}\mathbf{R}^{(1)} \ldots \mathrm{d}\mathbf{R}^{(P)} \; e^{-\beta U_P(\mathbf{R}^{(1)},\ldots,\mathbf{R}^{(P)})} \tag{2.73}$$

with momenta fully integrated out. The corresponding temperature-dependent potential $U_P$ is

$$U_P(\mathbf{R}^{(1)},\ldots,\mathbf{R}^{(P)}) \equiv \sum_{i=1}^{P} \left\{ \sum_{I=1}^{N} \left[ \frac{1}{2} M_I \omega_P^2 \left| \mathbf{R}_I^{(i+1)} - \mathbf{R}_I^{(i)} \right|^2 \right] + \frac{1}{P} E_0(\mathbf{R}^{(i)}) \right\}, \tag{2.74}$$

where the first sum going up to $P$ is subject to cyclic boundary conditions, which ensure that $\mathbf{R}^{(P+1)} = \mathbf{R}^{(1)}$. This is an analogy of a classical partition function taken over an extended configuration space of $P$ copies (replicas) of the classical system, which are coupled by harmonic springs with frequencies $\omega_P \equiv \sqrt{P}/\hbar\beta$. The cyclic boundary conditions remain due to the initial need to evaluate a trace to obtain the partition function. The configurations in this extended space are commonly known as *ring polymers* (Figure 2.2). Importantly, note that within a ring polymer, the extended configuration space as defined above allows physical interactions through the PES only between atoms with the same replica index; interactions between different replicas are rather trivial since they only connect the neighboring ones through the harmonic spring terms.

The exact quantum system is represented by taking the limit of infinite $P$. In this limit, the ring polymers take on the form of continuous cyclic trajectories $\mathbf{R}(\tau)$ with $\tau$ going from 0 to $\hbar\beta$. Recognizing that the harmonic coupling term becomes an exact representation of the square of the first derivative of position with respect to imaginary time, we can identify this term with kinetic energy and, consequently, the whole potential with a Euclidean imaginary-time action of the discretized ring polymer trajectory

$$\begin{aligned} S_\mathrm{E}[\mathbf{R}(\tau)] &= \hbar\beta \lim_{P\to\infty} U_P(\mathbf{R}_1,\ldots,\mathbf{R}_P) \\ &= \int_0^{\hbar\beta} \mathrm{d}\tau \; \left\{ \sum_{I=1}^{N} \frac{1}{2} \left[ \frac{\mathrm{d}\mathbf{R}_I(\tau)}{\mathrm{d}\tau} \right]^2 + E_0[\mathbf{R}(\tau)] \right\}; \end{aligned} \tag{2.75}$$

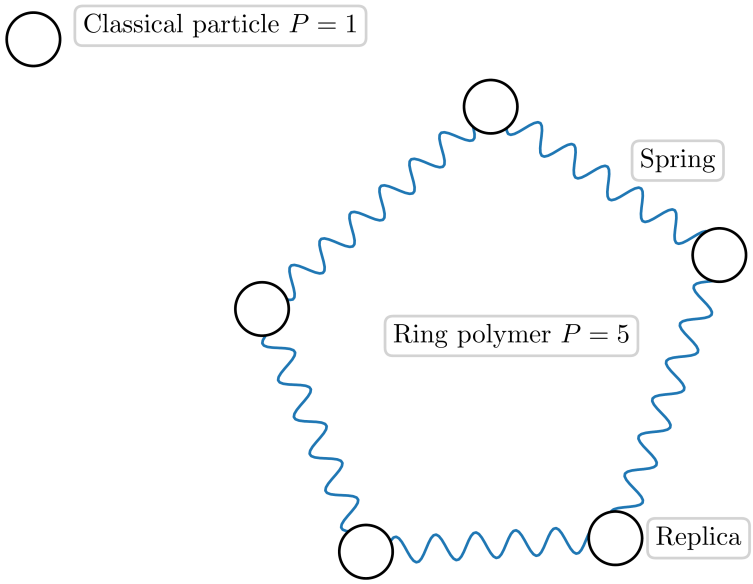


Figure 2.2: Comparison of a classical particle with $P = 1$ and a ring polymer with $P = 5$.

note the positive sign between the kinetic and potential energy term which is a result of the Wick rotation into the imaginary time domain. With this in mind, we can express the quantum partition function as a functional integral over all such cyclic trajectories

$$Q(\beta) \propto \oint \mathcal{D}[\mathbf{R}(\tau)] e^{-\frac{1}{\hbar} S_E[\mathbf{R}(\tau)]}. \tag{2.76}$$

It is clear through this expression that the path integral formalism offers a deeply insightful connection with classical physics by reintroducing the concept of a trajectory and by identifying quantum effects as weighted fluctuations around the classical trajectory with minimal action.

So far, we have shown that the imaginary time path integral framework can be used to calculate the partition function of a quantum system. How about observables according to Equation 2.68? It is not hard to see that we can only repeat the above procedure for the term $\mathrm{Tr}\,\widehat{\rho}\widehat{A}$ if $\widehat{A}$ represents an observable that only depends on positions $\widehat{A} = A(\widehat{\mathbf{R}})$, as this can be taken out of the position-represented trace. For such observables, we get the straightforward result

$$\langle A \rangle = \frac{1}{Q(\beta)} \lim_{P\to\infty} \prod_{I=1}^{N} \left( \frac{M_I P}{2\pi\beta\hbar^2} \right)^{\frac{3P}{2}} \int \mathrm{d}\mathbf{R}_1 \ldots \mathrm{d}\mathbf{R}_P \left[ \frac{1}{P} \sum_{i=1}^{P} A(\mathbf{R}_i) \right] e^{-\beta U_P(\mathbf{R}_1,\ldots,\mathbf{R}_P)}, \tag{2.77}$$

which tells us that the expectation value of $\widehat{A}$ can be obtained by averaging the expression inside the square brackets (known as the *estimator* of $\widehat{A}$) over the

extended phase space. A particularly important estimator is that of the ring-polymer *centroid*

$$\mathbf{R}_\mathrm{c} \equiv \frac{1}{P}\sum_{i=1}^{P}\mathbf{R}_i. \tag{2.78}$$

For other observables that depend on momenta as well, we cannot easily take the operator out of the trace like it was possible with position-only dependent operators. Consequently, their expectation values cannot be evaluated based on the knowledge of the diagonal matrix elements of the density matrix, and open paths are needed in addition to the cyclic paths. An exception is thermodynamic observables that can be expressed knowing $Q(\beta)$, since the partition function itself is defined through cyclic paths only. This includes important quantities such as pressure or total energy; estimators for the kinetic energy (a momentum-only dependent quantity) can also be derived based on the difference between total and potential energies. Various formulations of kinetic energy estimators are available and are often used as a convergence indicator for the number of replicas.[31]

#### 2.3.1.2 Classical limit

Arguably, one of the most remarkable achievements of the path integral formulation of quantum mechanics is its ability to naturally address the quantum–classical correspondence in contrast to the traditional operator mechanics, where the appropriate classical limits are often not easily found. For example, systems are known to behave more classically at high temperatures, but the behavior of the canonical density matrix as $\beta \to 0$ is not particularly illuminating in that sense. On the other hand, as $\beta \to 0$, the springs of the ring polymer stiffen as $\omega_P \to \infty$ and the whole ring polymer collapses onto a single classical point, consistently with the expected behavior. Therefore, restricting the path integral description to $P = 1$ at conditions where the classical limit is not yet reached amounts to making the classical approximation for the nuclei. $Q(\beta)$ reduces to the classical canonical partition function of distinguishable particles

$$Q_\mathrm{c}(\beta) = \prod_{I=1}^{N}\left(\frac{M_I}{2\pi\beta\hbar^2}\right)^{\frac{3}{2}}\int \mathrm{d}\mathbf{R}\; e^{-\beta E_0(\mathbf{R})} = \frac{1}{h^{3N}}\int\int \mathrm{d}\mathbf{R}\mathrm{d}\mathbf{P}\; e^{-\beta H(\mathbf{R},\mathbf{P})} \tag{2.79}$$

and the expectation value to the classical phase space Boltzmann average

$$\langle A\rangle_\mathrm{c} = \frac{\int\int \mathrm{d}\mathbf{R}\mathrm{d}\mathbf{P}\; A(\mathbf{R},\mathbf{P})e^{-\beta H(\mathbf{R},\mathbf{P})}}{\int\int \mathrm{d}\mathbf{R}\mathrm{d}\mathbf{P}\; e^{-\beta H(\mathbf{R},\mathbf{P})}}. \tag{2.80}$$

The deviations of the behavior of the fully quantum system from the classically approximated one are referred to as NQEs.

### 2.3.2 Molecular dynamics

At this point, we are equipped with the formal statistical tools to calculate the quantum and classical properties of a system of interacting nuclei on a given PES.

However, the corresponding formulae contain integrals that are not analytically solvable in most practically relevant settings. Therefore, they must be solved approximately by sampling the underlying configuration spaces and converging statistics on the representative subset of configurations. One approach used for this purpose is known as simulation of molecular dynamics (MD), which is based on sampling the configuration space by a numerical simulation of the time evolution of the system under appropriate equations of motion. In the section below, we will lead off with the discussion of classical MD and introduce the machinery used to enforce canonical sampling. Then, we will reintroduce NQEs through the above imaginary-time path-integral formalism to obtain path integral molecular dynamics (PIMD) and briefly discuss the most important practical aspects of simulation execution and our software choices for this work.

#### 2.3.2.1 Classical molecular dynamics

A classical MD simulation models the evolution of nuclei in time under the classical approximation. The exact dynamics of the classical system is encoded in the Hamilton equations

$$\nabla_{\mathbf{R}} H(\mathbf{R},\mathbf{P}) = \frac{\mathrm{d}\mathbf{P}}{\mathrm{d}t} \qquad \nabla_{\mathbf{P}} H(\mathbf{R},\mathbf{P}) = -\frac{\mathrm{d}\mathbf{R}}{\mathrm{d}t} \tag{2.81}$$

the formal solution of which is

$$\begin{bmatrix}\mathbf{R}(t)\\ \mathbf{P}(t)\end{bmatrix} = e^{iL(t-t_0)} \begin{bmatrix}\mathbf{R}(t_0)\\ \mathbf{P}(t_0)\end{bmatrix}, \tag{2.82}$$

where $iL$ is the so-called Liouville operator[31]

$$iL \equiv \nabla_{\mathbf{P}} H(\mathbf{R},\mathbf{P}) \cdot \nabla_{\mathbf{R}} - \nabla_{\mathbf{R}} H(\mathbf{R},\mathbf{P}) \cdot \nabla_{\mathbf{P}}. \tag{2.83}$$

The two parts of the operator do not commute, and the symmetric Trotter factorization can be used to develop a useful numerical approximation (exactly as was done above for the derivation of the quantum partition function in the path-integral context). Specifically, if we call the two terms in Equation 2.83 $iL_{\mathrm{A}}$ and $iL_{\mathrm{B}}$, by applying the factorization, disregarding the $P \to \infty$ limit, and introducing a time step $\Delta t = (t - t_0)/P$, we find that the approximate evolution of the system is obtained by successively applying the following propagator

$$e^{iL\Delta t} = e^{\frac{iL_B \Delta t}{2}} e^{iL_{\mathrm{A}}\Delta t} e^{\frac{iL_{\mathrm{B}}\Delta t}{2}}. \tag{2.84}$$

Explicitly filling in that

1. $\nabla_{\mathbf{R}} H(\mathbf{R},\mathbf{P}) = -\nabla_{\mathbf{R}} E_0(\mathbf{R}) = \mathbf{F}(\mathbf{R})$ is the vector of forces for the given configuration

2. $\nabla_{\mathbf{P}} H(\mathbf{R},\mathbf{P}) = \mathbb{M}^{-1}\mathbf{P} = \mathbf{V}$ is the vector of velocities (where $\mathbb{M}$ is the diagonal mass matrix $\mathrm{diag}(M_1,\ldots,M_{3N})$)

leads to the so-called velocity-Verlet propagator[144]

$$\begin{aligned}\mathbf{R}(t_0+\Delta t) &= \mathbf{R}(t_0) + \mathbf{V}\Delta t + \mathbb{M}^{-1}\frac{\mathbf{F}(\mathbf{R}(t_0))}{2}(\Delta t)^2 \\ \mathbf{V}(t_0+\Delta t) &= \mathbf{V}(t_0) + \mathbb{M}^{-1}\frac{[\mathbf{F}(\mathbf{R}(t_0)) + \mathbf{F}(\mathbf{R}(t_0+\Delta t))]}{2}\Delta t,\end{aligned} \tag{2.85}$$

which ensures a symplectic, finite-time-step integration of the Hamilton equations. Since the Hamilton equations conserve the Hamiltonian and hence the total energy by definition, using the velocity-Verlet propagator generates dynamics in the microcanonical ensemble (also at times denoted as *NVE* for its constant number of particles, volume, and energy).

#### 2.3.2.2 Origins of potential energy surfaces

It follows naturally from the Born–Oppenheimer framework that the PES $E_0(\mathbf{R})$ comes from an electronic structure calculation. In a typical setting, we do not have access to the full surface as a function of the nuclear configuration. Rather, we can calculate single-point energies and forces for a given configuration in line with Equation 2.8. An MD simulation where one does so explicitly on the fly in every simulation step is known as AIMD,[97] which is the simulation method of choice in this work. The non-negotiable benefit of an accurate electronic structure is counter-weighted by the computational expense brought about by the need for repeated energy and force evaluations. However, performing AIMD is not the only option. In simulations of larger systems where the *ab initio* PES is prohibitively expensive for running MD, one uses an empirical, physically motivated function of $\mathbf{R}$ known as a force field[27,145] to represent the PES. Empirical force fields usually do not reach the accuracy of *ab initio* surfaces. A modern method that favorably combines the accuracy of *ab initio* methods with the computational costs close to a force field is represented by a family of potentials known as machine learning potentials (MLPs),[35] discussed in detail in Section 2.4.

#### 2.3.2.3 Canonical sampling

While microcanonical statistics and dynamics are of interest for certain special systems — for instance, molecular clusters isolated in the interstellar void, one would often be interested in simulations in other ensembles that allow for a more physical, real-world experimental correspondence. In the context of this work, we focus on the canonical ensemble, *NVT*, which allows for fluctuations of energy in exchange for a requirement of a constant thermodynamic temperature

$$T \equiv \left\langle \frac{2E_{\text{kin}}}{3Nk_{\text{B}}} \right\rangle. \tag{2.86}$$

The canonical conditions are formally imposed by embedding the studied system in a heat bath at temperature $T$ with which it can exchange energy and which fixes the average temperature at the desired value. How does one represent the contact with the heat bath in the equations of motion without having to include a

vast number of explicit additional degrees of freedom? The bath effect is modelled by a new term[31,146] in the Liouville operator

$$iL = iL_{\mathrm{A}} + iL_{\mathrm{B}} + iL_{\mathrm{O}}, \tag{2.87}$$

which is commonly referred to as a thermostat: an abstract device that is used for temperature control. This gives, as one possibility, the following finite time-step propagator

$$e^{iL\Delta t} = e^{\frac{iL_{\mathrm{O}}\Delta t}{2}} e^{\frac{iL_{\mathrm{B}}\Delta t}{2}} e^{iL_{\mathrm{A}}\Delta t} e^{\frac{iL_{\mathrm{B}}\Delta t}{2}} e^{\frac{iL_{\mathrm{O}}\Delta t}{2}}. \tag{2.88}$$

Other options for the splitting exist and are equally valid, but they can lead to differences in performance and accuracy for specific thermostat choices. The explicit form of the O-term[h] is a matter of choice and numerous thermostat flavors are available. For instance, the Nosé thermostat[148] and its more practical reformulation in the form of Nosé–Hoover chains[149,150] extend the physical system with auxiliary degrees of freedom defined in such a way that a sampling of the microcanonical distribution in the extended phase space exactly generates a canonical one in the physical system. Alternatively, the Andersen thermostat[151] relies on a stochastic resampling of velocities from the Maxwell–Boltzmann distribution which also ensures a canonical distribution, although at the cost of a significant disruption of the dynamics of the system. As a primary thermostat choice in the simulations discussed in this work, a similar strategy of building on random processes is employed in the family of thermostats based on Langevin dynamics[152]

$$\frac{\mathrm{d}\mathbf{R}}{\mathrm{d}t} = \mathbf{V} \qquad \frac{\mathrm{d}\mathbf{P}}{\mathrm{d}t} = -\nabla_{\mathbf{R}} E_0(\mathbf{R}) - \gamma\mathbf{P} + \sqrt{\frac{2\gamma}{\beta}}\mathbb{M}^{\frac{1}{2}}\boldsymbol{\zeta}(t), \tag{2.89}$$

which approach the canonical distribution by adding a deterministic friction term ($\gamma\mathbf{P}$) and a stochastic term (represented by a vector of independent white noise variables $\boldsymbol{\zeta}$) to the purely Hamiltonian forces.[31] The two terms in the above Equation are balanced in a way that ensures a constant temperature through the so-called fluctuation–dissipation theorem.[31] The damping coefficient $\gamma$, given in units of inverse time, controls the time scale on which the thermostat converges the distribution of momenta to the canonical one. Using the Liouville operator formalism, one can find that the momentum update due to the thermostat is composed of two parts: a scaling and an addition of a random noise[147]

$$P_i(t+\Delta t) = P_i(t)e^{-\gamma\Delta t} + \zeta_i(t)\sqrt{\frac{M_i}{\beta}\left(1 - e^{-2\gamma\Delta t}\right)}. \tag{2.90}$$

The Langevin thermostat is an example of a *local* thermostat: the thermostat is coupled to and acts on the momentum of each degree of freedom individually. The local action of the thermostat leads to a robust convergence to the canonical distribution on the timescale $\sim \gamma^{-1}$. Still, it more easily disturbs the dynamics of

[h] The origin of the label O for the thermostat term is connected to the introduction of the Liouville operator formalism into the Langevin thermostat formulation where the stochastic part of the momentum update can be identified with an Ornstein–Uhlenbeck random process.[147]

the system enough so that no meaningful dynamic information can be extracted from the thermostatted trajectory. As such, this formulation is appropriate for equilibration simulations starting from even far-from-equilibrium initial conditions where an aggressive thermalization is needed. For simulations targeting canonical dynamic properties, one can use the stochastic velocity rescaling (SVR) (or canonical sampling through velocity rescaling (CSVR)) thermostat,[153] which can be shown to be the *global* version of the Langevin thermostat.[154] In this case, the momentum update is a simple collective rescaling

$$\mathbf{P}(t+\Delta t) = \alpha(\Delta t)\mathbf{P}(t), \tag{2.91}$$

where the rescaling factor $\alpha$ is determined stochastically, ensuring correct canonical sampling.[154] The global thermostat thus offers a smoother action on the momentum variables and is appropriate for production simulations intending the freedom to address dynamic properties on timescales shorter than $\gamma^{-1}$.

#### 2.3.2.4 Path integral molecular dynamics

The classical isomorphism offered by the imaginary time path integral representation of quantum mechanics can be exploited to simulate static NQEs in a formally exact way using the framework of classical MD in a method known as path integral molecular dynamics (PIMD).[18,31] Unlike in classical MD simulations, which in principle give access to both static and dynamic properties, PIMD simulations should not be attributed any relevance regarding real-time dynamics since the access to such properties was forfeited for staying in the computationally tractable imaginary time domain. However, approximate real-time dynamics can be obtained from PIMD simulations with some specifically tuned parameters: some relevant options are discussed in Section 2.3.3. Here, we discuss PIMD purely as a method of sampling "quantum geometries" needed to calculate the corresponding static expectation values of observables according to Equation 2.77.

To obtain a dynamical scheme to propagate the ring polymers, one needs to take a step back and reintroduce the momenta that were integrated out on the way to Equation 2.73. Technically, this is performed through a "reverse" Gaussian integration

$$\left(\frac{M_I P}{2\pi\beta\hbar^2}\right)^{\frac{3}{2}} = \int \mathrm{d}\mathbf{P}_I^{(i)}\; e^{-\beta\frac{4\pi^2\hbar^2\left(\mathbf{P}_I^{(i)}\right)^2}{2M_I P}} \equiv \int \mathrm{d}\mathbf{P}_I^{(i)}\; e^{-\beta\frac{\left(\mathbf{P}_I^{(i)}\right)^2}{2\mu_I}}, \tag{2.92}$$

which, when inserted back into the definition of $Q(\beta)$ gives the following PIMD Hamiltonian

$$\begin{aligned} &H_P(\mathbf{R}^{(1)},\ldots,\mathbf{R}^{(P)},\mathbf{P}^{(1)},\ldots,\mathbf{P}^{(P)}) = \\ &\sum_{i=1}^{P}\left\{\sum_{I=1}^{N}\left[\frac{\left(\mathbf{P}_I^{(i)}\right)^2}{2\mu_I} + \frac{1}{2}M_I\omega_P^2\left|\mathbf{R}_I^{(i+1)} - \mathbf{R}_I^{(i)}\right|^2\right] + \frac{1}{P}E_0(\mathbf{R}^{(i)})\right\}. \end{aligned} \tag{2.93}$$

In the above, we have rigorously reintroduced the physical masses of all degrees of freedom through the parameters $\mu_I$. However, since the mass-containing

prefactors fully cancel in the definition of $\langle A \rangle$ (Equation 2.77) and such observables, therefore, do not depend on mass at all, one is free to choose the set of $\mu_I$ arbitrarily to influence the integration time step and the rate of sampling.

However, naively using the Cartesian PIMD Hamiltonian to drive MD simulations is not practical due to the wide range of characteristic frequencies present in the ring polymers, which complicates thermalization and limits the simulation time step that one can afford without significantly affecting the accuracy of the integration.[155] To address this issue, practical simulations are typically performed in an alternative coordinate system based on the normal modes of the free ring polymer.[31] These are obtained as

$$\Omega_{I,\alpha}^{(k)} = \frac{1}{\sqrt{P}} \sum_{i=1}^{P} T_{ik} R_{I,\alpha}^{(i)}, \quad I = 1, \ldots, N; \ \alpha = x, y, z \tag{2.94}$$

using a transformation matrix $\mathbb{T}$ (with dimension $P \times P$) defined so that it diagonalizes the harmonic part of the PIMD Hamiltonian for each $\alpha$-th Cartesian component of $I$-th atom separately.[31] The transformed Hamiltonian then reads

$$\begin{aligned} &H_P(\Omega_{1,x}^{(1)}, \ldots, \Omega_{N,z}^{(P)}, \Pi_{1,x}^{(1)}, \ldots, \Pi_{N,z}^{(P)}) = \\ &\sum_{k=1}^{P} \left\{ \sum_{I=1}^{N} \sum_{\alpha=x,y,z} \left[ \frac{\left(\Pi_{I,\alpha}^{(k)}\right)^2}{2\mu_I^{(i)}} + \frac{1}{2} \mathcal{M}_I^{(i)} \omega_P^2 \left(\Omega_{I,\alpha}^{(i)}\right)^2 \right] \right. \\ &\left. + \frac{1}{P} E_0 \left[ \mathbf{R}^{(i)} \left( \Omega_{1,x}^{(1)}, \ldots, \Omega_{N,z}^{(P)} \right) \right] \right\}, \end{aligned} \tag{2.95}$$

where $\{\Pi_{I,\alpha}^{(k)}\}_{k=1}^{P}$ are conjugate momenta to the set of normal modes $\{\Omega_{I,\alpha}^{(k)}\}_{k=1}^{P}$. The auxiliary mode masses $\mu_I^{(i)}$ can be again chosen arbitrarily ($\mathcal{M}_I^{(i)}$ is fixed at the value of the physical mass $M_I^{(i)}$ times the square of the mode frequency[31]). The decoupled picture thus allows us to set the mode masses individually in a way that shifts their frequencies with a positive impact on the accessible length of the integration time step. The propagation proceeds fully in normal mode coordinates except for when the PES needs to be evaluated, which is only possible in the original Cartesian coordinates: each step, a backward transformation of positions and a forward transformation of forces is, therefore, necessary. Efficient implementations based on fast Fourier transform (FFT) are available.[156]

PIMD simulations require careful thermostatting to impose canonical conditions. The original approach uses Nosé–Hoover chains locally for each normal mode.[146] More commonly these days, this is achieved by attaching a Langevin thermostat to each degree of freedom in an approach known as local path-integral Langevin equation (PILE-L),[157] which offers superior computational efficiency at comparable accuracy. A global Langevin tharmostatting scheme known as global path-integral Langevin equation (PILE-G)[157] is obtained by attaching a single global SVR thermostat to the centroids of all the ring polymers while keeping local thermostats attached to the higher modes.

#### 2.3.2.5 Practical remarks

As discussed above in the context of the electronic part of the problem, MD simulations often need to be performed under PBCs to represent the condensed phase. For the nuclei, this pertains to how interatomic distances are calculated. Specifically, PBCs respect the so-called minimum image convention, where the physically relevant distance between two atoms $I$ and $J$ is always taken to be the one between the closest periodic images. For a general box described by three lattice vectors $(\mathbf{a}_1, \mathbf{a}_2, \mathbf{a}_3)$, the minimum image convention is achieved by modifying a displacement vector between atoms $I$ and $J$ as

$$\mathbf{R}_{IJ} \leftarrow \mathbf{R}_{IJ} - \sum_{i=1}^{3} \left\rceil \frac{\mathbf{R}_{IJ} \cdot \mathbf{a}_i}{|\mathbf{a}_i|^2} \right\rceil \mathbf{a}_i, \tag{2.96}$$

where $\lfloor\ \rceil$ denotes the rounding operation. For cubic simulation boxes, which are important in the context of simulations of liquid systems and which are fully specified by a box length $L$, the above equation reduces to

$$\mathbf{R}_{IJ} \leftarrow \mathbf{R}_{IJ} - L \left\rceil \frac{\mathbf{R}_{IJ}}{L} \right\rceil. \tag{2.97}$$

For visualization purposes, the raw atomic positions are commonly wrapped into the original unit cell using

$$\mathbf{R}_I \leftarrow \mathbf{R}_I - L \left\lfloor \frac{\mathbf{R}_I}{L} \right\rfloor, \tag{2.98}$$

where $\lfloor\ \rfloor$ denotes the floor operation. Explicit wrapping of atoms is, however, not strictly needed for successful simulation execution.

Finally, we sketch out how initial conditions for running MD simulations are obtained. Clearly, this has to be physical in the sense that the chosen configuration and its attached momenta must lie, loosely speaking, in a reasonably thermally accessible region of the phase space to minimize equilibration time and prevent both SCF and numerical propagator failures. For isolated molecules in the gas phase and ordered crystalline solids, a reasonable starting point is a structure optimized to a local minimum using a PES on par with the one intended to be used to drive the simulation. Disordered systems such as neat liquids and solutions are usually constructed by randomly placing a given number of solvent molecules into the simulation box and running an equilibration simulation using either a force field or a computationally inexpensive *ab initio* PES to accommodate the non-covalent interaction between the molecules. The corresponding momenta are typically sampled from the Maxwell–Boltzmann distribution at the target simulation temperature. Once an acceptable initial condition is obtained, a several ps-long equilibration simulation is performed with the production-level PES to properly thermalize all degrees of freedom. This trajectory is not intended for statistical analysis and can be discarded; its last point is used as a properly equilibrated initial condition for production simulations.

#### 2.3.2.6 Software choices

Besides being a highly optimized electronic structure package, CP2K can also be used as an AIMD engine: all classical DFT- and MLP-based simulations in this work have been performed using this software. PIMD simulations have been accomplished using the i-PI program.[158] Written in the Python programming language, it is intended primarily as a simulation engine that relies on externally provided forces. Notably, it does not independently perform electronic structure calculations but relies on a socket interface to couple to various established electronic structure packages, including CP2K and FHI-aims, that calculate forces on individual imaginary time slices. Simpler manipulation with atomic nuclei, *e.g.*, geometry optimizations, and nudged elastic band (NEB) calculations,[159] has been accomplished using the Atomic Simulation Environment (ASE).[160]

### 2.3.3 Dynamical properties

So far, we have built the infrastructure to study static properties. However, equilibrium dynamical properties such as diffusion constants, rates of chemical reactions, and vibrational spectra are equally relevant to providing insight into the behavior of molecular systems, and it is, therefore, the key to being able to model those as well. The usual approach relies on linear response theory, which relates dynamical properties to the so-called time correlation functions (TCFs) and, therefore, sets up the task of calculating such functions from equilibrium MD simulations.

#### 2.3.3.1 Time correlation functions

The standard way to define a quantum-mechanical thermal equilibrium TCF between observables $\widehat{A}$ and $\widehat{B}$ is[31]

$$c_{AB}(\tau) \equiv \langle \widehat{A}(t_0)\widehat{B}(t_0+\tau)\rangle = \frac{1}{Q(\beta)} \operatorname{Tr} e^{-\beta\widehat{H}} \widehat{A}\widehat{U}^{\dagger}(\tau)\widehat{B}\widehat{U}(\tau) \tag{2.99}$$

where $\widehat{U}^{\dagger}(\tau)\widehat{B}\widehat{U}(\tau)$ is the Heisenberg-evolved operator $\widehat{B}$ to a delay time $\tau$ with respect to an initial condition taken to be at $t_0$. Alternatively, one can define the Kubo-transformed version of the TCF[161]

$$\bar{c}_{AB}(\tau) = \frac{1}{\beta Q(\beta)} \int_0^{\beta} \mathrm{d}\lambda \ \operatorname{Tr} e^{-(\beta-\lambda)\widehat{H}} \widehat{A} e^{-\lambda\widehat{H}} \widehat{U}^{\dagger}(\tau)\widehat{B}\widehat{U}(\tau), \tag{2.100}$$

which is not exactly the same as $c_{AB}(\tau)$, but the two (and also other formulations of quantum TCFs) can be shown to be rigorously related in the Fourier domain through[31]

$$\widehat{c}_{AB}(\omega) = \left(\frac{\hbar\beta\omega}{1-e^{-\hbar\beta\omega}}\right) \widehat{\bar{c}}_{AB}(\omega). \tag{2.101}$$

In contrast, under the classical approximation, the TCF is defined unambiguously as

$$c_{AB}(\tau) = \frac{1}{Q_{\mathrm{c}}(\beta)} \int\int \mathrm{d}\mathbf{R}\mathrm{d}\mathbf{P} \ A[\mathbf{R}(t_0),\mathbf{P}(t_0)]B[\mathbf{R}(t_0+\tau),\mathbf{P}(t_0+\tau)]e^{-\beta H(\mathbf{R}(t_0),\mathbf{P}(t_0))}, \tag{2.102}$$

correlating the phase space functions separated by the delay $\tau$.

Calculating classical TCFs is, therefore, quite straightforward as classical MD simulations capture physically meaningful dynamics. Correctly, the calculation of the canonical TCF is approached by sampling several initial conditions from a thermostatted MD trajectory and running a set of $NVE$ trajectories from each, collecting time correlations along them. In practice, this rigorous approach is usually replaced by an approximate treatment in which time correlations are collected along a single, long, weakly enough thermostatted $NVT$ trajectory.[31] Simulating quantum TCFs represents a fundamentally more serious problem since PIMD simulations based on imaginary time path integrals do not contain physically meaningful dynamics. Despite this limitation, it was proposed that given a reasonable choice of replica masses, the auxiliary PIMD dynamics can, in fact, be used, at least in an approximate way, to capture real-time dynamics. Two main types of PIMD simulation that build on this premise are known as centroid molecular dynamics (CMD)[162] and ring polymer molecular dynamics (RPMD).[163,164] In an RPMD simulation, one assigns physical particle masses to each replica ($\mu_I = M_I$) and runs the time evolution in the $NVE$ ensemble. RPMD thermal correlation functions are thus calculated by sampling initial conditions from a canonical, thermostatted PIMD simulation and running multiple daughter RPMD trajectories from them. The obtained microcanonical dynamics of the replicas is used to approximate the Kubo-transformed TCF through the following prescription

$$\begin{aligned} \bar{c}_{AB}(\tau) &\approx \frac{1}{(2\pi\hbar)^P Q(\beta)} \int\int \mathrm{d}^P\mathbf{R}\mathrm{d}^P\mathbf{P}\ A_P(t_0)B_P(t_0+\tau)e^{-\beta H_P} \\ &= \langle A_P(t_0)B_P(t_0+\tau)\rangle, \end{aligned} \tag{2.103}$$

where the estimate of the quantum time-dependent observable is

$$A_P(t) = \frac{1}{P}\sum_{i=1}^{P} A[\mathbf{R}_i(t)]. \tag{2.104}$$

Note that for linear operators, this is equivalent to the observable being evaluated at the position of the ring polymer centroid, but for non-linear operators, it first needs to be evaluated for each replica separately and then averaged. The RPMD prescription of the exact Kubo TCF can be shown to have the properties of being exact in the harmonic limit and being a reliable approximation in the limit of short delays.[163] Historically, this gave it enough credibility to be routinely used in approximate simulations of quantum dynamics despite the *ad hoc* nature of its formulation. Later on, the specific RPMD formulae were given a more rigorous footing by connecting it to real-time quantum dynamics by performing approximations in the Matsubara dynamics formalism.[165] Generally speaking, RPMD is a very successful and efficient approach to approximating quantum dynamics. However, its downside is that it exhibits spurious artifacts in simulated vibrational spectra due to the resonance between internal ring modes and physical molecular vibrations.[166] This issue is solved by thermostatted RPMD (TRPMD), where thermostats are carefully attached to the internal ring polymer modes to dampen these spurious resonances.[167] This requires the same kind of treatment

as RPMD to obtain thermal correlation functions. In practice, one normally attaches a weak thermostat also on the centroid and approaches the calculation of correlation from a single, long $NVT$ trajectory as discussed above for classical TCFs.

Finally, a couple of notes on the properties of TCFs. Note that in the following, we will only use the classical, operator-less notation for TCFs for both the quantum and the classical case since the quantum TCFs can now be calculated in a classical fashion over an extended phase space through RPMD. First, given a long enough trajectory, one can rely on the same principle that holds for static properties that a statistical average is equivalent to a time average. In the present case, replacing the statistical average with an average over the trajectory redefines the TCF as

$$c_{AB}(\tau) = \lim_{T\to\infty} \frac{1}{T} \int_{-T}^{T} \mathrm{d}t_0 \; A(t_0)B(t_0+\tau) \equiv A * B, \tag{2.105}$$

which is consistent with the mathematical understanding of correlation functions as convolutions of time series. Second, TCFs have specific symmetry properties pertaining to time reversal. We have

$$c_{AB}(-\tau) = \langle A(t_0)B(t_0-\tau)\rangle = \langle A(t_0'+\tau)B(t_0')\rangle = c_{BA}(\tau). \tag{2.106}$$

Therefore, general cross-correlation functions between observables $A$ and $B$ do not have any special properties regarding mirroring around the origin of the time axis, *e.g.*, evenness, but flipping the order of observables is equivalent to flipping the time axis. An autocorrelation function (ACF), *i.e.*, a TCF for a single observable, clearly is an even function of time since

$$c_{AA}(-\tau) = c_{AA}(\tau). \tag{2.107}$$

#### 2.3.3.2 Vibrational spectra

As briefly mentioned in the opening of this Section, vibrational spectroscopy is an experimental technique that measures the separations of nuclear energy levels using light–matter interaction to induce the relevant transitions. Our computational treatment of nuclei presented so far does not offer a state-resolved solution of nuclear degrees of freedom to calculate the vibrational transitions directly, but they can be accessed via a TCF-based approach. Specifically for IR absorption spectroscopy, the spectral intensity can be related to the Fourier transform of the time ACF of the time derivative of the total dipole moment $\mathbf{M}$ of a system[168]

$$\begin{aligned} I_{\mathrm{IR}}(\omega) \propto \mathcal{F}[c_{\dot{\mathbf{M}}\dot{\mathbf{M}}}(\tau)] &= \int \mathrm{d}\tau \; e^{-i\omega\tau} \left\langle \frac{\mathrm{d}\mathbf{M}}{\mathrm{d}t}(t_0) \cdot \frac{\mathrm{d}\mathbf{M}}{\mathrm{d}t}(t_0+\tau) \right\rangle \\ &= \omega^2 \int \mathrm{d}\tau \; e^{-i\omega\tau} \langle \mathbf{M}(t_0) \cdot \mathbf{M}(t_0+\tau)\rangle. \end{aligned} \tag{2.108}$$

where the second equality is based on the so-called $\omega^2$-theorem, which is a fundamental property of the Fourier transform and can be found derived in Appendix A. The reason why this holds can perhaps be gleaned from the fact that

the light–matter interaction that introduces vibrational transitions can be theoretically described as a perturbation to the total Hamiltonian that depends explicitly on $\mathbf{M}$, hence its fundamental role in IR spectra. In fact, the tools offered by time-dependent perturbation theory can be used to rigorously connect this perturbation to Equation 2.108 using Fermi's golden rule (with a bit of algebraic effort, as shown in Reference 31). Conveniently, theoretical simulation of IR spectra allows for various useful decompositions of the total spectrum $I(\omega)$ that are not experimentally accessible and can provide relevant insight. For instance, the total dipole moment can be decomposed into molecular contributions for the $N_{\text{mol}}$ molecular entities in the system

$$\mathbf{M} = \sum_{i=1}^{N_{\text{mol}}} \boldsymbol{\mu}_i, \tag{2.109}$$

given a specific partitioning scheme: our simulation setup in CP2K relies on maximally localized Wannier orbitals.[169] This illustrates that an IR spectrum is a highly non-trivial quantity since

$$\begin{aligned} \langle \mathbf{M}(t_0) \cdot \mathbf{M}(t_0+\tau) \rangle &= \sum_{ij} \langle \boldsymbol{\mu}_i(t_0) \cdot \boldsymbol{\mu}_j(t_0+\tau) \rangle \\ &= \sum_{i=1}^{N} \langle \boldsymbol{\mu}_i(t_0) \cdot \boldsymbol{\mu}_i(t_0+\tau) \rangle + \sum_{i,j\neq i} \langle \boldsymbol{\mu}_i(t_0) \cdot \boldsymbol{\mu}_j(t_0+\tau) \rangle, \end{aligned} \tag{2.110}$$

which tells us that the overall picture cannot be described only as a sum over individual molecular contributions (self-terms, first sum) but also cross-correlations (second sum) that describe how dipoles on individual molecules are affected by interacting with dipoles elsewhere in the system. Another highly useful spectrum decomposition is that in the time variable, which will be discussed in Chapter 5.

As a computationally simpler vibrational quantity, which, however, does not have an experimentally measurable equivalent, we use the vibrational density of states (VDOS)

$$I_{\text{VDOS}}(\omega) \propto \mathcal{F}[c_{\mathbf{vv}}(\tau)] = \int \mathrm{d}\tau \; e^{-i\omega\tau} \sum_{i=1}^{N} \langle \mathbf{v}_i(t_0) \cdot \mathbf{v}_i(t_0+\tau) \rangle, \tag{2.111}$$

which is defined through atomic velocity autocorrelation self-terms only. As such, it can be easily decomposed into any subsets of atoms in the studied system and, since it only corresponds to atomic motion, it is not obfuscated by electronic effects and selection rules like IR is. It is also possible to simulate other vibrational spectra through the TCF approach, for example, Raman scattering[170] or sum-frequency generation spectra,[171] but the corresponding theory will not be discussed as these quantities are not modeled in this work.

#### 2.3.3.3 Reaction rates

In Chapter 6, we will discuss the simulation of the rate constant of a proton transfer reaction. Reaction rates represent another type of dynamic quantity

that can be related to TCFs. Specifically, given a potential energy landscape consistent with a reactive transition, the rate is related to the long time limit of the so-called flux-side correlation function

$$\begin{aligned} k(\beta)Q_{\mathrm{r}}(\beta) &= \lim_{\tau\to\infty} c_{\mathrm{fs}}(\tau) \\ &= \lim_{\tau\to\infty} \left\langle \frac{\mathrm{d}\theta\{s[\mathbf{R}(t_0)]\}}{\mathrm{d}t}\theta\{s[\mathbf{R}(t_0+\tau]\}\right\rangle, \end{aligned} \tag{2.112}$$

where $s(\mathbf{R})$ is a reaction coordinate, $s(\mathbf{R}) = 0$ is a dividing surface that separates the reactants from the products, $\mathrm{d}\theta(s)/\mathrm{d}t$ is the flux through that surface, $\theta(s)$ is a step function representing a projector on the product side and $Q_{\mathrm{r}}(\beta)$ is the so-called reactant partition function.[172] RPMD rate theory,[173] *i.e.*, using RPMD simulations to sample $c_{\mathrm{fs}}(\tau)$, is a powerful approach to access thermal rate constants including dynamic recrossings and tunneling NQEs, especially employing the Bennett–Chandler factorization[174] to facilitate the statistical sampling.

In this work, we do not use full RPMD theory to simulate reaction rates but rather rely on a semiclassical approach known as ring polymer instanton rate theory.[96] While this can be rationalized by making a semiclassical approximation to the flux-side correlation function,[175] it is more commonly derived starting with the so-called $\mathrm{Im}\,F$ (imaginary free energy) premise.[96,176] Both versions of instanton theory are equivalent but lead to different practical formulae for the tunneling rates.[177] The $\mathrm{Im}\,F$ premise can be rationalized by modeling the reacting system as a decay of trapped resonances through the barrier[175] with such considerations leading to the expression for the thermal rate

$$k(\beta) \approx -\frac{2}{\hbar}\,\mathrm{Im}\,F(\beta), \tag{2.113}$$

where $F(\beta)$ is a complex-valued free energy corresponding to the metastable decaying system. Introducing a complex-valued partition function $R(\beta) = e^{-\beta F(\beta)}$ then allows us to write

$$k(\beta) \approx \frac{2}{\beta\hbar}\,\mathrm{Im}\,R(\beta) = \frac{2}{\beta\hbar}\arctan\frac{\mathrm{Im}\,R(\beta)}{\mathrm{Re}\,R(\beta)} \approx \frac{2}{\beta\hbar}\frac{\mathrm{Im}\,R(\beta)}{\mathrm{Re}\,R(\beta)}, \tag{2.114}$$

where the last approximation represents a linear approximation for the arctan function for the expected relation $\mathrm{Im}\,R(\beta) \ll \mathrm{Re}\,R(\beta)$. The real part of $R(\beta)$ can be shown to be connected to the reactant partition function $Q_{\mathrm{r}}(\beta)$. This implies, in a loose sense, that the imaginary part $\mathrm{Im}\,R(\beta)$ is correspondingly connected to the barrier region and will be further referred to as the imaginary part of the instanton partition function $\mathrm{Im}\,Q_{\mathrm{inst}}(\beta)$,[178,179] allowing us to re-express the thermal rate as

$$k(\beta)Q_{\mathrm{r}}(\beta) = \frac{2}{\beta\hbar}\,\mathrm{Im}\,Q_{\mathrm{inst}}(\beta). \tag{2.115}$$

The ring polymer instanton theory is obtained by applying the discrete Feynman path integral formalism in imaginary time to evaluate both partition functions using Equation 2.76 and further approximating the resulting integral using

the steepest descent approximation. Roughly speaking, this approach is equivalent to expanding the action functional into a second-order Taylor series around a local minimum, which is well justified because the exponential quickly quenches fluctuations at high values, leaving the local minima to dominate the value of the integral. This gives us

$$\begin{aligned} Q(\beta) &\propto \oint \mathcal{D}[\mathbf{R}(\tau)] e^{-\frac{1}{\hbar} S_{\mathrm{E}}[\mathbf{R}(\tau)]} \\ &\approx \lim_{P\to\infty} \sum_{\text{all minima}} \sqrt{\left[\frac{2\pi\hbar}{\det \mathbb{H}_{S_{\mathrm{E}}}(\mathbf{R}_{\min})}\right]^{P}} e^{-\frac{1}{\hbar} S_{\mathrm{E}}(\mathbf{R}_{\min})}, \end{aligned} \tag{2.116}$$

where $\mathbf{R}_{\min}$ is a ring-polymer configuration that minimizes $S_{\mathrm{E}}$ and $\mathbb{H}_{S_{\mathrm{E}}}$ is the Hessian matrix of the action. Therefore, the calculation of the partition function is reduced to an optimization of well-defined stationary imaginary time paths and to the calculation of the determinant of the matrix of second derivatives of the paths' action with respect to replica displacements. Naturally, practical calculations are performed using a finite $P$ approximation. Finding a stationary point of the action requires that

$$\boldsymbol{\nabla} S_{\mathrm{E}} = \mathbf{0}. \tag{2.117}$$

Explicit differentiation of the action gives

$$M_I \frac{R_{I,\alpha}^{(i+1)} - 2R_{I,\alpha}^{(i)} + R_{I,\alpha}^{(i-1)}}{(\Delta\tau)^2} = +\frac{\partial E_m}{\partial R_{I,\alpha}^{(i)}}, \quad \alpha = x, y, z \tag{2.118}$$

with $\Delta\tau = 1/\omega_P$. This traces a classical, Newtonian trajectory on an inverted PES. The reactant state corresponds to a minimum on the PES, and the only way for such a stationary imaginary-time path to be arranged to comply with the above conditions is with a ring polymer that is fully collapsed onto the PES minimum. Evaluating $Q_{\mathbf{r}}(\beta)$ in using the steepest descent method is thus trivial and leads to the harmonic approximation for the reactant partition function. The instanton then corresponds to a first-order saddle point on the extended ring-polymer PES. It can be shown[177] that at high temperatures, the geometry of the instanton also corresponds to all replicas being collapsed onto the classical transition state (TS), making the theory equivalent with classical transition state theory. However, such a configuration ceases to be a first-order stationary point at temperatures below the so-called crossover temperature[96]

$$T_{\mathrm{c}} = \frac{\hbar\omega_{\mathrm{barrier}}}{2\pi k_{\mathrm{B}}}, \tag{2.119}$$

with $\omega_{\mathrm{barrier}}$ being the absolute value of the imaginary frequency at the barrier, and a non-trivial instanton trajectory appears that falls down from the barrier and retraces itself once back and forth. Using the steepest descent method on such an imaginary-time trajectory is not as straightforward as for the reactant state as we are dealing with a saddle point. That means that we can employ

the approximation for all degrees of freedom given by normal modes with real frequencies, but the mode corresponding to the unstable direction must be treated specially by continuation into the complex plane. Moreover, the ring polymer has a mode with a zero-valued frequency that represents the cyclic permutation of the ring-polymer beads: this can also be integrated analytically.[96,179] Once these two modes are taken care of, the final expression for the instanton rate becomes

$$k(\beta) = A(\beta) e^{-\frac{1}{\hbar} S_{\mathrm{E}}(\mathbf{R}_{\mathrm{inst}})}; \tag{2.120}$$

note the resemblance with the classical Eyring equation. The preexponential factor $A(\beta)$ contains all the terms originating from the steepest-descent treatment of vibrational degrees of freedom as well as classical approxmations for the rotational and translational components of the partition functions: the complete rate formula can be found, for example, in Reference 179. Evaluating $A(\beta)$ requires the calculation of the second derivatives of the action with respect to all replica positions. This yields the following sparse matrix

$$\mathbb{H}_{S_{\mathrm{E}}} = \omega_P^2 \begin{pmatrix} \mathbb{H}^{(1)} + 2 \cdot \mathbb{I}_1 & -\mathbb{I}_1 & \mathbb{I}_0 & \cdots & -\mathbb{I}_1 \\ -\mathbb{I}_1 & \mathbb{H}^{(2)} + 2 \cdot \mathbb{I}_1 & -\mathbb{I}_1 & \cdots & \mathbb{I}_0 \\ \mathbb{I}_0 & -\mathbb{I}_1 & \mathbb{H}^{(3)} + 2 \cdot \mathbb{I}_1 & \cdots & \mathbb{I}_0 \\ \vdots & \vdots & \vdots & \ddots & \vdots \\ -\mathbb{I}_1 & \mathbb{I}_0 & \mathbb{I}_0 & \cdots & \mathbb{H}^{(P)} + 2 \cdot \mathbb{I}_1 \end{pmatrix}, \tag{2.121}$$

where $\mathbb{H}^{(i)}$ is the mass-weighted Hessian of the $i$-th replica, $\mathbb{I}_1$ is the identity matrix of size $3N$ and $\mathbb{I}_0$ is a zero-valued matrix of the same size. Calculating its determinant is what primarily makes the instanton method computationally demanding at low temperatures, where high replica numbers are needed. Instanton theory has been successfully deployed to calculate thermal rates of reactions in the gas phase and on surfaces.[178–180] Its applicability becomes limited once numerous reaction channels start contributing to the total rate, *e.g.*, in the condensed phase, as they need to be considered one by one.

## 2.4 | Neural network potentials

*Ab initio* calculations with quantum electronic structure are a powerful tool to conduct theoretical studies of molecular systems. However, the high computational demands connected to the *ab initio* calculations restrict the applicability of the method to relatively small systems: for example, the simulation of a periodic box containing 64 water molecules and a single benzene solute at a hybrid DFT level (*cf.* systems discussed in Chapter 5) can already be considered a large simulation project with timing of ∼95 s per MD step on a 32-core EPYC-based compute node. The role of neural network potentials (NNPs) is to replace the explicit quantum mechanical calculation and, therefore, to reduce the computational cost of the simulation while maintaining its accuracy.

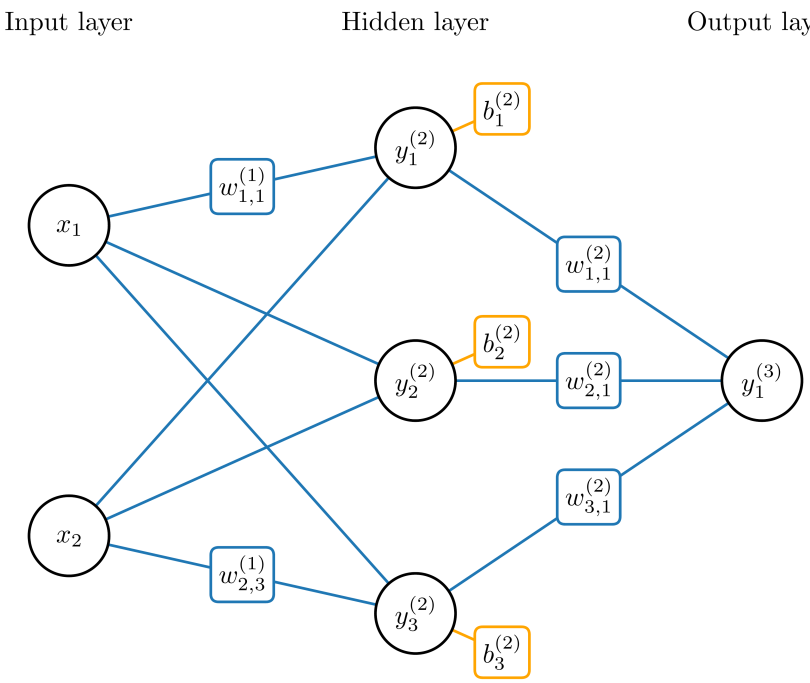


Figure 2.3: An example of a structure of a feedforward NN with a two-dimensional input, a single hidden layer, and a one-dimensional output. Neurons are represented by black circles, a selected set of weights in blue, and biases in orange.

### 2.4.1 The basic principle of a neural network

In general, an artificial NN is a mathematical structure inspired by biological neural networks, where neurons take multiple inputs and produce an output that is distributed to subsequent neurons to convey complex information. Feedforward NNs,[37] which are the kind of networks used for NNP applications in this work, have a layered structure consisting of an input layer, one or several hidden layers, and an output layer, each containing a given number of neurons connected by weights $w$ (Figure 2.3). In the following, we will consider one-dimensional outputs only. Information flows unidirectionally from the input layer to the output layer, creating a mapping $y = y(\mathbf{x})$ ($\equiv y^{(3)}_1$ in Figure 2.3) that establishes a unique relationship between the input vector $\mathbf{x}$ and the output $y$ through a specific choice of the NN parameters. In addition to weights, these parameters also include biases $b$, which act as an offset of the value predicted in the individual neurons. This prediction is represented by the following function for a neuron at position $i$ in layer $k > 1$

$$y_i^{(k)} = f^{(k)} \left( b_i^{(k)} + \sum_{j=1}^{N^{(k-1)}} y_j^{(k-1)} w_{ji}^{(k-1)} \right), \tag{2.122}$$

which connects the outputs of all neurons in the previous layer to the one in question through the corresponding weights and biases. The so-called activation function $f^{(k)}$ is a specifically selected non-linear function that gives the NN the flexibility to fit complex, non-linear relationships. Often, smooth switch functions

such as the logistic function or the hyperbolic tangent are used as activation functions for regression problems. Importantly, the so-called universal approximation theorem shows that infinitely large NNs are universal approximators that can fit any arbitrary function.

As an important application, feedforward NNs are employed in regression tasks in which, given a number of discrete samples of inputs and associated outputs representing the underlying relationship (*i.e.*, the training set), the NN is trained to yield the best possible fit through these data points. This is normally achieved by minimizing an appropriate loss function, for instance, the mean square error between the predicted output $y(\mathbf{x}_i)$ for a given input $\mathbf{x}_i$ and the corresponding target value $t_i$.

$$L(w, b; \{\mathbf{x}_i, t_i\}) = \frac{1}{N} \sum_{i=1}^{N} \left[ y(\mathbf{x}_i) - t_i \right]^2 , \tag{2.123}$$

with respect to the NN parameters. The optimization is normally performed by various gradient descent approaches such as first-order-only backpropagation,[181] more efficient second-order Levenberg–Marquardt[182] or L-BFGS[183–187] algorithms, or by alternative approaches, *e.g.*, Kalman filtering.[188] Given the inherent complexity of the loss function for many-dimensional data, it is nearly certain that a trained model is based on a set of parameters that correspond to a local rather than a global minimum. This is fully acceptable as long as the fit error is reasonable, *i.e.*, the minimum lies low enough to allow for reliable predictions.

To bypass explicit *ab initio* calculations, NNs are used as NNPs to model the *ab initio* PES as a function of the nuclear configuration

$$E_0(\mathbf{R}) = \langle \psi_0(\mathbf{R}) | \, \widehat{H}_\mathrm{e}(\mathbf{R}) \, | \psi_0(\mathbf{R}) \rangle \tag{2.124}$$

by training on a set of *ab initio* configurations and energies $\{\mathbf{R}_i, E_i\}$. However, training directly on Cartesian atomic positions would give rise to two detrimental problems. First, it does not yield models that would exhibit translational, rotational, and permutational symmetries (permutational in the sense of exchanging coordinates of atoms of the same kind) as required by the invariance of $\widehat{H}_\mathrm{e}(\mathbf{R})$ to such transformations. This is because transforming the input coordinates changes the input for a model that does not have these symmetries fundamentally wired into its structure. Second, such models would only work for a fixed system size and not generalize to other arrangements. Both issues are addressed by the Behler–Parrinello architecture.[36]

### 2.4.2 Behler–Parrinello high-dimensional NNPs

The main idea behind the Behler–Parrinello architecture (as well as several others) is to split the total electronic energy into atomic contributions to the total energy

$$E_0 = \sum_{i=1}^{N} E_i \tag{2.125}$$

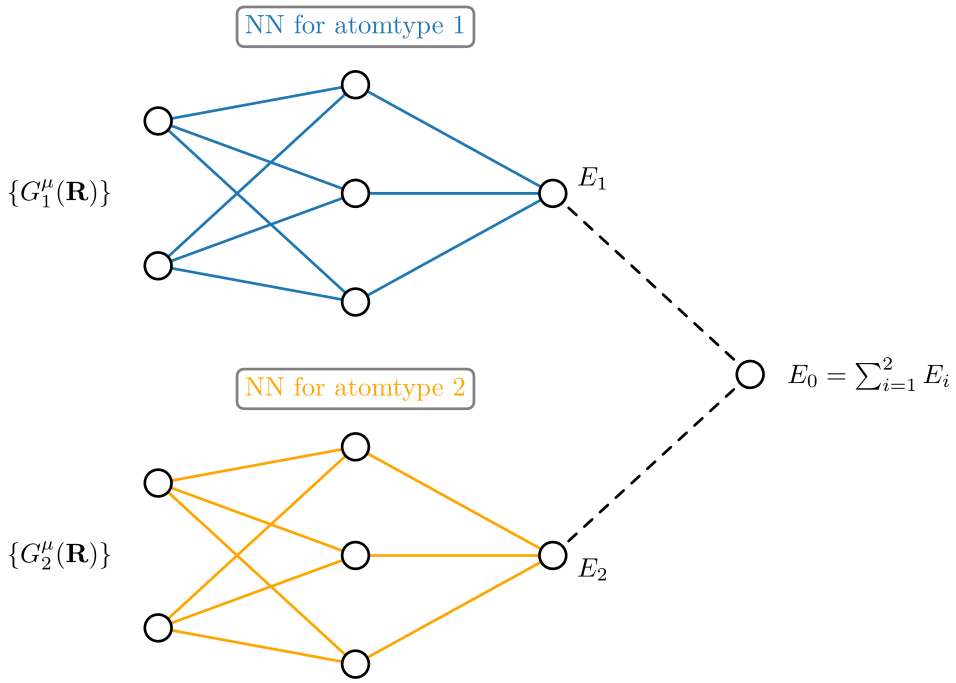


Figure 2.4: A schematic illustration of the Behler–Parrinello NNP architecture. The atom centered symmetry functions (ACSF) $G_i^\mu$ describe the geometry of the system and are derived directly from the Cartesian positions of the atoms. For each atom of a given kind, its set of descriptors is fed to the corresponding atomic subnetwork, yielding atomic energies $E_i$. These are finally summed to obtain the total electronic energy $E$.

and predict each $E_i$ through individual subnetworks for each atom type (Figure 2.4) using a set of geometric descriptors that comply with the required symmetry properties to describe the local chemical environments of each atom. It is important to realize that the atomic energies $E_i$ do not have any physical meaning and do not correspond to the electronic energies of isolated atoms. The atomic subnetworks are self-standing NNs on their own and are not coupled to the other ones in any other way than through Equation 2.125, which represents the connection between the last two layers of the overall NN with unit weights and no biases (Figure 2.4). In this way, all of the complications mentioned above are addressed since

1. Contributions to the total energy $E_i$ are additive and, therefore, the model is applicable to arbitrary system sizes.

2. The exact same atomic subnetwork is used for all atoms of the same kind, which ensures permutational symmetry.

3. The specific form of the atomic environment descriptors ensures rotational and translational symmetry.

There is no unique set of descriptors to achieve the last point, and a convenient choice must therefore be made. In their original paper, Behler and Parrinello employ the so-called atom centered symmetry functions (ACSF).[36] These functions

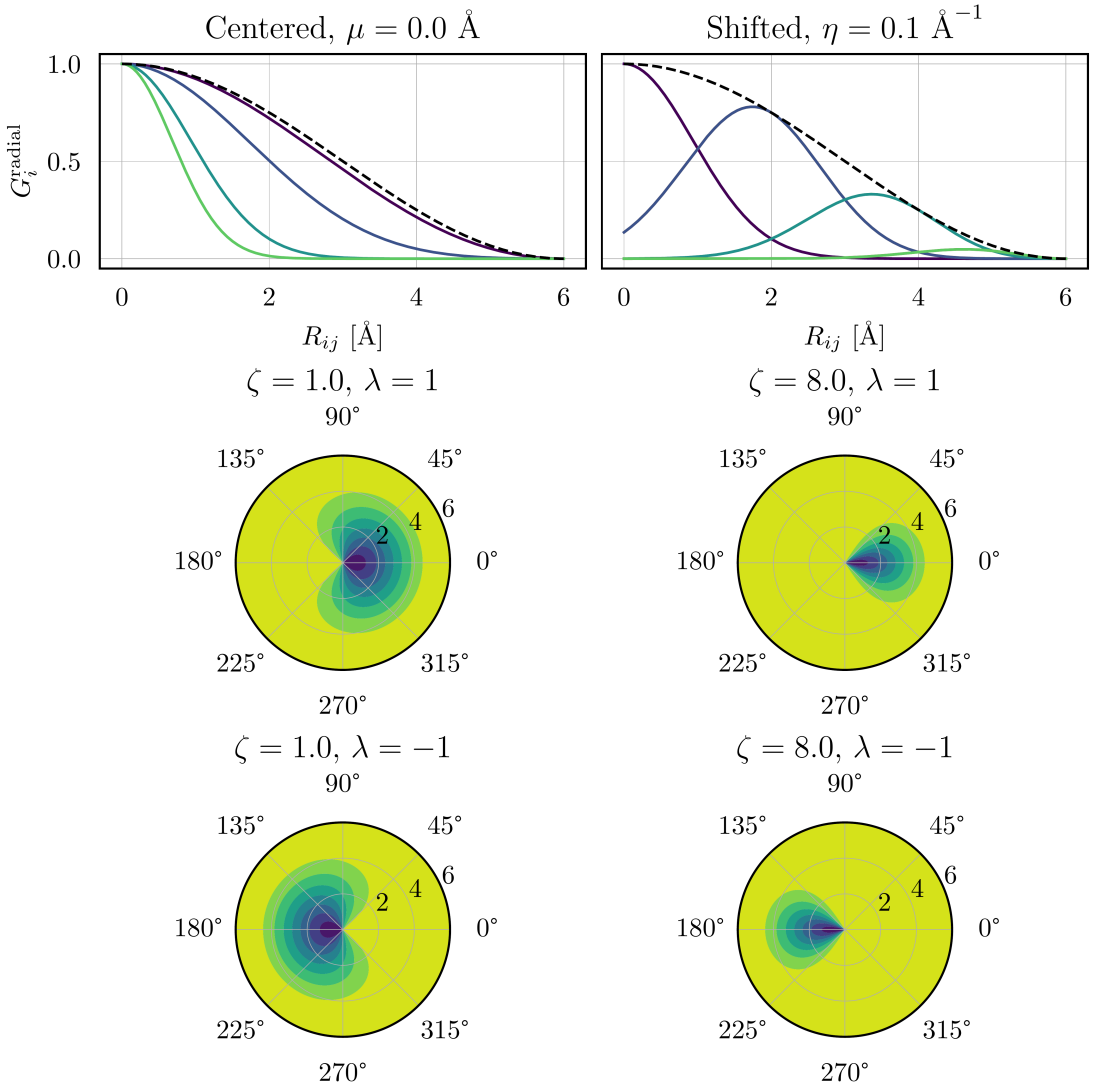


Figure 2.5: Atom-centered symmetry functions as defined in Reference 36. The first row shows two types of radial functions: centered at a given value of $\mu$ with varying values of $\eta$ and on the left and shifted functions with a fixed value of $\eta$ and varying value of $\mu$. The polar plots show four different angular functions depicted for a single term from the sum in Equation 2.128, using $\zeta$ values of 1.0 and 8.0 and $\lambda$ values of $\pm 1$. The more purple regions correspond to high values of the ACSF.

are based on internal degrees of freedom, such as interatomic distances and angles to describe the relevant chemical environment surrounding an atom which renders them independent of a global coordinate frame. They fall into two categories: radial (two-atom) and angular (three-atom). Both types share a cutoff function

$$f_{\text{c}}(R_{ij}) = \begin{cases} \frac{1}{2}\left[\cos\left(\pi \frac{R_{ij}}{R_{\text{c}}}\right) + 1\right] & R_{ij} < R_{\text{c}} \\ 0 \quad \text{otherwise,} \end{cases} \tag{2.126}$$

where $R_{ij} = |\mathbf{R}_j - \mathbf{R}_i|$ and $R_{\text{c}}$ is a cutoff distance after which no neighbors are included in the description. Normally, for practical purposes, this is fixed at

12 $a_0$.[36] Radial ACSF are defined as

$$G_i^{\text{radial}} = \sum_{j \neq i} e^{-\eta(R_{ij}-\mu)^2} f_c(R_{ij}) \tag{2.127}$$

and as such, they encode information about the distribution of distances between atoms $i$ and $j$ through a Gaussian function centered at $\mu$ with a width given by $\eta$, the user chooses these parameters. Radial functions themselves come in two flavors: *centered*, where $\mu$ is fixed to zero distance and the Gaussian widths $\eta$ are varied (Figure 2.5, top left) and *shifted*, where the width is fixed and the position is varied (Figure 2.5, top right); a combination of both is also possible.[189,190] The angular functions are then defined as

$$\begin{aligned} G_i^{\text{angular}} = 2^{1-\zeta} \sum_{j \neq i} \sum_{k \neq i,j} & [1 - \cos(\theta_{ijk})]^\zeta \\ & \times e^{-\eta\left[(R_{ij}-\mu)^2 + (R_{ik}-\mu)^2 + (R_{jk}-\mu)^2\right]} f_c(R_{ij}) f_c(R_{ik}) f_c(R_{jk}). \end{aligned} \tag{2.128}$$

and thus depend on both the angle $\theta_{ijk}$ (with $\cos(\theta_{ijk}) = \mathbf{R}_{ij} \cdot \mathbf{R}_{ik} / R_{ij} R_{ik}$) between a triplet of atoms $i$, $j$ and $k$ and on the respective distances between those atoms through the multiplication by corresponding radial functions. The parameter $\zeta$ has a similar function as $\eta$ in the case of radial functions to control the width. $\lambda = \pm 1$ then defines the orientation of the function's peak. A single term of the sum in Equation 2.128 (*i.e.*, a function of angle and a single distance) is shown in the bottom part of Figure 2.5 for two values of $\zeta$ and $\lambda$.

In a practical setting, one has to predefine a set of ACSF for each atom combination, choosing parameters such that all configurations available to the studied system can be well resolved by the descriptors. For example, a system composed purely of $H_2O$, hence containing only atoms H and O, in principle requires radial ACSF for the pairs H–O and H–H for the hydrogen subnetwork and O–H and O–O for the oxygen subnetwork and angular ACSF for the triples H–H–H, H–H–O, O–H–O for the H hydrogen subnetwork (placing the relevant hydrogen atom in the middle of each triplet) and, similarly, H–O–H, H–O–O and O–O–O for the oxygen subnetwork. Clearly, the number of possible combinations grows quickly with the number of atom kinds, which makes the ACSF method impractical for systems with many different elements, and other types of descriptors must be used. For the training of Behler–Parrinello NNPs, this work relies on the n2p2 software package,[191] which uses a multistream adaptive extended Kalman filter approach to efficiently optimize the NNP parameters exploiting the possibility to tunably include atomic forces as training variables. This explicitly includes the information on PES gradients into the training and was shown to lower force generalization errors while maintaining the accuracy in energy predictions compared to models trained only on energies.[191] The forces from the models — both for training and simulation execution — are readily obtained by analytical differen-

tiation of the predicted energy[191] as

$$\begin{aligned}\mathbf{F}_i &= -\boldsymbol{\nabla}_i E_0 \\ &= -\boldsymbol{\nabla}_i \sum_{j=1}^{N} E_j \\ &= \sum_{j=1}^{N} \sum_{\{\mu\}} -\frac{\partial E_j}{\partial G_j^{(\mu)}} \boldsymbol{\nabla}_i G_j^{(\mu)}.\end{aligned} \tag{2.129}$$

Evaluating this expression requires analytic gradients of the employed ACSFs: the corresponding relevant expressions can be found, for example, in Reference 192.

# 3 | Towards robust and affordable neural network potentials

In this Chapter, we present and discuss our work on developing the computational methodology for efficient generation of NNPs and their deployment in MD simulations published in two publications referred to as Paper I and II and listed as References 43 and 46.

## 3.1 | Paper I: Summary

In the first methodological paper *"Committee neural network potentials control generalization errors and enable active learning"* (Reference 43, reprinted in Appendix C), we introduce a systematic workflow to enable committee NNPs (C-NNPs) for routine use in molecular simulations. In this paper, I have participated primarily by executing and analyzing all validation simulations and preparing the corresponding parts of the manuscript.

A C-NNP is an ensemble combining $N$ individual NNP models that have been trained with different initializations of the NN parameters and, possibly, to a different subset of the full training set. This introduces variation between the models, which allows one to estimate the predicted energy as an arithmetic mean of the individual committee predictions,

$$E = \frac{1}{N} \sum_{i=1}^{N} E_i. \tag{3.1}$$

All force components are predicted in an identical manner. Having a varied committee at hand also allows one to calculate the so-called committee disagreement as a standard deviation of the committee energy (or equivalently, force) predictions

$$\sigma(E) = \left[ \frac{1}{N} \sum_{i=1}^{N} (E_i - E)^2 \right]^{\frac{1}{2}}. \tag{3.2}$$

This quantity is important in the proposed methodology for several reasons. First, it enables the active-learning generation of a training set using the QbC method. In this approach, one begins by training a preliminary C-NNP on a very small number of randomly selected training structures and then predicts $\sigma(E)$ for the whole pool of candidate geometries from which the training set will be selected.

Then, structures featuring the highest $\sigma(E)$ values are added to the training set batch-by-batch, retraining the committee after each addition. Like this, the nascent C-NNP is able to isolate and target configurations that are, loosely speaking, the most challenging for accurate prediction and train on them to learn the corresponding regions of the PES. QbC is discussed in the parts of Paper I revolving around Figures 1 and 2, Figure 3 illustrates the superiority of the C-NNP approach over individual NNP models; we typically pick 8-membered committees as a practical compromise between the accuracy that the approach offers and the computational cost of training as well as using a large number of models at once. Second, $\sigma(E)$ can be monitored on the fly to assess the stability of the MLP-based simulation: once the simulated system ventures into an unknown region of configuration space during time evolution, $\sigma(E)$ tends to grow rapidly as the predictions of the committee members start to diverge due to heavy extrapolation. Finally, $\sigma(E)$ can be used to prevent the system from embarking on such high-disagreement excursions by adding an auxiliary harmonic bias

$$V_\sigma = \begin{cases} \frac{1}{2}k\left[\sigma(E) - \sigma_0\right]^2, & \sigma(E) \geq \sigma_0 \\ 0, & \sigma(E) < \sigma_0 \end{cases} \tag{3.3}$$

to the physical PES, with $\sigma_0$ being a threshold disagreement for the activation of the bias and $k$ the stiffness of the harmonic potential (Paper I, Figure 4).

To gauge the efficiency and accuracy of the proposed workflow, we trained and validated a C-NNP model for simulations of water in various states of matter, including liquid water at different temperatures, several ice phases, and the air/water interface under the classical as well as path-integral description of nuclei over several generations of models. The various state points of water are accessed by model bootstrapping: an improvement of the descriptive qualities of the model using the model itself and only very few new *ab initio* calculations on top of it.

In the present case, we start from a preexisting classical *ab initio* trajectory of liquid water at 300 K to obtain an initial, first-generation C-NNP. This is then used to drive new molecular dynamics simulations starting in the new state points and also using a path integral description of the nuclei with the aim of sampling new candidate geometries. As the next step, we rely on QbC (with a minimal number of *ab initio* single point evaluations) to expand the training set in order to train a model with improved capabilities in the new regions of configuration space. In only four generations and with a training set consisting of only about 800 geometries, we were able to generate a C-NNP capable of describing all of the above-mentioned states in the path integral context with very low error (Paper I, Figure 5). The main results of the validation performed on liquid water simulations at 300 K are then summarized in Figure 6 and showcase an excellent agreement between the C-NNP and the original hybrid DFT data.

## 3.2 | Paper I: Discussion

### 3.2.1 AML: QbC implemented

The ideas presented in the publication are the basis for a publicly available Python implementation of QbC named AML (`https://github.com/MarsalekGroup/aml`) that our group in Prague continually maintains and develops. In the latest public version, the AML code relies on externally provided candidate geometries (*i.e.*, a wide pool of physically meaningful thermal geometries of the studied system from which relevant training points are selected) labeled with the corresponding *ab initio* energies and forces. This comes naturally from an AIMD simulation, where energies and forces are needed on the fly anyway, but once only unlabeled data is at hand, a full recalculation would be needed in order to be able to use the code as is. In a development version, a calculator interface to various electronic structure codes (directly for CP2K, but notably also for ASE, which opens the door to all electronic structure calculators inside it) has been implemented, which allows for the calculation of energies and forces on the fly during QbC for only the selected training structures. New releases of AML are expected in the future.

### 3.2.2 Another perspective on model bootstrapping

Above, we discussed how model bootstrapping can be used to target unseen state points of matter by using QbC and exploratory MD. Another useful application of the same idea would not target new, unexplored regions of a given PES but would allow us to promote the PES to a new one altogether by running QbC with the new electronic structure method on a candidate set created by the old model. Approaching computationally demanding electronic structure methods through machine learning has been previously approached with the so-called $\Delta$-learning;[193] this approach would represent an alternative that does not require learning the difference of two PESs but rather can give access to an explicit C-NNP for the new PES building only on the minimum necessary number of *ab initio* single point evaluations as required by QbC. Such treatment would give access to NNPs that are impossible to obtain using the direct approach through AIMD simulations for extended, condensed-phase systems such as, for instance, post-HF methods. Stable bootstrapping requires the model not to rely heavily on extrapolation to the point that the committee disagreement tends to diverge: to prevent this, the proposed biasing of committee disagreement represents a useful tool. Testing of the approach for realistic systems is a subject of ongoing research in our group.

### 3.2.3 New horizons in MLPs

Behler–Parrinello NNPs (and other invariant models) have successfully enabled highly efficient and large-scale simulations of virtually all kinds of molecular systems. However, the specific form of the architecture based on scalar descriptors,

symmetrically invariant features, and the use of hard-limit cutoff functions can lead to inaccuracies in the description and relatively higher generalization errors compared to more advanced models. An exemplary illustration of a qualitative failure of an invariant model[194] to describe the torsional energy profile of relative cyclopentadiene ring rotations in a ferrocene molecule.[195] These shortcomings are addressed by the advent of equivariant message-passing models,[196] NN architectures with tensor-like features and equivariant internal transformations.[195,197,198] By construction, such models allow for the propagation of structural information regarding atomic environments beyond the given interaction cutoff: the ferrocene problem is solved by employing the equivariant PaiNN model.[195] In addition, equivariant models are not limited by externally supplied descriptors, exhibit comparable computational efficiency, and have been shown to have higher data efficiency, therefore requiring smaller training sets than invariant models. These considerations suggest that equivariant models are, in fact, the likely future direction of MLP-oriented research. On another note, we mention the emergence of foundational models, *i.e.*, universal models trained on very large and diverse data sets that offer accuracy and robustness over extensive parts of chemical and configurational space.[199] For example, this could mean that a single model will be able to describe a liquid structure, isolated molecules, a reaction on a metal surface, and a solid material with the same flexibility and precision. A universal MLP at a quantitative level of accuracy remains elusive as of this moment. However, recent development has introduced several large-scale MLPs which aim at being universal and which have been shown to attain qualitative descriptive capabilities over a wide range of molecular systems.[199,200] While these cannot yet be used in an out-of-the-box fashion for applications in accurate molecular modeling, they have the potential to become extremely useful as a physically well-based starting point, for example, in our case, to generate cheap structures for QbC completely free of *ab initio* simulations.

## 3.3 | Paper II: Summary

In *"Reducing the cost of neural network potential generation for reactive molecular systems"* (Reference 46, reprinted in Appendix C), we identify a potentially serious drawback of the methodology proposed in Paper I pertaining to systems where chemical reactions and other high-barrier transitions are to be described. Specifically, the reactive equivalent of obtaining candidate geometries through short AIMD simulations in non-reactive systems (or alternatively, in systems with ultrafast reactions that can be sufficiently sampled thermally) is enhanced-sampling AIMD. This may become prohibitive once accurate and computationally demanding *ab initio* methods are required for substantially extensive systems. It is, therefore, desirable to devise a sampling method that will yield thermal reactive geometries that can be used as candidates for QbC at a lower computational cost than that of full-scale dynamical simulations. Here, we introduce such methodology for gas-phase systems, which we call transition tube sampling (TTS) and which combines the knowledge of a path through configuration space that describes the reactive transition (such as, but not limited to, a

minimum energy path (MEP)) and a set of local normal mode expansions with an approach known as normal mode sampling (NMS) to obtain thermal geometries along the whole reaction (Paper II, Figure 1). Existing literature contains several definitions of NMS, most relying on random displacements from a uniform distribution of normal coordinates.[201,202] In the present case, NMS stands for essentially a correlation-free MC exact thermal sampling from the Gaussian distribution of normal coordinates around a reference configuration at an inverse temperature $\beta = (k_\mathrm{B}T)^{-1}$ (Paper II, Equations 1 and 2). Apart from being exact under the harmonic approximation, it brings around the advantage of being easily and exactly quantized by switching from the classical $\beta$ to the so-called effective quantum inverse temperature

$$\beta^*(\beta, \omega) = \frac{2}{\hbar\omega} \tanh\left(\frac{\beta\hbar\omega}{2}\right) \leq \beta \tag{3.4}$$

for each vibrational mode with frequency $\omega$ separately: this gives access to predicting thermal geometries consistent with path-integral replicas (the thermal density of a quantum harmonic oscillator is Gaussian, see the Supporting information of Reference 46). This puts a perspective on methods that attempt to incorporate quantum properties by elevating the physical temperature by a constant shift: such an approach is not physically well founded, as according to Equation 3.4, each vibrational mode has a different effective temperature, and, therefore, the magnitude of the quantum effect is different as well. How pronounced these quantum effects are is shown in Figure 3.1, which depicts the dependence of the quantity $\beta^*/\beta \leq 1$ on $\omega$ and $\beta$. This suggests that the most affected modes are those with high frequencies and at low temperatures, and

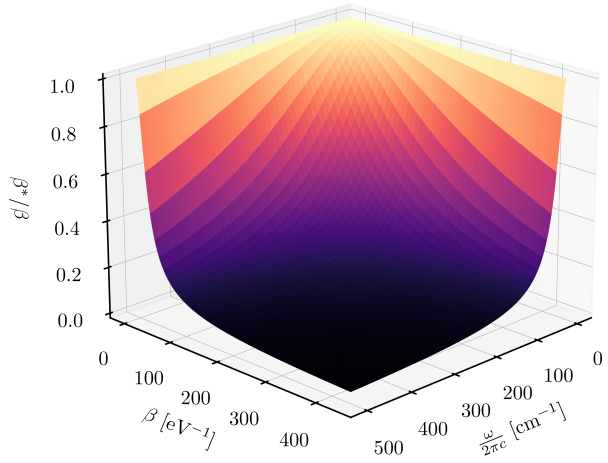


Figure 3.1: Graphical representation of the relationship given in Equation 3.4. The region of the classical limit at high temperatures and low oscillation frequencies with $\beta^* \to \beta$ corresponds to the light coloration of the surface; conversely, the region of pronounced quantum effects corresponds to the dark coloration. For orientation, $\beta$ at the temperature of 300 K is equal to approximately 39 eV$^{-1}$.

conversely, softer modes at higher temperatures tend to behave more classically. Note that at 300 K (which corresponds to the inverse temperature of approximately 39 $\text{eV}^{-1}$), physical molecular vibrations on the order of $10^2$ to $10^3$ $\text{cm}^{-1}$ are affected by quantum effects in very different ways.

The presented TTS methodology is tested on creating C-NNPs for three different gas-phase molecules. First, we look at the simple example of benzene, which has no reaction, and therefore, the TTS reduces to a simple, single-reference NMS. This validates the correctness of the underlying physics given by Equation 3.4 in a simple, controllable context (as discussed below). Then, we address two molecules with intramolecular proton-sharing reactions. On the one hand, this is malonaldehyde, which we use to showcase that TTS can be efficiently combined with active learning to obtain an accurate C-NNP despite the presence of anharmonicities beyond the reaction that we are trying to describe. On the other hand, we look at the DABQDI molecule (which will be discussed in detail in Chapter 6). The implementation of the TTS method has been realized in the Python programming language and is expected to be released as a part of a future public version of the AML code.

## 3.4 | Paper II: Additional results and discussion

### 3.4.1 Normal mode distributions in gas-phase benzene

As it was stressed explicitly in Paper II, the TTS ensemble does not correspond to any physical ensemble, and no physical quantities should be calculated over it: it merely serves an auxiliary purpose in NNP training. However, in the simple case of gas-phase benzene simulations at 300 K, an interesting similarity between the true canonical ensemble and the TTS ensemble appears, since the thermally available PES at this temperature is closely represented by its harmonic approximation — for that reason, benzene is often highlighted as an example of a "highly harmonic system" that can be accurately described as a collection of independent harmonic oscillators in individual normal coordinates. This is already clear from the distributions of geometric properties in Figure 2 of Paper II, which shows a comparison of MD and TTS statistics. However, it is useful to illustrate this explicitly through the full, multivariate Gaussian distribution from which the TTS samples are drawn. A plot comparing the distribution of all normal coordinates from AIMD simulations (shaded areas) and TTS (solid lines) is shown in Figure 3.2 for both the classical and quantum case (red and blue, respectively). The values of the normal coordinate were obtained by projecting each immediate mass-weighted configuration $\mathbf{Q} \equiv \mathbb{M}^{-\frac{1}{2}}\mathbf{R}$ onto the corresponding normalized normal mode vectors

$$\Omega_i = \mathbf{Q} \cdot \mathbf{\Omega}_i. \tag{3.5}$$

Clearly, the TTS and the MD distributions exhibit a nearly perfect overlap in both the classical and quantum case, which represents direct evidence for the correctness of the physics encoded in Equation 3.4. The quantum TTS distributions retain their classical Gaussian shape but are non-trivially widened as the

difference between $\beta^*$ and $\beta$ grows with increasing oscillation frequency; this effect is reliably reproduced by *ab initio* PIMD simulations that make no harmonic approximation. In less harmonic systems, such as the case of malonaldehyde discussed in detail in Paper II, the level of agreement between the true, anharmonic distribution and that of the TTS samples would be lower, possibly requiring active learning to provide good coverage of the anharmonic PES.

### 3.4.2 Distribution of malonaldehyde TTS geometries

As a supplementary plot to the ones presented in the malonaldehyde section of Paper II, the distribution of the TTS samples is shown in Figure 3.3. In the top panel, the proton-sharing MEP, which serves as the entryway into the TTS procedure, is presented as a function of the dimensionless reaction coordinate $\xi$.

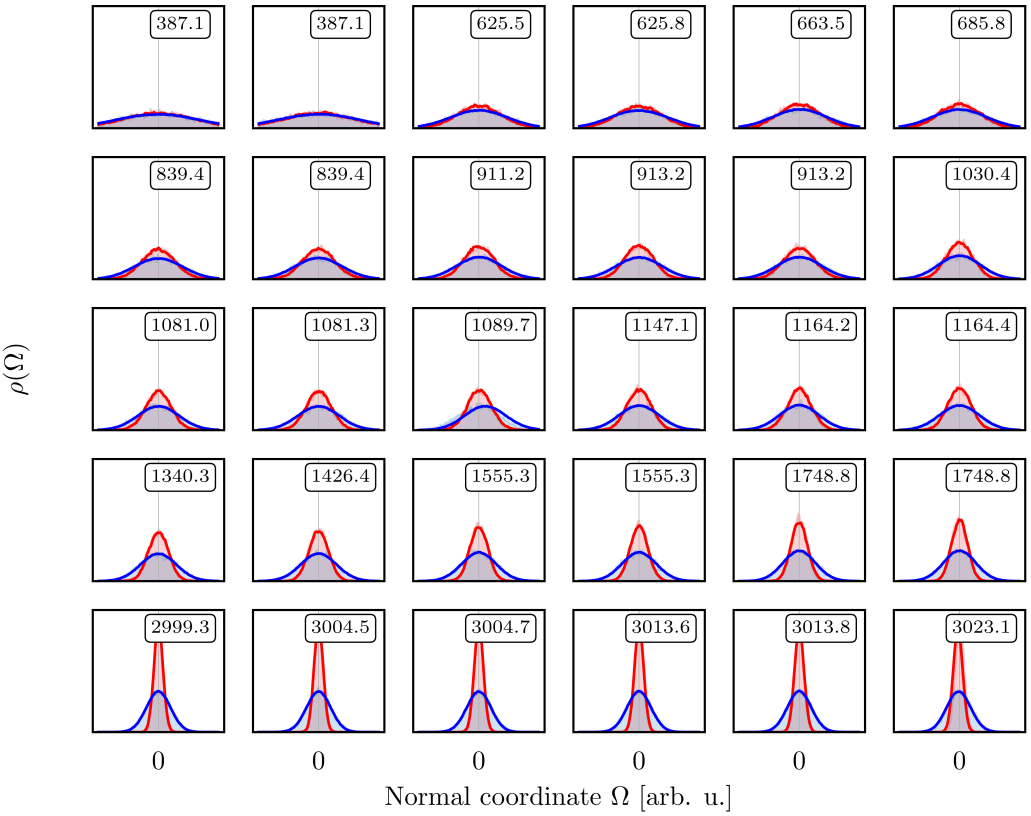


Figure 3.2: Statistical probability density distributions of normal mode coordinates in gas-phase benzene at 300 K obtained by projecting the immediate geometry on a set of normal mode vectors calculated for the optimal minimum geometry. The red-shaded distributions originate in a classical AIMD simulation, whereas the blue ones were obtained from an *ab initio* PIMD simulation. The red lines then represent the distribution of classical TTS geometries, and the blue lines their quantum counterpart. Each panel has the corresponding vibrational wavenumber in the units of $\mathrm{cm}^{-1}$ shown in the top right corner.

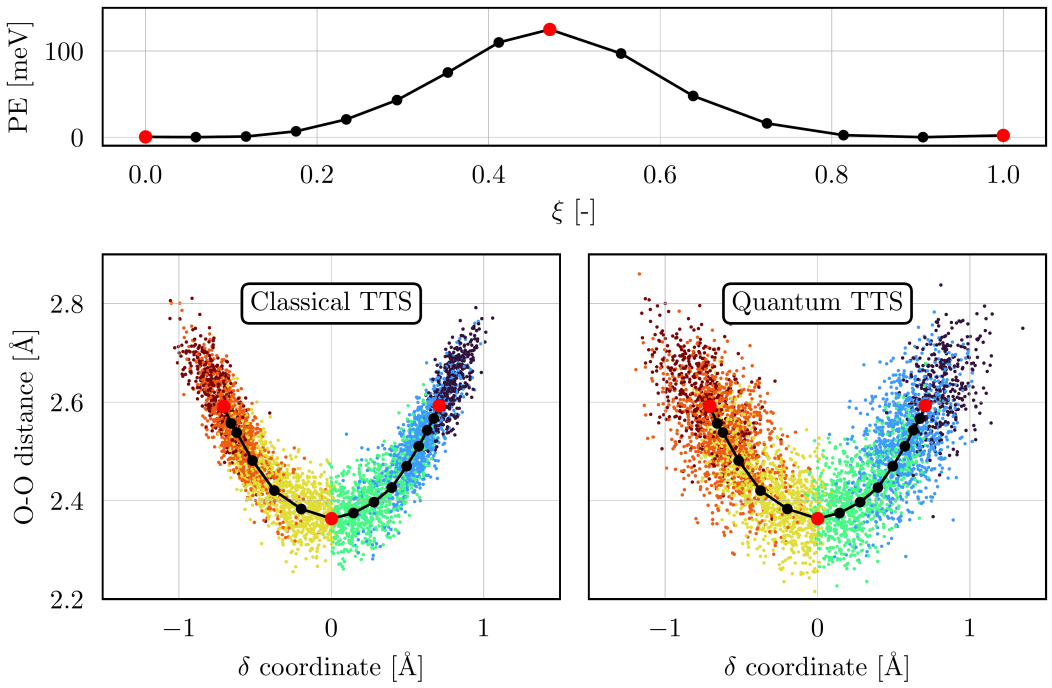


Figure 3.3: TTS of malonaldehyde. Top panel: the potential energy (PE) of the molecule as a function of the proton-sharing MEP described by the dimensionless reaction coordinate $\xi$. The reactant and product minima and the transition state are highlighted in red. Bottom panels: the same reaction MEP (black with red highlights) shown in a suitably chosen subspace of geometric descriptors $d_{\mathrm{OO}'}$ and $\delta$ to describe the proton-sharing reaction (see main text for definitions). Each point in the scatter plots represents a TTS-generated geometry projected into the same subspace. Points that share the same color belong to one control point. Note the broadening of the quantum distribution on the right compared to the classical distribution on the left.

The two end-point minima and the transition state, which are used as TTS control points, are highlighted in red. The two bottom panels then show the same MEP in the subspace given by two geometric coordinates: the oxygen–oxygen distance

$$d_{\mathrm{OO}'} \equiv |\mathbf{R}_{\mathrm{O}} - \mathbf{R}_{\mathrm{O}'}| \tag{3.6}$$

and the proton-sharing coordinate

$$\delta \equiv |\mathbf{R}_{\mathrm{O}} - \mathbf{R}_{\mathrm{H}}| - |\mathbf{R}_{\mathrm{O}'} - \mathbf{R}_{\mathrm{H}}|. \tag{3.7}$$

This pair of descriptors is commonly used to describe proton-sharing processes because the heavy atoms are brought closer together during the course of the reaction, creating the characteristic V-shaped path. Alongside the MEPs, Figure 3.3 contains a scatter plot of the geometries generated by TTS with the color of each cluster denoting its correspondence to a given control point. This kind of plot can be understood as a real-world equivalent of the illustrative TTS on a model 2D PES shown in Figure 1 of Paper II. Note that the quantum TTS distribution is broadened in the perpendicular direction to the MEP due to the

inclusion of $\beta^*$ for the perpendicular modes (the same effect was illustrated in Figure 3.2 for benzene).

### 3.4.3 Going beyond the gas phase

While gas-phase reactions clearly carry a great deal of relevance in molecular physics ranging from atmospheric chemistry to industrial processes carried out in the gas phase, it is important to realize that various condensed-phase and hybrid arrangements, such as reactions in solutions, on surfaces, at interfaces, and in solid materials, are perhaps of even larger technological and biological significance. At the same time, the generation of reactive MLPs for gas-phase systems could be comfortably brute-forced via explicit *ab initio* simulations on modern supercomputers, technically making TTS not necessary, even though it was clearly shown in Paper II to lead to a significant speed-up of the whole process.

Therefore, to close this Chapter, we shall hypothesize about the possible generalizations of the TTS method beyond the gas phase, where methodology of this sort is inevitable. As a standalone sampling method, TTS is fundamentally limited by the harmonic approximation and the small number of configurational minima one can take into account. As such, it can only be used for non-gas-phase systems where the parts that do not actively participate in the reaction are addressable, at least to a decent degree, by the harmonic approximation. This includes, for instance, various crystals, reactive systems encased in isolated solid matrices, or surface-bound molecules without significant surface diffusion; here, TTS can potentially yield computationally affordable, first-generation C-NNP models that can be further refined by active learning, if necessary. A bigger challenge is represented by reactive systems where disordered condensed phase comes into play, *e.g.* liquids, solutions, and interfaces with a liquid component. In this case, extremely many configurational minima are available, and using TTS alone makes it practically impossible to probe even a relevant subset of them for sufficient representation of configurations in the candidate set. On the other hand, simulation methods such as MD are very efficient in scanning these slightly rippling, nearly flat PESs of liquid systems. Therefore, one can imagine a combined method that will use the capability of TTS to sample geometries along a well-defined reaction path supplemented by sampling thermal configurations using some kind of molecular simulation. The exact nature and extent of this combination and its deployment to study realistic condensed-phase reactions will be explored in future studies.

# 4 | Electronic and molecular structure of solvated benzene radical anion

The following Chapter summarizes and discusses our research focused on the benzene radical anion solvated in liquid ammonia and the consequent questions that it opens. The theoretical core of this relatively extensive research project that combines theory with experiment is represented by two publications referred to as Papers III and IV and listed as References 71 and 72, respectively, which are reprinted in Appendix C). In both publications, I figure as the first author and had a primary role in the performing of the simulations, design and execution of the data analysis, and in the preparation of the manuscripts.

## 4.1 | Papers III and IV: Summary

The benzene radical anion is notably formed in the environment of liquid ammonia when a solvated electron attaches to a molecule of benzene during the course of the initial mechanistic step of the Birch reduction (Paper III, Equation 1). Intrigued by the chemistry of solvated electrons and motivated to gain insight into this technologically important process, we performed AIMD simulations of the benzene radical anion in bulk liquid ammonia using the hybrid revPBE0-D3 density functional.

This choice of functional is shown in *"Benzene radical anion in the context of the Birch reduction: when solvation is the key"* (Paper III) to be crucial for a correct description of the studied system to prevent an overdelocalization of the excess electron due to self-interaction error at the otherwise computationally much more viable GGA level of theory. We show that at the hybrid DFT level, the spin density stays spontaneously localized almost exclusively on the aromatic solute (Paper III, Figure 1). This is consistent with the experimentally implied fact that the solvated radical anion represents an electronically stable bound state, unlike in the gas phase, where it can only be measured as a short-lived resonance. Apart from these considerations, Paper III does not discuss electronic structure problems, but rather addresses the questions of molecular geometry of both the radical anion solute itself and its solvation structure, while comparing them to neutral benzene in solution as a reference. Importantly, our simulations demonstrate that the solute undergoes a dynamic Jahn–Teller effect (Paper III,

Figures 2–4), which causes its geometry not to be a fixed, hexagonal one like in the case of neutral benzene, but rather a dynamically evolving one switching between two distinct symmetries in a reduced-symmetry point group. The solvation structure is analyzed via spatial distribution functions (SDFs) and their integrals in the form of various angularly restricted radial distribution functions (RDFs) (Paper III, Figures 5, 6). These point to the fact that two solvation regimes are present in the studied systems: hydrophobic solvation that can be expected for a hydrocarbon solvated in a polar solvent and a characteristic $\pi$-hydrogen bond that is formed by the interaction of the polar hydrogen of the solvent molecules with the $\pi$-electron density of the solute. Finally, the discussion in Paper III revolves around the prediction of vibrational spectra and finds plausible evidence for $\pi$-hydrogen bonding in the infrared spectrum (Paper III, Figure 7). Interestingly, the very diffuse character of the excess electron in the benzene radical anion causes its solvation to be only slightly more structured than in neutral benzene. A detailed study of $\pi$-hydrogen bonds in solvated benzene, including their structure, dynamics and vibrational spectroscopy, is presented in Paper V in Chapter 5.

As the name suggests, the focus of *"Electronic structure of the solvated benzene radical anion"* (Paper IV) is the complementary electronic part to Paper III. The discussion there consists of two parts. First, we inspect the manifestation of the Jahn–Teller effect on the spin density. Using a rather involved combination of dimensionality reduction of the 3D spin density into a finite vector space of Fourier coefficients with unsupervised machine-learning methods, we find that the spin density also evolves dynamically between two distinct symmetries, closely following the underlying molecular geometry (Paper IV, Figures 2–4). This shows, loosely speaking, a certain level of inertness of the benzene radical anion to the symmetry-breaking by the presence of the solvent: qualitatively, the observed Jahn–Teller effect is consistent with symmetry arguments that would be valid in the gas phase. Note, however, that unlike in the gas phase, the solution environment allows one to actually observe this phenomenon in equilibrium, as the species is stabilized here. The issue of solvent-induced electronic stability is set on a rigorous footing in Paper IV by demonstrating that the benzene radical anion represents a bound state (Paper IV, Figure 5). To this end, we model the valence EDOS using the $G_0W_0$ method, which estimates the binding energy of the excess electron to be around $-2.3$ eV relative to the vacuum level (note that this is even slightly more bound than the binding energy of $-2.0$ eV of the free solvated electron[62]). To inspect the EDOS projected on the various molecular entities present in the system, we introduce the so-called projected density of states (PDOS), which allows us to isolate these contributions. This has multiple advantages, for instance, it uncovers solute states hidden under the overwhelming solvent peaks (due to larger concentration) and also allows us to inspect the radially resolved solvent PDOS to find a slight effect on the solvent electron binding energies in the first solvent shell (Paper IV, Figure 6). These results can be used to justify the usual isolation of experimental solute XPS spectra by subtraction of the neat solvent, as projection is only possible in the realm of theoretical modeling.

## 4.2 | Papers III and IV: Follow-up research and discussion

### 4.2.1 Solvent-induced stability

Arguably the most important result of Paper IV is the calculation of the excess electron binding energy in the bulk liquid ammonia solution of the benzene radical anion that proves the existence of a bound state. An indisputable advantage of the $G_0W_0$ approach is the fact that it gives direct access to physically meaningful bulk binding energies without having to rely on KS orbital energies or resort to even lower levels of theory. On the other hand, the calculations performed in order to obtain the data presented in Paper IV do not shed light on the stabilization process itself, *i.e.*, how and, perhaps more importantly, why the benzene radical anion is stabilized upon transitioning from the gas phase to the solution. In addition, we have previously seen the $G_0W_0$ method produce unphysical results in the case of solvated electrons (as discussed in Chapter 1). This was most likely due to basis set convergence issues owing to the stringent requirements on the basis set needed to describe the off-atomic density peaks of the solvated electrons. Since this is not a problem with the benzene radical anion, where the excess electron density is localized on atoms as usual, we do not strictly have a reason to doubt the obtained results, but having a consistency check at hand would be reassuring.

For these reasons, we have revisited the calculation of the excess electron binding energy in the benzene radical anion from another methodological standpoint using vertical ionizations in *"Benzene radical anion microsolvated in ammonia clusters: modeling the transition from an unbound resonance to a bound species"*[73] (this publication is not attached to this thesis; as the second author, I supervised the execution of the calculations and contributed to the manuscript preparation, but did not perform calculations myself).

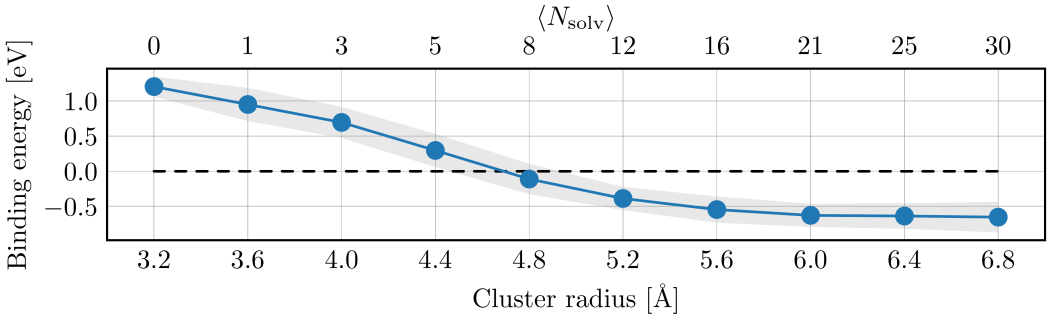


Figure 4.1: Binding energies calculated for small clusters consisting of ammoniated benzene radical anion at the revPBE0-D3/def2-TZVP level of theory. The top horizontal axis shows the average number of solvent molecules for the corresponding cluster radius given at the bottom axis. The shading gives the magnitude of the standard deviation of the binding energies.

Here, one approaches the definition of Dyson equation eigenvalues rather literally and calculates the binding energy of the highest-energy electron as

$$E_{\mathrm{B}} = E_0^n - E_0^{n-1}, \tag{4.1}$$

*i.e.*, by explicitly calculating the ground state energies of the original anionic system with $n$ electrons and that of the neutral system after vertically removing a single electron and subtracting them. In contrast to the $G_0W_0$ approach, this one cannot be used to model all binding energies since one is not free to choose which electron gets detached — it will always be the top one according to the aufbau principle — and cannot be used for periodic boxes due to the non-convergence of the Madelung sum of the residual charged periodic system. Therefore, these calculations were performed based on molecular clusters carved out of the thermal periodic geometries sampled by AIMD simulations in open boundary conditions, consistently with the aforementioned solvated electron work[62] in Chapter 1. This allowed us to answer several questions regarding the transition from the gas phase into the solution by considering spherical clusters centered around the solute with progressively increasing radii. First, we show that as few as 6–8 ammonia molecules are needed to bring the binding energy into the negative numbers (Figure 4.1, top panel). Strictly speaking, the preceding positive binding energies before reaching this point do not have a physical meaning since an $\mathcal{L}^2$-integrable basis is used to evaluate them, which is not suitable for addressing resonances; once the binding energy becomes negative, the quantitative values become meaningful. At the same time, the isolated benzene radical anion submerged into a polarizable continuum with the dielectric constant $\epsilon_{\mathbf{r}} = 22.6$ corresponding to liquid ammonia already exhibits a binding energy very close to the predicted bulk value of $-2.3$ eV. This suggests that the radical anion is stabilized mainly by electrostatic screening via the dielectric environment produced by the solvent rather than specific interactions with the ammonia molecules.

Finally, we explore what number of solvent molecules one needs to reach the bulk limit without resorting to polarizable continuum solvation. Clearly, the DFT calculation of clusters counting thousands of molecules is not an option due to its prohibitive computational requirements. These calculations were thus approached using a special form of quantum mechanics/molecular mechanics description known as effective fragment potentials[203] to represent the solvent beyond the molecules in the closest distance to the solute. Several particular methods and numerical choices are compared in Reference 73; here, the binding energy curve that gives the best agreement with the $G_0W_0$ results is shown in Figure 4.2. A consistent value of $-2.3$ eV is obtained in clusters with >4000 solvent molecules. In summary, these calculations point to the fact that the benzene radical anion is stabilized by the electrostatic screening induced by the solvent rather than chemically specific interactions, and while already very few solvent molecules produce a bound state, a large number solvent molecules are needed to reach the bulk behavior. The stability of the benzene radical anion was observed experimentally in electron attachment experiments to ammonia clusters doped with benzene molecules: here, the energy released by the binding of the incident electron was observed to cause solvent molecules to evaporate from the clusters,

measured by mass spectrometry.[204]

### 4.2.2 Experimental correspondence

The theoretical prediction of the EDOS of the benzene radical anion and of neutral benzene in Paper IV raises the question of whether the corresponding experimental spectra can be measured by liquid microjet XPS.

In *"Photoelectron spectroscopy of benzene in the liquid phase and dissolved in liquid ammonia"*,[74] our experimentalist colleagues report that the solubility of benzene in liquid ammonia at −50 °C of approximately 400 mM is sufficient for the resolution of XPS by a large margin and successfully measure the XPS spectrum of that solution (once again, despite my co-authorship of the publication, this paper is not attached to this thesis owing to my contribution by data analysis and manuscript preparation, but not by adding relevant new calculations). This exhibits excellent agreement with the theoretical predictions as shown in Figure 4.3 for both the total spectra and the solute contribution obtained, respectively, by projection and by subtraction in the calculation and the experiment.

However, an identical experiment for the benzene radical anion (realized by the addition of an alkali metal into the solution of benzene in liquid ammonia in analogy with the solvated electrons/dielectrons XPS experiments discussed in Chapter 1) was not successful and only showed spectroscopic evidence of neutral benzene and a solvated electron: the excess electron feature at ca. −2 eV would be indistinguishable between the solvated electron and the radical anion anyway, but no shifts of the lower solute states were observed as predicted by theory (*cf.* Paper IV, Figure 5). To explain why there is no benzene radical anion observed in the XPS experiments, one has to come back to more fundamental considerations. In particular, we have shown and discussed that the benzene radical anion in

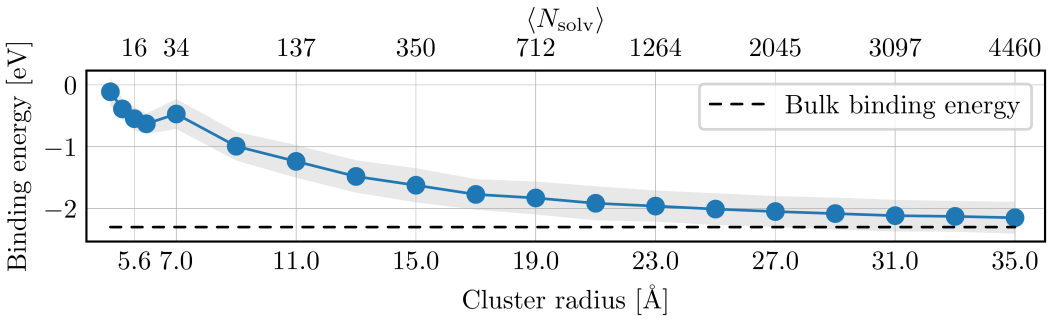


Figure 4.2: Binding energies calculated for larger clusters consisting of ammoniated benzene radical anion. The calculation was perfomed using a dual-potential approach: the benzene radical anion and all solvent molecules up to 6 Å were treated at the revPBE0-D3/def2-TZVP level of theory, while all solvent at larger distances was treated using EFP. The top horizontal axis shows the average number of solvent molecules for the corresponding cluster radius given at the bottom axis. The dashed horizontal line gives the $G_0W_0$ prediction of the bulk value of −2.3 eV.

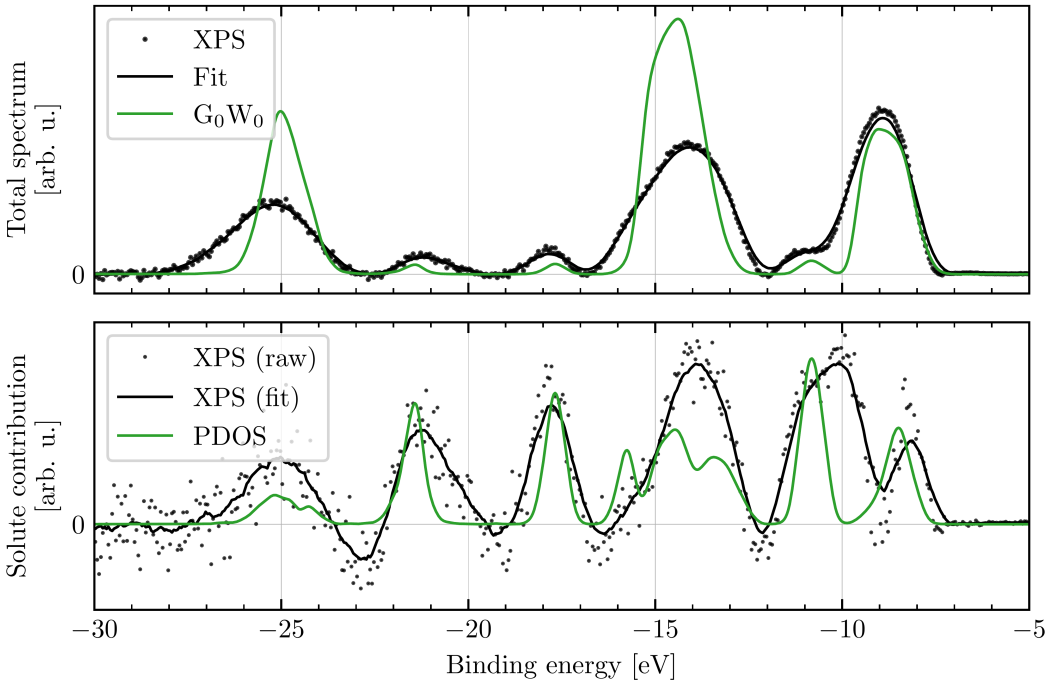


Figure 4.3: Comparison of XPS measurements and $G_0W_0$ calculations of neutral benzene solvated in liquid ammonia. Top panel: The measured total XPS spectrum, including the solute as well the solvent (black points) was fitted with a smooth curve (black line).[74] The calculated EDOS is shown in green (same data as in Figure 5 of Paper IV). Bottom panel: Same quantities as above, but only the contribution of the solute. The experimental curve was obtained by subtraction of the neat solvent spectrum; the theoretical curve was obtained by projection, as described in detail in Paper IV.

liquid ammonia forms an electronically stable bound state and a minimum at the corresponding PES. However, we did not look at its thermodynamic stability, *i.e.*, what does its equilibrium with solvated electrons in the liquid ammonia solution

$$C_6H_6 + e^- \rightleftharpoons C_6H_6^{\bullet -} \tag{4.2}$$

look like. Perhaps, the benzene radical anion is not a strongly populated state despite its electronic stability. Addressing this question correctly from a computational perspective means addressing the free-energy difference $\Delta F$ between these two states, which is by all means no simple task. Even without considering the computational resources needed to perform some sort of an enhanced-sampling simulation at a hybrid DFT level of theory with the extended basis set needed to describe solvated electrons, it is unclear what the CV describing this reaction should be in the first place. Nemirovich and coworkers[205] have circumvented the difficult explicit free energy calculation by making the approximation that $T\Delta S \sim 0$ for the reaction (which they present as a well-reasoned step in this case) and thus $\Delta F \sim \Delta U$, where $\Delta U$ is the adiabatic difference in potential energies between the states that includes molecular relaxation. Interestingly, building on these premises, they find that in the single solvated electron case, the

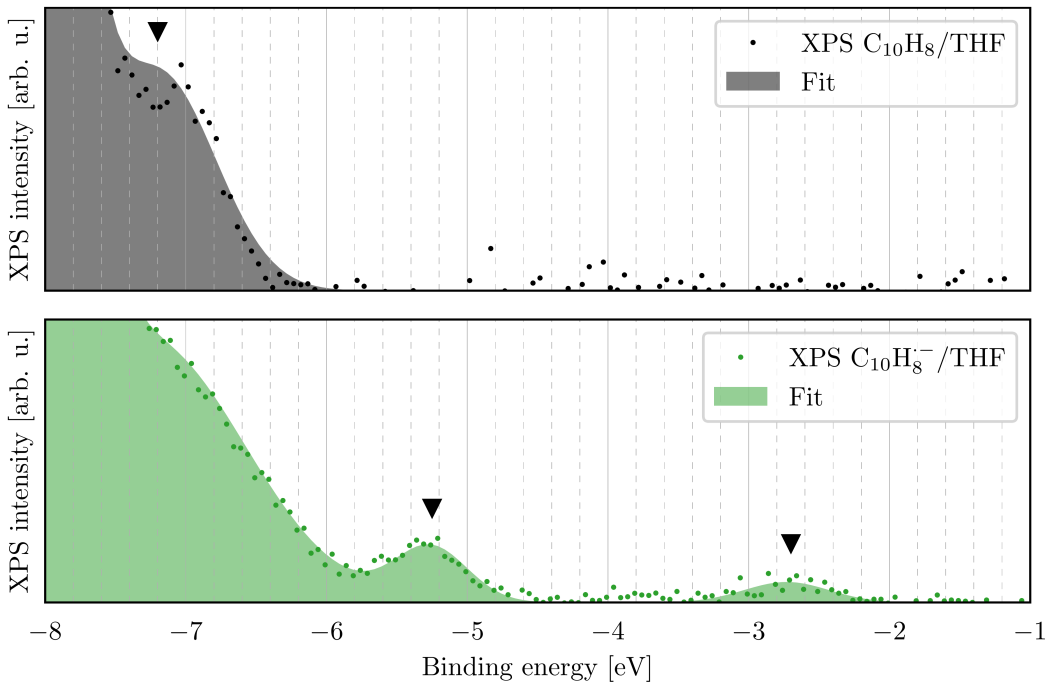


Figure 4.4: Experimental XPS measurement of naphthalene and its radical anion in tetrahydrofuran (THF).[75] The top panel shows the spectrum for the neutral species, the bottom one for the anion. Important spectral features are highlighted by the black arrows.

radical anion is the favored state

$$C_6H_6 + e^- \longrightarrow C_6H_6^{\bullet-} \tag{4.3}$$

but at higher concentrations that feature dielectrons, the radical anion is disfavored

$$C_6H_6 + e_2^- \longleftarrow C_6H_6^{\bullet-} + e^-. \tag{4.4}$$

Now, the resolution of the XPS experiment is limited by the concentration of the solutes and does not allow one to measure in the single solvated electron regime with an appropriate signal-to-noise ratio. Therefore, the performed experiments rather targeted the dielectron regime and it is consistent with the theoretical groundwork that no radical anion was observed. A more suitable experimental approach capable of measuring much lower solute concentrations will be necessary to capture the fingerprints of the benzene radical anion in liquid ammonia. Note that this does not invalidate our calculations presented in Paper IV in any way but also illustrates the fact that sometimes the overall picture is bigger than a particular calculation can reveal.

At this point, a question was raised whether changing the chemistry of the system, such as perhaps measuring a different aromatic radical anion solute in a different solvent, can represent a problem more suitable for a liquid-microjet XPS measurement. As a result of this discussion, a recently published paper *"Stability and reactivity of aromatic radical anions with relevance to Birch reduction"*[75]

reports the measurement of the naphthalene radical anion in tetrahydrofuran, which can be obtained at much higher concentrations; the measured spectra are shown in Figure 4.4 (again, while I have a minor contribution to this publication, it is not attached to this thesis but rather its highlights are discussed for the sake of the big picture perspective). Importantly, note that the studied system follows the same trend as the benzene radical anion discussed in Paper IV. Neutral naphthalene has its highest-occupied state at around −7 eV, just at the onset of the valence spectrum of the solvent (Figure 4.4, top panel). After binding the electron, the resulting radical anion is recognizable for two reasons: first, a new feature appears at −2.7 eV (*cf.* the −2.3 eV peak predicted for the benzene radical anion) and, second, a non-trivial rearrangement of the solute spectral features takes place in the region between −5 and −8 eV (Figure 4.4, bottom panel).

### 4.2.3 Remarks on the interpretation of XPS spectra

To close this Chapter, we will address some of the details that were brought up during the various discussions of XPS spectra both from the theoretical and experimental points of view.

#### 4.2.3.1 Origins of different peak broadenings and intensities between XPS and EDOS

During the course of this text, we have observed numerous times (think of the data in Figures 1.3 or 4.3) that experimental XPS peaks are broadened in comparison to the calculated EDOS peaks and have qualitatively different intensities. The alteration of peak widths can be attributed to two origins. First, our simulations at the time did not include NQEs and, therefore, the experimental spectra are broadened by quantum effects which are not reflected in the simulations with classical nuclei. Second, the experiment is affected by inelastic scattering processes that take place during the realistic electron detachment from the sample, which again contributes to the experimental broadening in comparison to the calculated peaks that only contain idealized vertical binding energies. The spectral intensities in the experiment reflect non-trivial absorption cross-sections for each ionization, whereas the calculation considers all ionizations with the same probability.

#### 4.2.3.2 Gas-to-liquid shifts

Finally, let us relate to an intriguing physical problem of gas-to-liquid shifts shown in Figure 1.3 where liquid ammonia exhibits a fairly constant gas-to-liquid shift of 1 – 2 eV over the studied energy range in comparison to the gas phase spectrum. One would naturally expect this shift to be system-dependent. However, experimental reality suggests otherwise: most, even chemically unrelated liquids, such as ammonia, benzene, or tetrahydrofuran mentioned in this work,[52,74,75] exhibit similar shifts of their spectral features by 1 – 2 eV. This surprising lack of dependence on the chemical nature of the liquid can be explained semi-quantitatively

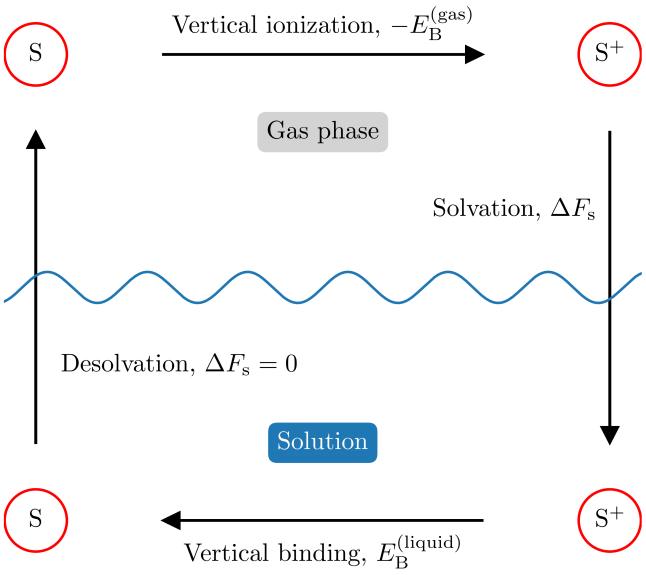


Figure 4.5: The Born–Haber cycle for predicting gas-to-liquid shifts in XPS spectra of liquids.

using a very simple but insightful model, which models the liquid as a continuum and approximates the solvation energy using the Born equation. To this end, we build a Born–Haber cycle as shown in Figure 4.5: we are reluctant to call the cycle "thermodynamic" as it contains vertical processes without geometry relaxation, but its principle is similar to true thermodynamic cycles. We start with an uncharged, structureless spherical species $S$ in the gas phase defined by an effective radius $R$ in the top left corner of the scheme: this can represent either a single molecule of the liquid in question (*e.g.*, ammonia in liquid ammonia) or a solute (*e.g.*, benzene in liquid ammonia). First, we perform a vertical ionization of an electron from $S$ for energy $-E_{\mathrm{B}}^{(\mathrm{gas})}$, giving us a nascent gas-phase cation

| Liquid | $n$ | $R$ [Å] | $\Delta E_{\mathrm{B}}$ predicted [eV] | $\Delta E_{\mathrm{B}}$ observed (h. p.) [eV] |
|---|---|---|---|---|
| $H_2O$ [206] | 1.33 | 2.24 | 1.40 | 1.45 |
| $NH_3$ [74] | 1.39 | 1.72 | 2.01 | 1.97 |
| THF [75] | 1.40 | 2.63 | 1.36 | 1.28 |
| $C_6H_6$ [74] | 1.50 | 2.95 | 1.36 | 0.82 |

Table 4.1: Illustration of the gas-to-liquid shift prediction using the Born–Haber cycle for examples of chemically distinct liquids. The abbreviation h. p. stands for "highest peak", referring to the shift of the spectral feature of the highest-energy electrons.

$S^+$. Then, we model the solvation of $S^+$ in the liquid phase by submerging it into a continuum with a dielectric constant $\epsilon_\mathrm{r}$: the Born solvation free energy for the process is

$$\Delta F_\mathrm{s} = -\frac{Z^2 e^2}{8\pi R}\left(1 - \frac{1}{\epsilon_\mathrm{r}}\right) \tag{4.5}$$

with the charge $Z = 1$. Then, we vertically attach an electron to the solute $S^+$ restoring the neutral $S$ and releasing the binding energy $E_\mathrm{B}^{(\mathrm{liquid})}$. Finally, we take the solute out of the solution to complete the path. However, there is an important point to consider: in order for the cycle to close, the polarizable continuum can only be allowed to relax electronically during the vertical binding inside the solution. In turn, one has to accordingly modify Equation 4.5 only to reflect the high-frequency limit of the dielectric constant that controls electronic polarization

$$\Delta F_\mathrm{s} = -\frac{Z^2 e^2}{8\pi R}\left(1 - \frac{1}{\epsilon_\mathrm{el}}\right), \tag{4.6}$$

with

$$\epsilon_\mathrm{el} = n^2, \tag{4.7}$$

where $n$ is the refractive index. Another alternative point of view to illustrate this need is to take the two possible paths from gas-phase $S$ to solvated $S^+$ (either vertically ionizing in the gas phase and then solvating, or solvating first and then vertically ionizing in the liquid), which gives the same outcome if and only if solely the electronic relaxation of the solute is taken into account. With these considerations, the closed cycle is

$$-E_\mathrm{B}^{(\mathrm{liquid})} + \Delta F_\mathrm{s} + E_\mathrm{B}^{(\mathrm{gas})} = 0 \tag{4.8}$$

which is trivially rearranged to give the final expression

$$\Delta E_\mathrm{B} \equiv E_\mathrm{B}^{(\mathrm{liquid})} - E_\mathrm{B}^{(\mathrm{gas})} = -\Delta F_\mathrm{s}. \tag{4.9}$$

Therefore, in this model, the gas-to-liquid shift only depends on the radius $R$ of $S$ and the refractive index of the liquid. Since most liquids have refractive indices in the range 1.3–2.0, the gas-to-liquid shifts can generally be expected to be similar, even though the static dielectric constants $\epsilon_\mathrm{r}$ may vary greatly (some predicted and measured shifts are listed in Table 4.1). Note that the Born–Haber model generally accounts for most of the experimentally observed shifts; the only exception is benzene, where clearly the spherical approximation is far from reality. The agreement with the experiment is quite surprising once one considers the simplicity of the model, which cuts several important corners through neglecting other relevant contributions such as cavitation energies during solvation of the species, or the species' internal structure.

# 5 | $\pi$-hydrogen bonding in aqueous and ammoniacal environments

The findings of our work on the solvation structure of the ammoniated benzene radical anion and neutral benzene presented in the previous Chapter prompted us to investigate the phenomenon of $\pi$-hydrogen bonding in more detail. This resulted in Paper V (in the form of an `arXiv` preprint at the time of writing this thesis), listed as Reference 87 and reprinted in Appendix C.

## 5.1 | Paper V: Summary

In *"Elucidating the nature of $\pi$-hydrogen bonding in liquid water and ammonia"* (Paper V), we report the execution and analysis of classical and TRPMD simulations of neutral benzene dissolved in liquid water and liquid ammonia. The work aims to explore the phenomenon of $\pi$-hydrogen bonding in these two solvents concerning its structure, dynamics, and, notably, vibrational spectroscopy.

From the structural perspective, we find similar solvation motives in both solvents by inspecting the SDFs of the solvent heavy atoms and hydrogens around

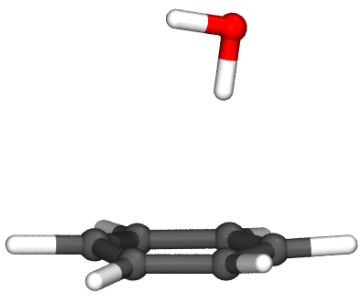

Figure 5.1: A simulation snapnshot showcasing a benzene molecule and a $\pi$-hydrogen solvent molecule (the rest of the periodic bulk solvent has been removed for visualization purposes.)

the benzene solute. This reveals the existence of the so-called $\pi$-hydrogen caps in the respective SDFs (Paper V, Figure 1), which point to a characteristic, oriented $\pi$-hydrogen bonding interaction. Further analysis of the possible orientations of the molecules occurring in the $\pi$-hydrogen caps (Paper V, Figure 2) suggests that while the nearly vertical configuration (*i.e.*, the one with the solvent molecule pointing its hydrogen atom towards the planar solute with the H–X $\cdots$ $C_6H_6$ angle not exceeding 40°) is the most common (Figure 5.1), the pool of available configurations is richer than that. Based on this knowledge, we set up a time-dependent existence criterion to judge whether a given solvent molecule (or, more precisely, a given replica of an imaginary time path-integral representation of a given solvent molecule in the TRPMD case) is $\pi$-hydrogen bonded. This is defined as

$$h(t) = \Theta\left[r_{\mathrm{X}}(t) - r_0\right] \Theta\left[z_{\mathrm{X}}(t) - z_0\right] \Theta\left[\theta_{\mathrm{X}}(t) - \theta_0\right], \tag{5.1}$$

where $r$ and $z$ are the cylindrical radial and vertical distance with respect to the plane of the benzene solute, $r_{\mathrm{X}}$ and $z_{\mathrm{X}}$ and the solvent heavy atom positions in this coordinate system and $\theta$ is the $\pi$-hydrogen bond angle, and $r_0$, $z_0$ and $\theta_0$ are fixed cutoff parameters (see Paper V for details); an example of this quantity is shown in Figure 3 of Paper V. Note that the definition in the above Equation serves an illustrative purpose; for the fully formal expressions, including all indices, refer to the text of Paper V. With access to these existence time series, we address the following questions.

First, we look into the cooperativity of $\pi$-hydrogen bonds since the benzene molecule simultaneously offers two binding sites for $\pi$-hydrogen bond formation (figuratively speaking, below and above the plane of the aromatic ring). We find that ammonia exhibits essentially no cooperativity effects, and the two binding sites behave independently. In contrast, water shows noticeable anticooperativity, where the formation of one $\pi$-hydrogen bond lowers the probability of the concurrent formation of a second one (Paper V, Figure 4): a gas-phase insight into this effect is presented and discussed in the following Section. Interestingly, we could not reproduce this effect with a C-NNP and we attribute this to the fact that the double-$\pi$-hydrogen bonded configuration extends beyond the standard 12 $a_0$ Behler–Parrinello cutoff, which renders the C-NNP insensitive to it. This affects not only the model itself but also the QbC-selected training set: this is a possible reason why we were not able to improve the description by switching to an equivariant NequIP model[197] (which is not limited by a hard cutoff value) trained on the same geometries. Additional research is needed to pinpoint the reasons for the observed behavior and potential improvements.

Second, we autocorrelate the time-dependent existence time series to obtain the so-called existence time-ACFs (Paper V, Figure 5), and then, using these, we estimate the lifetimes of $\pi$-hydrogen bonds in both solvents. We observe shorter lifetimes in water (1.8 ps) compared to the solvent–solvent hydrogen bond lifetime (3.9 ps) and comparable lifetimes in ammonia (1.7 ps vs. 1.4 ps, respectively for the $\pi$-hydrogen and solvent–solvent hydrogen bonds).

Finally, we model the VDOS and IR vibrational spectra of both studied systems and reproduce the experimentally observed phenomena discussed in Chapter 1. We find an imprint of the blue-shifted OH-stretch vibration due to the

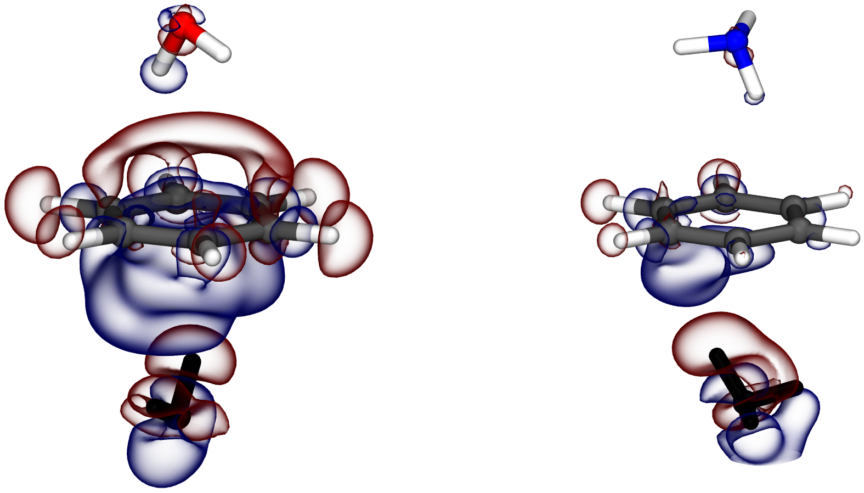

Figure 5.2: $\Delta\rho(\mathbf{r})$ plots for the optimized gas-phase clusters shown at the $\pm 3.5 \cdot 10^{-4}$ $a_0^{-3}$ contour (red for +, blue for −; see text for definition).

$\pi$-hydrogen bonded molecule in the water simulations. There is an equivalent effect in ammonia but without vibrational shifts: this behavior is fundamentally connected to the weak hydrogen bonding, which cannot soften the vibrations inside a solvent–solvent hydrogen bond as is the case in liquid water. To this end, we present the real part of the $\pi$-hydrogen bond resolved spectra obtained by correlating the simulated time-resolved vibrational spectra with the time series $h(t)$. The reasons why a non-trivial imaginary part of the time-resolved spectrum exists and a justification for why it does not need to concern us in this case are discussed below.

## 5.2 | Paper V: Discussion

### 5.2.1 Changes in electron density due to $\pi$-hydrogen bonding

To provide a degree of insight into the observed anticooperativity of $\pi$-hydrogen bonds in water, we resorted to a pair of auxiliary gas-phase calculations with the aim of qualitatively exploring the changes in electron density with $\pi$-hydrogen bonding. For this purpose, we optimized the geometries of the gas-phase double-occupied configurations (Figure 5.2) at the revPBE0-D3(BJ)/def2-TZVP [207,208] level of theory using the QChem software [209] and calculated the electron density of the optimized geometry $\rho(\mathbf{r})$. Then, we have vertically split the system into an isolated solvent molecule (Figure 5.2, black) and the remaining single-bonded configuration (Figure 5.2, usual color-coding by elements) and also calculated the electron densities of these fragments, say, $\rho_\mathrm{A}(\mathbf{r})$ and $\rho_\mathrm{B}(\mathbf{r})$, respectively. Finally, from these densities, we have calculated a difference density

$$\Delta\rho(\mathbf{r}) = [\rho_\mathrm{A}(\mathbf{r}) + \rho_\mathrm{B}(\mathbf{r})] - \rho(\mathbf{r}), \tag{5.2}$$

which shows the polarization of the system owing to the removal of one of the water molecules. The positive and negative contours at $\pm 3.5 \cdot 10^{-4}\ a_0^{-3}$ are shown in Figure 5.2 in red and blue, respectively.

In the case of water, the removal of the solvent molecule creates a pronounced effect where the electron density is strongly drawn to the side of the remaining solvent molecule, creating a large negative lobe at the side of the removed molecule and a large positive lobe at the other. This can be linked with the observed anticooperativity: as the density is depleted at the unoccupied side, the formation of the second $\pi$-hydrogen bond is correspondingly more difficult. In ammonia, the effect is much less pronounced already at the level of the gas phase. At the same isovalues, the positive lobe is essentially non-existent and the negative is considerably smaller in size in comparison to water. This is qualitatively consistent with the observed independence of the binding sites in ammonia. Additional effort would be necessary to perform a similar analysis on the fully condensed geometries.

### 5.2.2 The complex character of simulated time-resolved vibrational spectra

In the discussion revolving around vibrational analysis presented in Paper V, we have relied on correlating a time-dependent vibrational spectrum with the existence time series to isolate the vibrational spectrum of $\pi$-hydrogen bonded molecules. In the following paragraphs, we will conduct an extensive analysis of the way how time-dependent spectra are calculated and what potential complications such an analysis brings around. For this purpose, we will assume infinite continuous trajectories of observables to be able to discuss the matter using the methods of calculus.

To begin with, we remind ourselves that the VDOS is calculated using atomic velocities as

$$\begin{aligned} I_{\mathrm{VDOS}}(\omega) &= \sum_{i=1}^{N} \int_{-\infty}^{\infty} \mathrm{d}\tau\ e^{-\mathrm{i}\omega\tau} c_{vv,ii}(\tau), \\ c_{vv,ii}(\tau) &= \langle \mathbf{v}_i(t_0) \cdot \mathbf{v}_i(t_0+\tau) \rangle_{t_0}, \end{aligned} \tag{5.3}$$

where the index $i$ labels the atoms, and the IR intensity is calculated using molecular dipoles as

$$\begin{aligned} I_{\mathrm{IR}}(\omega) &= \omega^2 \sum_{i,j}^{N_{\mathrm{mol}}} \int_{-\infty}^{\infty} \mathrm{d}\tau\ e^{-\mathrm{i}\omega\tau} c_{\mu\mu,ij}(\tau), \\ c_{\mu\mu,ij}(\tau) &= \langle \boldsymbol{\mu}_i(t_0) \cdot \boldsymbol{\mu}_j(t_0+\tau) \rangle_{t_0}, \end{aligned} \tag{5.4}$$

where $i$ and $j$ labels the molecules. As the Fourier image[a] of a real even function is a real even function, it is clearly expected for both vibrational intensities to

[a]Here, we adhere to the tradition of using the symbol $\widehat{f}(\omega)$ to denote the Fourier image of the function $f(t)$ — this does not represent a quantum mechanical operator!

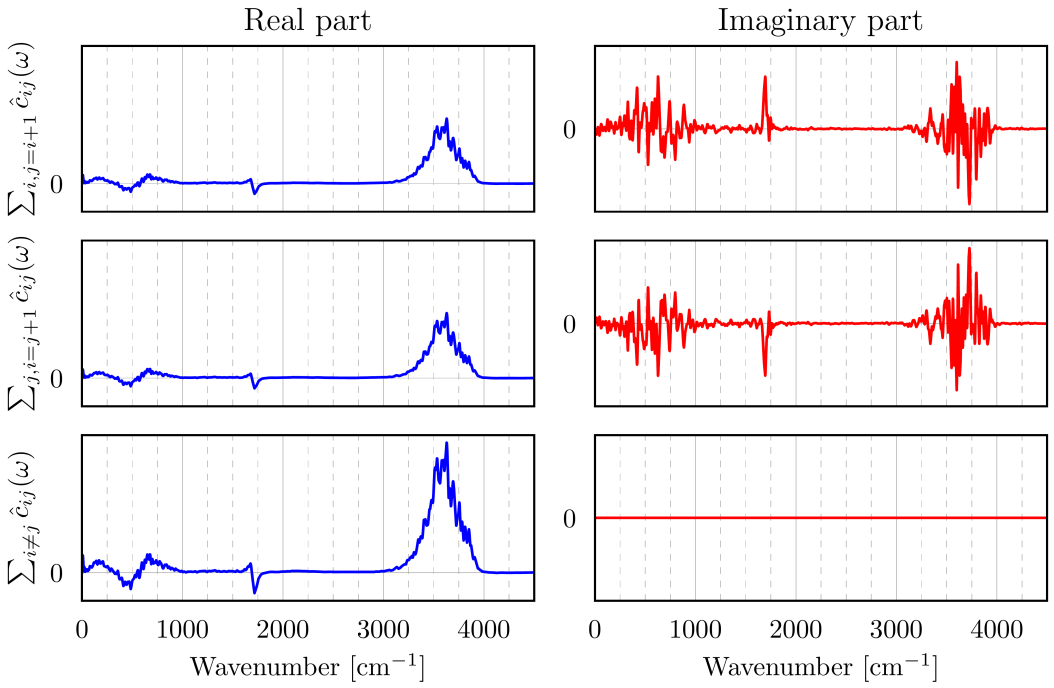


Figure 5.3: IR cross-terms obtained from an AIMD simulation of liquid water. Here, we illustrate the complex nature of the individual cross-terms. The top row shows the sum over half of the cross terms that comply with $j > i$ (*e.g.*, $\widehat{c}_{12}(\omega)$), which has a non-trivial imaginary part. The middle row than shows the sum over the complementary set ($j < i$, *e.g.*, $\widehat{c}_{21}(\omega)$), which also has a non-trivial imaginary part that is exactly the negative of the first one. The fact that they exactly cancel is shown in the bottom row which shows the sum over all molecular cross-terms — a purely real quantity.

be purely real quantities. For the VDOS, this is obvious as it only uses ACFs, which are real and even by definition (Equation 2.107). The same goes for the IR self-terms with $i = j$. A seeming complication arises for the cross-terms with $i \neq j$, as these are generally not even and, therefore, have a spectrum with a non-vanishing imaginary component. However, this can be disregarded for any practical purposes: thanks to the time reversal property of Equation 2.106, each $c_{ij}$ term is balanced out by a corresponding $c_{ji}$ term which together combine to an even function, too (this effect is shown in a realistic example of a liquid water AIMD simulation[4] in Figure 5.3). Another perspective on why the imaginary parts of molecular cross-terms have to cancel is obtained by considering that the contribution of all cross-terms combined can be alternatively obtained by subtracting the purely real self-term contribution from the also purely real total spectrum obtained as the autocorrelation of the total dipole. As both VDOS and IR share these same properties, we will use a general $A(t_0)$ notation for the time-dependent observables and keep in mind that these can represent either atomic velocities or molecular dipoles based on the immediate context.

The key quantity to the time-dependent vibrational spectrum is the time dependent ACF (which we can use instead of general CFs thanks to the argu-

mentation above)

$$c_{AA}(\tau, t_0) = A(t_0)A(t_0 + \tau) \tag{5.5}$$

for which clearly the full correlation function is recovered by integration

$$c_{AA}(\tau) = \int_{-\infty}^{\infty} \mathrm{d}t_0 \; c_{AA}(\tau, t_0), \tag{5.6}$$

*cf.* Equation 2.105. Some previous works relied on an approximate treatment, where not the raw ACF fragments $c_{AA}(\tau, t_0)$ were used for the calculation of the time-dependent spectrum, but each of these fragments was additionally autocorrelated with itself.[170] This results in a non-exact decomposition, but also in a mathematically simpler structure with purely real time-dependent spectra and works well for many practical purposes. Here, we aim to explore the possibility of an exact time decomposition of time-ACFs as defined in Equation 5.5. Due to the general nature of the functions $A(t_0)$, one cannot say anything about the symmetry properties of each contribution $c_{AA}(\tau, t_0)$, for instance, whether it is even. As a result, its Fourier transform, *i.e.*, the time-dependent spectrum, is a non-trivial complex-valued quantity. This is easily shown explicitly through

$$\begin{aligned}
\widehat{c}_{AA}(\omega, t_0) &= \int_{-\infty}^{\infty} \mathrm{d}t_0 \; e^{-\mathrm{i}\omega\tau} c_{AA}(\tau, t_0) \\
&= \int_{-\infty}^{\infty} \mathrm{d}t_0 \; e^{-\mathrm{i}\omega\tau} A(t_0)A(t_0 + \tau) \\
&= A(t_0)e^{\mathrm{i}\omega t_0} \int_{-\infty}^{\infty} \mathrm{d}t' \; e^{-\mathrm{i}\omega t'} A(t') \\
&= A(t_0)\widehat{A}(\omega)e^{\mathrm{i}\omega t_0} \; :
\end{aligned} \tag{5.7}$$

$\widehat{c}_{AA}(\omega, t_0)$ has an explicit complex phase factor and the Fourier image of the raw time series $\widehat{A}(\omega)$ is also generally complex-valued. As expected, this highly non-trivial nature vanishes upon integration over the time domain, which recovers the full, real spectrum:

$$\begin{aligned}
\widehat{c}_{AA}(\omega) &= \int_{-\infty}^{\infty} \mathrm{d}t_0 \; \widehat{c}_{AA}(\omega, t_0) \\
&= \widehat{A}(\omega) \int_{-\infty}^{\infty} \mathrm{d}t_0 \; A(t_0)e^{\mathrm{i}\omega t_0} \\
&= |\widehat{A}(\omega)|^2.
\end{aligned} \tag{5.8}$$

However, since Equation 5.8 holds, it must be true that the real part of $\widehat{c}_{AA}(\omega, t_0)$ integrates to the full spectrum

$$\int_{-\infty}^{\infty} \mathrm{d}t_0 \;\; \mathrm{Re}\, \widehat{c}_{AA}(\omega, t_0) = \widehat{c}_{AA}(\omega), \tag{5.9}$$

and, consequently,

$$\int_{-\infty}^{\infty} \mathrm{d}t_0 \;\; \mathrm{Im}\, \widehat{c}_{AA}(\omega, t_0) = 0. \tag{5.10}$$

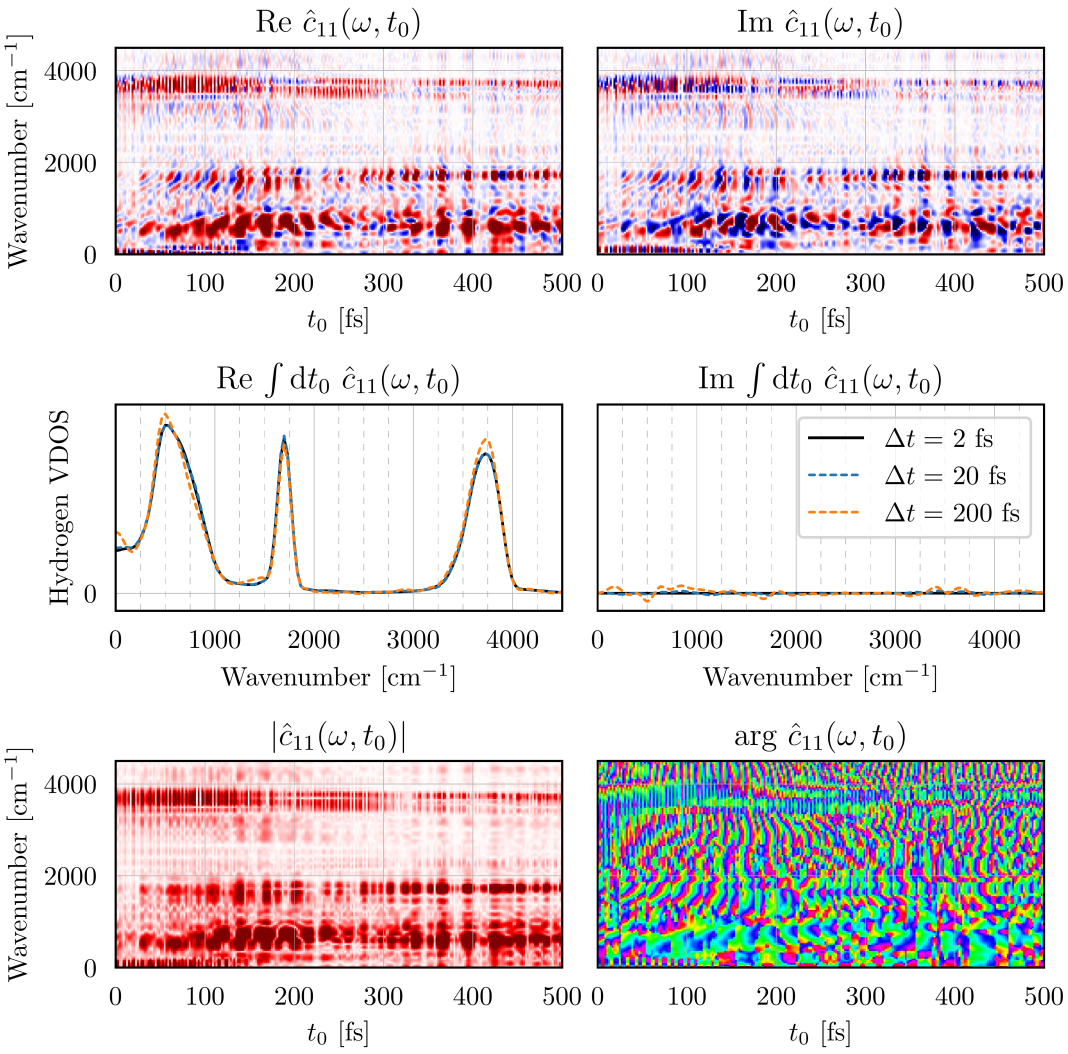


Figure 5.4: Time-dependent VDOS of a single-atom (indexed 1 in the employed topology of the system) velocity time series obtained from a classical AIMD liquid water simulation. The top row shows the real and imaginary part of the Fourier transform $\hat{c}_{11}(\omega, t_0)$ of the time-resolved ACF $c_{11}(\tau, t_0)$. The middle row then shows the integral of the data on both top panels over the time axis taken with three different strides through the data: the full resolution (2 fs) and then with data points spaced by 20 and 200 fs. The bottom row then shows the alternative representation of the same time-dependent spectrum, using the absolute value and the argument.

This causes a non-uniqueness in the choice of the "correct" time-dependent spectrum since multiple choices that share the same real part are possible. Apart from $\widehat{c}_{AA}(\omega, t_0)$, this is $\overline{\widehat{c}_{AA}(\omega, t_0)}$ and $\mathrm{Re}\,\widehat{c}_{AA}(\omega, t_0)$: all of these spectra are distinct, but all integrate to the same static spectrum.

This may represent a problem when correlating the spectrum essentially with any geometric property (*e.g.*, the existence $h(t)$ series in Paper V), as the result is a static spectrum with potentially non-vanishing imaginary components. We have tested this effect on the VDOS of neat liquid water, inspecting the velocity time

series of a single hydrogen atom (we use the employed topology index 1 to refer to it, but the specific choice is not critical as all the individual velocity time series behave identically from the viewpoint of this discussion). The obtained spectra (shown in Figure 5.4) are a testament to the analytical expressions derived above. The top row shows the complex nature of the time-dependent VDOS with both the real and the imaginary parts having a highly non-trivial character, exhibiting both positive and negative values. The validity of Equations 5.9 and 5.10 is demonstrated in the middle panel. An integration with the full resolution of the time-dependent data reconstructs the static VDOS through the real part and makes the imaginary part vanish nearly exactly (small fluctuations of the imaginary part, most likely an artifact of the finite data set size, the use of FFTs and apodization, are about 6 orders of magnitude smaller than the real part). Taking a stride through the data (which can mimic the correlation of the time-dependent spectrum with $h(t)$) reveals that Equations 5.9 and 5.10 remain approximately true: the imaginary part remains small in comparison to the real part. This is further supported by inspection of the argument of the spectrum, which shows a wildly oscillatory, quasi-random behavior, suggesting that integrating over a large number of data points will eventually make the phase vanish.

These considerations justify the use of only the real part of the spectra in Paper V as including the imaginary part only causes a small difference, especially when taking into account the fact that the $\pi$-hydrogen bond is featured prominently in $h(t)$ and thus a large number of data points is being used. However, the relevance and, perhaps more importantly, the meaning of the imaginary part could be explored in more detail. Finally, as a technical note, the form of the time-dependent spectrum given in Equation 5.7 implies that such spectra could be calculated in a more streamlined way, only needing a single Fourier transform of the raw time series and a trivial complex phase factor, rather than performing a Fourier transform at every point along the time axis.

# 6 | DABQDI in the gas phase and adsorbed on Au(111)

The final results-oriented Chapter focuses on the properties of the DABQDI molecule as an isolated entity and bound to the surface of gold and offers a compilation of various thus far unpublished results that we collected along the way.

## 6.1 | Insight from the gas phase

We will begin by discussing the results concerning DABQDI and some of its shorter chains in the gas phase mainly focusing on the proton-transfer reactivity. First, we will inspect the proton-sharing PESs of these systems and the corresponding MEPs, which makes it possible to discuss what reaction mechanisms are classically allowed. Then, at the level of the DABQDI monomer, we will introduce NQEs into the picture using instanton rate theory and discuss how quantum effects modify the possible reaction mechanism.

### 6.1.1 Classically allowed proton-sharing mechanisms

Concerted proton tunneling has been suggested as a suitable mechanism for the proton-transfer reaction in DABQDI chains on Au(111), as discussed in Chapter 1 and in Reference 93. Here, our aim is to explore whether concerted proton transfer can be already observed in simpler systems, *i.e.*, monomers or short chains in the gas phase, and if yes, whether it is a manifestation of NQEs as suggested by the interpretation of the experiment. The proton-sharing PES for the DABQDI monomer in terms of proton-sharing coordinates $\delta$ (return to Paper II, Figure 6 for definitions) was discussed in detail in Paper II as the molecule was used as one of the original examples to illustrate the TTS procedure. For convenience, identical data is shown also in Figure 6.1. It was obtained by performing a 2D relaxed scan with the values of the two proton-sharing coordinates fixed using custom constraints from the ASE library. The proton-sharing PES has a 4-minimum, 4-TS, and one-maximum structure: clearly this does not allow for a concerted proton transfer from the classical perspective, as the reaction MEP would lead through a higher-order saddle point (ca. 1.3 eV above the global basin that we set as the zero-energy reference), coinciding with the diagonal line $\delta_2 = \delta_1$. Rather, the actual MEP (calculated using the climbing-image NEB calculation [159,210] and

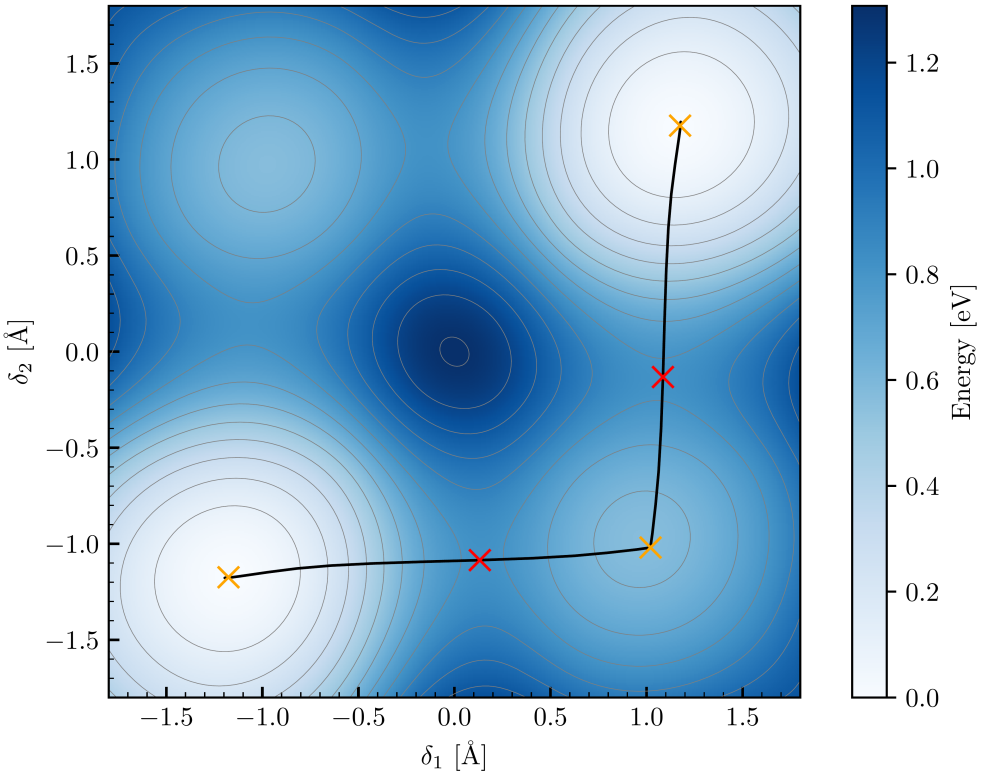


Figure 6.1: The PES of the DABQDI monomer shown as a function of two $\delta$-coordinates that describe the transfer of the individual exchangeable protons (blue). The classical MEP on this PES is shown as a black line. The important stationary points along this MEP are highlighted in orange (minima) and in red (TSs).

our C-NNP[46]) winds around the central barrier (Figure 6.1, black) through a lower-lying, first-order TS (ca. 0.8 eV above zero) and an off-diagonal minimum (ca. 0.6 eV above zero). As such, the classically allowed mechanism of the proton-sharing reaction is sequential, where one proton is transferred first (this corresponds to the "horizontal" part of the MEP where $\delta_1$ changes while $\delta_2$ stays almost constant) and the other proton follows after the first one (this corresponds to the remaining "vertical" segment).

For the dimer and the trimer, one cannot straightforwardly visualize the multidimensional PES in all the relevant $\delta$-coordinates as was done for the monomer, but the energy dependence along the MEP can be inspected with ease. It was found that a qualitatively identical discussion arises for the dimer and the trimer and, therefore, the results only for the trimer are presented in Figure 6.2 to illustrate the general rule. Just like the monomer, the trimer exhibits a MEP that corresponds to a fully sequential proton transfer. The direction and order of the proton-transferring steps of the whole reaction are illustrated on the snapshot in Figure 6.2 by arrows and numbers. The reaction starts from the global minimum at $\xi = 0$ by transferring one of the outer protons at the edge of the chain (step 1). This creates a potential energy minimum structure, which is defective in the sense that no Lewis structure can be produced. The initial proton transfer is

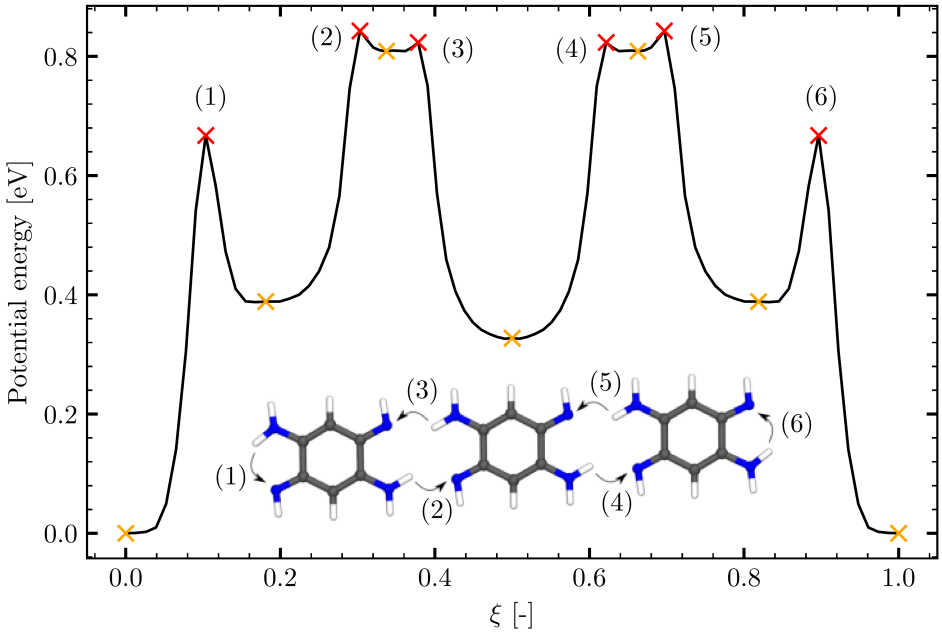


Figure 6.2: The MEP of the complete proton-transfer in the gas-phase DABQDI trimer. The dependence of the potential energy on the dimensionless reaction coordinate $\xi$ is shown in black, with the corresponding minima in highlighted in orange and the TSs in red. The bracketed numbers pertain to the order of the steps of the sequential proton transfer: each transfer of an individual proton as numbered on the snapshot of the chain corresponds to a peak on the MEP with the same number. The presented curves were obtained at the revPBE0-D3/TZV2P level of theory.

followed by the transfer of the pair of adjacent inner protons (steps 2 and 3), that is predicted at the employed revPBE0-D3/TZV2P level of theory to happen also sequentially, albeit through a very subtle minimum. As such, the possibility that this is an artifact of the chosen DFT method cannot be excluded and one has to consider an alternative picture where steps 2 and 3 happen in a concerted fashion (we note in passing that such a two-proton concerted mechanism was observed, for example, in the acetic acid dimer[211]). Then, the same happens for the other pair of inner protons (steps 5 and 6), and the reaction path is closed by the exchange of the final outer proton, ending in the second global minimum. Therefore, a general trend can be devised: the classical MEP always starts with the exchange of one of the edge protons, which creates a defect that is propagated through the chain consecutively from one molecule to another and finally quenched by closing the sequence by the second outer proton. From this perspective, the monomer can be understood as a chain consisting of a single unit. The consideration of gas-phase chains with >3 units is mostly hypothetical as the structures tend to twist upon geometry optimization; in principle, the presence of an inert surface sanitizes this behavior, as seen in the STM/AFM experiments.[93] The conclusion of the above calculations is that the proton-sharing PESs of the gas-phase DABQDI chain do not permit classical concerted proton transfer as

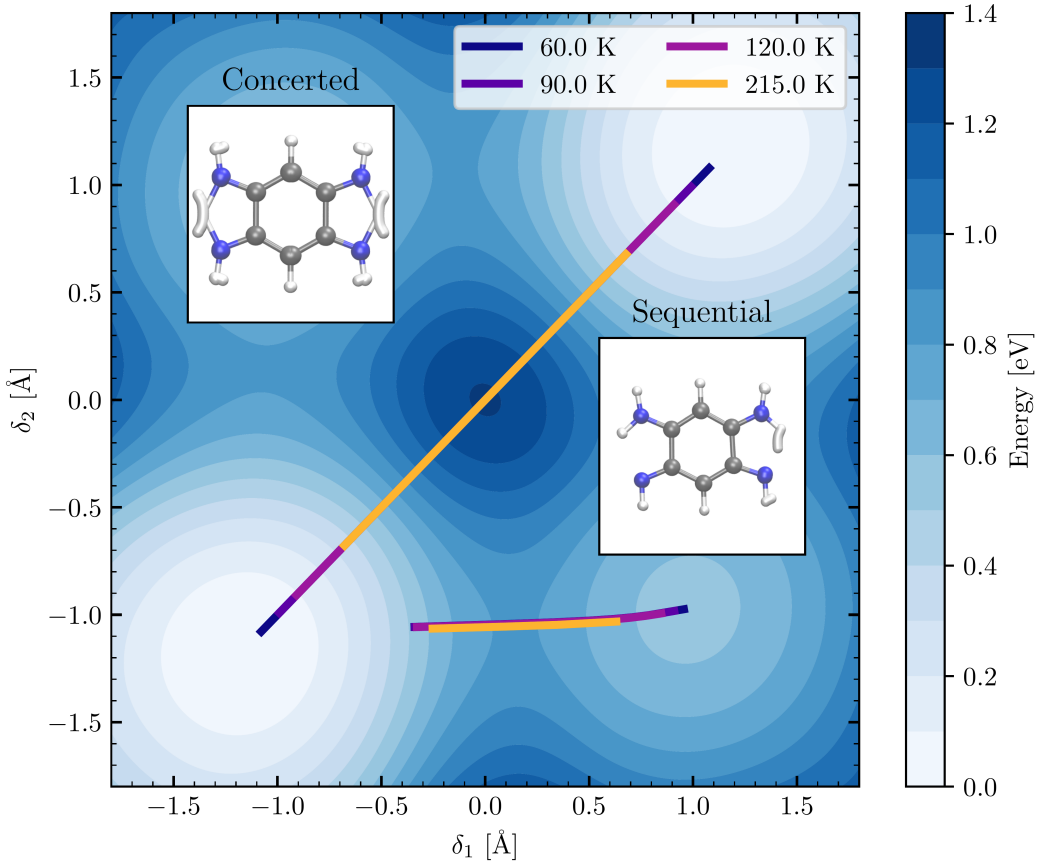


Figure 6.3: Calculated ring-polymer instanton paths of the DABQDI monomer at different temperatures projected onto the $(\delta_1, \delta_2)$-PES. Two different types of instantons can be seen which correspond to the two types of proton-transfer mechanisms: sequential and concerted. A depiction of the instanton path going through the fully dimensional configuration space is presented in the two inset snapshots.

this process is connected with high barriers.

### 6.1.2 Quantum effects on the proton-sharing reaction

The appropriate question at this point is what happens quantum-mechanically when tunneling through the central barrier is allowed. In this thesis, this problem is addressed at the level of the gas-phase monomer using ring-polymer instanton theory; instanton calculations for the trimer in the gas phase were unsuccessful due to twisting of the chain geometry when optimized and the workflow for obtaining surface-bound C-NNPs is a matter of ongoing research.

The instanton paths for the isolated DABQDI monomer, optimized using the C-NNP obtained in Paper II in tandem with the i-PI program using 1024 full-ring replicas, are shown in Figure 6.3 for three different temperatures. Below the crossover temperature for this system of $T_c = 284$ K, we find two types of stable instantons for this molecule that correspond to the concerted and sequential reaction mechanisms. The sequential one derives from the classical TS (*cf.* Fig-

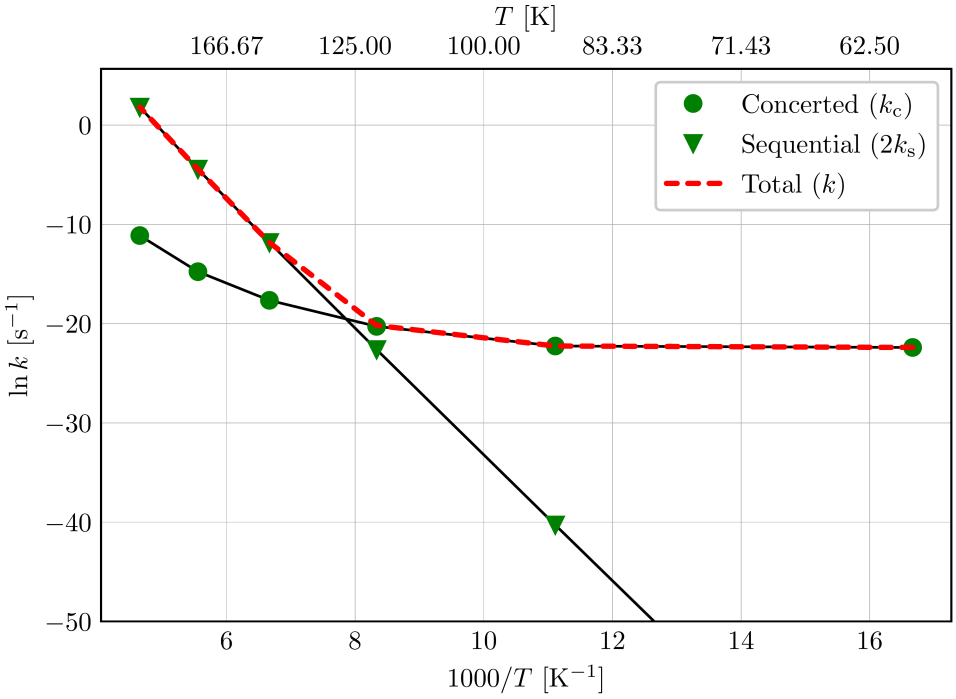


Figure 6.4: The temperature dependence of the sequential, concerted and total proton transfer reaction rates in the isolated DABQDI monomer. The sequential rates have been multiplied by 2 to account for the presence of two alternative sequential tunneling paths.

ure 6.1) and represents quantum proton tunneling between the global basin and the higher-lying minimum of the defective structure, with only one proton being exchanged at a time (Figure 6.3, bottom right snapshot). A typical temperature dependence is observed: as the system is cooled down, the instanton paths grows longer as quantum effects become more pronounced. As a new feature that was established as classically disallowed and therefore has no parallel in Figure 6.1, we find stable instantons for the concerted proton transfer once tunneling is accounted for by the instanton theory. These lie on the main diagonal $\delta_2 = \delta_1$ and thus represent tunneling from one of the global minima to the other where both protons are exchanged at the same time (Figure 6.3, top left snapshot). The existence of both instanton paths tells us that the tunneling of the quantum system happens through both of the two corresponding mechanistic channels.

The question of which of the channels is dominant at which temperature is not answerable simply from the knowledge of the paths, and their rates must be calculated. These are shown in Figure 6.4. The total tunneling rate is given by the sum

$$k = k_c + 2k_s, \tag{6.1}$$

where $k_c$ is the rate constant evaluated for the concerted instanton trajectory and, accordingly, $k_s$ is the rate constant of the sequential reaction. The factor of 2 accounts for the fact that two distinct sequential paths are possible which correspond to the order of the proton tunneling. At high temperatures above 160 K,

where the system is expected to behave more classically, the sequential rate is clearly the dominant pathway, with the concerted tunneling only as a negligible contribution. As the temperature is lowered, the two curves come closer together until they finally intersect at approximately 130 K, and the concerted proton tunneling starts to take over. At low temperatures, the concerted mechanism clearly dominates as the concerted rate exhibits a plateau, while the sequential rate keeps exponentially decreasing: this behavior can be tracked to the magnitude of the difference between the energy of the zero-point energies of the reactants and the products in each mechanistic step.[180] Finally, we note that one should focus more on the trends predicted by instanton theory and take the absolute values of instanton tunneling rates with a grain of salt unless extremely accurate electronic structure methods (such as, for example, coupled cluster theory[106]) are employed. This is due to the exponential dependence of the rate on the action of the instanton path, which itself directly depends on the shape of the underlying PES, including both the barrier height and its curvature: relatively small errors in both can cause several orders of magnitude of difference in the estimated rate.

## 6.2 | Surface-bound systems

The emergence of concerted proton tunneling at low temperatures in the gas-phase monomer supports the interpretation of the initial experiment as a concerted tunneling of protons in the surface-bound chains, albeit it does not represent a complete computational proof. The fact that this temperature-dependent effect occurs already in the gas phase suggests that the surface does not strongly interact with the deposited molecules (weak surface–substrate interaction is also initially suggested by experimental evidence) rather than being a key element in the sense that it would change the prevalent proton-sharing mechanism through a strong and non-trivial interaction. In the following Section, we address some of the properties of the DABQDI monomer and dimer bound to the gold surface regarding molecular geometry and the strength of the molecule–surface interaction.

### 6.2.1 Optimized geometries

Using the FHI-aims software,[140] we first optimized the lattice parameters of bulk gold for the chosen MBD-corrected PBE density functional and the "light" defaults. This was achieved by performing a fixed-angle cell optimization of the fully periodic face-centered cubic one-atom bulk while monitoring the **k**-point convergence of the lattice parameters. Scalar zeroth-order regular approximation[212] was employed to address relativistic effects and the optimal lattice constant was found to be 4.132 Å. With the optimized cell parameters, we proceeded by building the (111) surface slab ($4 \times 3 \times 4$ atoms) using ASE tools and centering the DABQDI monomer over the slab. The geometry of such a system was then optimized using the BFGS optimizer[183–186] with a maximum force component threshold of $5 \cdot 10^{-3}$ eV Å$^{-1}$. For the optimization, we have employed full PBCs with a 50 Å

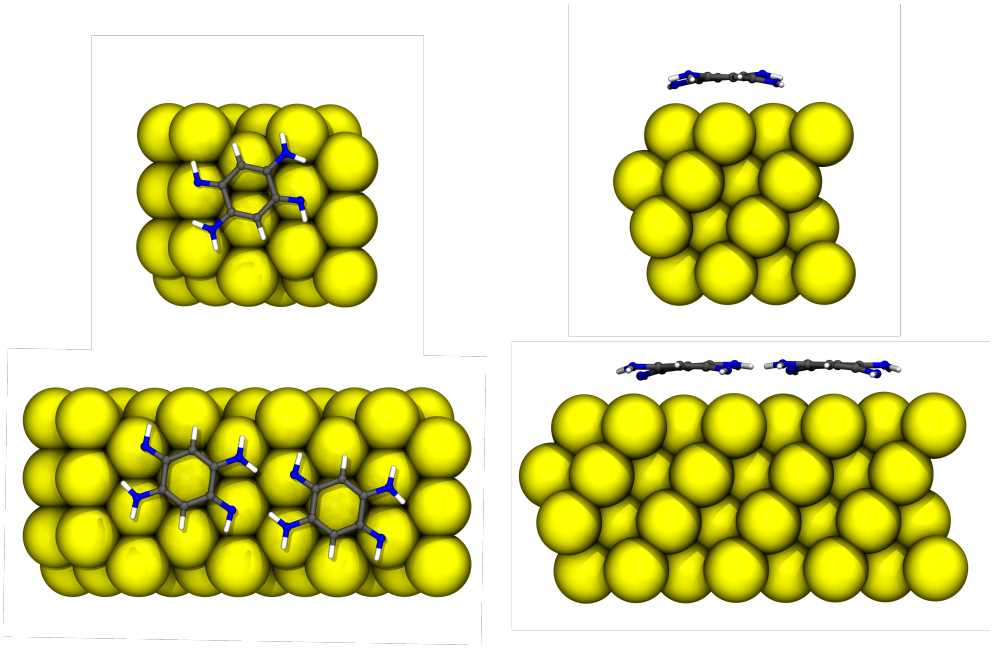

Figure 6.5: Optimized DABQDI monomer (top row) and dimer (bottom row) geometries on Au(111) (yellow) viewed from the top and the side. The slab is described using PBCs.

vacuum in the $z$-direction and a $4 \times 5 \times 1$ Γ-centered **k**-point grid; a validation of these choices was performed. A dipole correction was employed.[141] For the surface-bound dimer an essentially identical approach was taken, just using a larger slab of $8 \times 3 \times 4$ atoms and a smaller $2 \times 5 \times 1$ Γ-centered **k**-point grid.

The obtained optimized geometries are shown in Figure 6.5. In general, the molecular geometry of DABQDI compares well with the one in the gas phase in terms of intramolecular structure of the monomers and the spacing of the chain units in the dimer. In both systems, the side view reveals a twist of the molecular geometry where the imine nitrogen atoms are brought closer to the surface, distorting the planarity of the molecule. The twist persists after a reoptimization with the hybrid HSE06 density functional[118] and "medium" defaults. The dimer geometry shows that the twist is stronger at the non-hydrogen-bonded imine groups at the ends of the chain, implying that a competition between the hydrogen bonding within the chain and the molecule-surface interaction is taking place. The presence of the twist is in contrast with the original supporting calculations in Reference 93, which report fully planar surface-bound monomers. Comparing the monomer and dimer suggests the possibility of several different unique equilibrium positions on the surface: the monomer has the center of the carbon ring positioned at the bridge between two gold atoms, whereas the dimer has the centers over gold atoms. A relaxed lateral scan of the DABQDI position with respect to the slab will be needed to provide a conclusive answer on the locations and energetics of equilibrium surface-bound positions. Finally, a curious fact to notice about the surface-bound dimer is that the spacing of the monomer units (7.72 Å for imine groups, 7.76 Å for amines) nearly exactly coincides with the naturally occurring spacing of gold atoms within the metal lattice in one particular direction (7.71 Å). This is not a surface-mediated effect, *i.e.*, the binding to

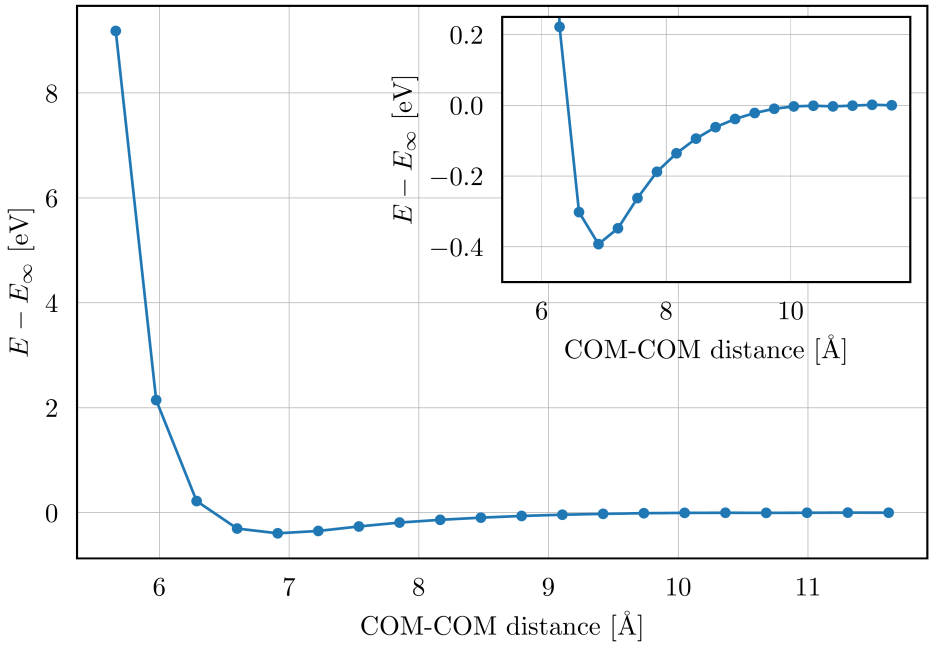


Figure 6.6: The binding curve of the DABQDI monomer to the Au(111) slab, calculated vertically in the geometric coordinate defined by the slab and monomer center-of-mass (COM) distance. The inset shows a detail on the binding energy minimum.

the surface does not alter the unit spacing to comply with the surface geometry, but rather a preexisting geometric property of the DABQDI dimer already at the gas-phase level. It points to a relevant question of whether this surprising agreement of spacings makes the Au(111) surface special for binding the DABQDI chains. As of now, we tend to believe, also based on the results summarized in the following Section, that this is merely a coincidence that will not have further consequences for the physics and chemistry of the studied systems.

### 6.2.2 Molecule–surface interaction

The original paper[93] speculates on the basis of several plausibility arguments that the molecule-surface dispersive interaction is not strong in the DABQDI/Au(111) systems, including the fact that the chains are oriented irrespective of the herringbone reconstruction of the experimental surface. To get insight into the magnitude of the DABQDI–surface interactions, we performed two different calculations on the surface-bound monomer.

In the first analysis, we predicted the binding energy curve of the monomer to the surface (Figure 6.6). This was calculated by a gradual vertical removal of the molecule from the slab, *i.e.*, starting from the bound minimum geometry and only changing the distance between the center of mass of the slab and of the molecule without any geometry relaxation. The curve adopts a typical shape consisting of a repulsive part at close distances and an attractive part at longer

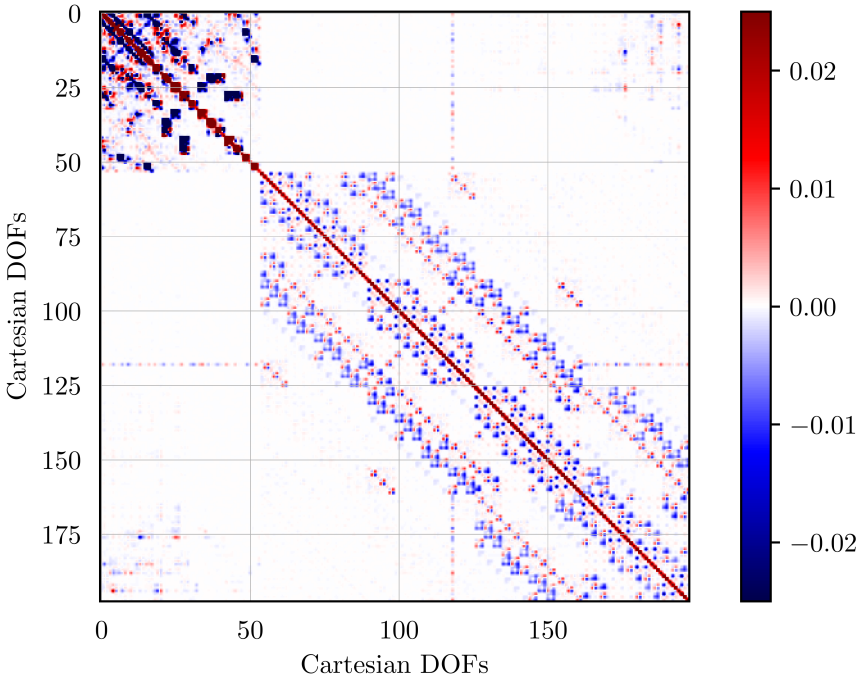


Figure 6.7: The full Hessian matrix of the DABQDI monomer/Au(111) system in Cartesian coordinates. Degrees of freedom 0–53 correspond to the motion of monomer atoms, the remaining 144 degrees of freedom to the gold slab.

distances; the optimized minimum lies approximately 0.4 eV under the $E_\infty$ value, which is understood here as the energies of the isolated slab and monomer combined and used as the zero-energy level. Such values are consistent with binding energies corresponding to the physisorption of other small molecules on metal surfaces, including Au(111). For example, it is more than values up to 0.1 eV for benzene[213] (depending on the specific configuration), and comparable to pyridine at 0.36 eV.[214] This suggests, consistently with the small change in molecular geometry upon absorption, that no chemically significant changes take place in the DABQDI molecule and, while it is important to take the explicit surface into consideration for an accurate overall picture, one can get a fairly good idea about the character of the absorption using, *e.g.*, an empirical van-der-Waals representation of the surface (as was done in Reference 93).

The second analysis focuses on the coupling of the vibrations between the molecule and the surface. For this purpose, we calculated the Hessian matrix for the whole DABQDI monomer/Au(111) system using the i-PI software with FHI-aims forces. The calculated Hessian is shown in Figure 6.7 as a visual representation of the matrix, showing the magnitude of the $\partial^2 E_0/\partial R_{I,\alpha}\partial R_{J,\beta}$ elements (with $R_{I,\alpha}$ being the Cartesian components of the atomic position vector $\mathbf{R}_I$) using a color map. As expected, the Hessian is a symmetric matrix and can be divided into 4 distinct blocks. The first square diagonal block corresponds to the DABQDI degrees of freedom (0–53) and has a non-trivial internal structure. The remaining block on the main diagonal (54–198) corresponds to the vibrations of

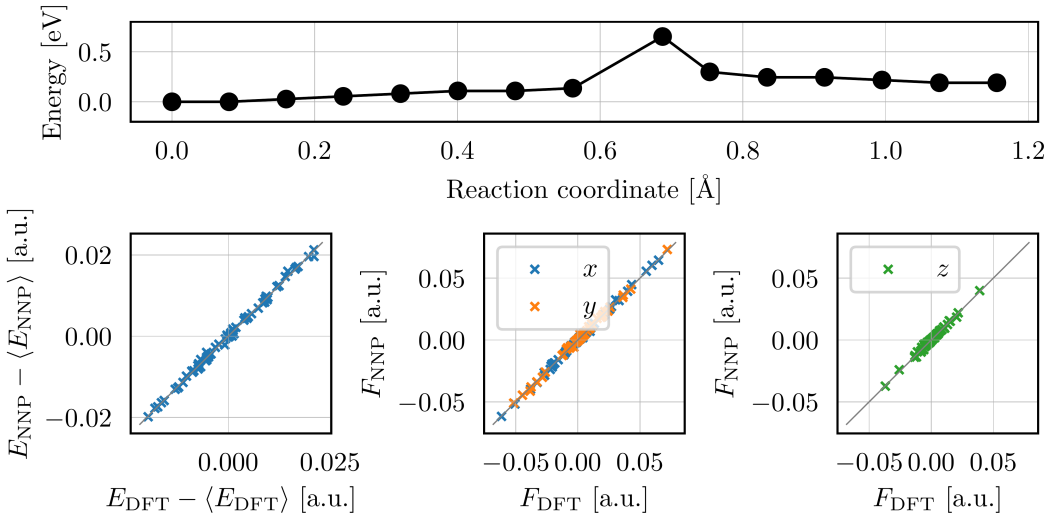


Figure 6.8: Characterization of the surface-bound DABQDI proton-sharing MEP and the validation of the resulting C-NNP model. Top panel: the energy dependence of the calculated MEP as a function of the distance along the path. Left bottom panel: correlation of energies between DFT and the obtained C-NNP. The mean of the energies evaluated by each method was subtracted from the respective values to remove a constant arbitrary shift between the *ab initio* method and the C-NNP model. Middle bottom panel: Correlation of force components DFT and the obtained C-NNP in the direction parallel to the gold slab ($x$ and $y$). Right bottom panel: Correlation of force components for the direction perpendicular to the metal slab ($z$).

the metal slab. The numbering of the Cartesian degrees of freedom inside the slab is as follows: 54–89 correspond to the bottom layer of the slab, 90–125 and 126–161 the middle layers and 162–197 to the top layer directly underneath the adsorbed molecule. From the graphical representation of the Hessian, we find that the vibrational coupling inside the slab is the strongest within a given layer and that the inter-layer coupling is generally much weaker. Importantly, the remaining off-diagonal rectangular blocks correspond to the molecule–surface vibrational coupling, which is essentially non-existent between the molecule and the distant layers and small between the molecule and the top layer. The single interacting gold atom corresponding to a position in the middle of the slab ($\sim 120^{\mathrm{th}}$ coordinate) is curious and remains unexplained; possibly, this is an artifact due to the finite precision of the numerical evaluation of the PES derivatives. Diagonalization of the DABQDI block from this matrix and diagonalization of the same block calculated with the surface frozen reveals essentially identical vibrational frequencies of the DABQDI molecule, further suggesting that the vibrational coupling is very weak. As such, one can make a reasonable approximation by keeping the surface frozen, as this can be expected to only have a small effect on the motion of the molecule.

### 6.2.3 Towards a surface-bound C-NNP

The above analysis gives us a level of understanding of the interaction of the absorbed DABQDI molecule and the gold surface. Ideally, one would consider a fully flexible surface that explicitly enters the electronic structure calculation to obtain the most accurate possible description with a given *ab initio* PES, but this makes the desired AIMD simulations quite computationally challenging already in the instance of the surface-adsorbed monomer treated at the GGA level of DFT as the proton-transfer reaction must be described at the *ab initio* level. Therefore, we initiated our efforts to obtain a C-NNP model for this system by invoking a TTS-like sampling with the surface included. Clearly, as a standalone method outside of the gas phase, TTS has limitations that were discussed in detail in Chapter 3: here, these pertain mainly to the surface diffusion of the molecule that is outside of the scope of a description offered by a single MEP. However, invoking TTS can give rise to a first-generation model that can be further improved by the aforementioned methods; here, we take an exploratory stance and attempt to create a very preliminary model with the aim of mapping whether these goals are possible at all.

To begin, we have optimized the two endpoint configurations on Au(111): these correspond to one branch of the reaction MEP shown in Figure 6.1 for the gas-phase molecule (*i.e.*, a transfer of a single hydrogen). Then, we optimized an MEP connecting these configurations to obtain the TS geometry. This was achieved using the climbing image NEB implementation within the i-PI software and relying on FHI-aims forces, consistently staying at the PBE-MBD level of theory. The resulting energy dependence of the MEP of the surface-bound system is shown in the top panel of Figure 6.8. It shows certain deviations from the gas phase MEP. First, the calculated reaction path now contains only slowly changing, almost plateau-like regions (ca. 0.0 – 0.5 Å and 0.8 – 1.1 Å) that correspond to a molecular reorientation against the surface with no intramolecular rearrangement (rotation–translation) taking place. This takes place rather abruptly (0.5 – 0.8 Å) with a pronounced change in energy and a TS located approximately 0.7 eV above the reactant minimum. In addition, it appears that the presence of the surface stabilizes the defective minimum by approximately 0.3 eV compared to the gas phase. A potential shortcoming of this MEP can be glimpsed straight away: the i-PI implementation appears to enforce equidistance of the NEB replicas, which causes the replicas to cluster into either side of the $\delta$ coordinate as a simple rotation–translation of the DABQDI molecule against the surface takes place (where many atoms move just slightly) and the reaction itself (where effectively only the hydrogen is moving) is not sufficiently resolved. To combat this effect, either a refinement of the NEB in the reactive region, or a change of implementation to one that does not have this constraint, will be needed.

Disregarding the numerical qualities of the obtained MEP for the time being, we proceeded to perform a TTS sampling of it. As per usual, we have calculated the Hessians of the two minima and the TS (while invoking the frozen-surface approximation to make these exploratory-level calculations a little less computationally challenging) and used the obtained modes to generate distorted

geometries through the standard procedure described in Paper II. Taking these as the candidate set, we proceeded to perform a QbC, yielding a total of 220 training structures, and training a standard C-NNP model. We first validated the resulting model by correlating the predicted energies and forces for a selected handful of geometries from the TTS ensemble against the target energies and forces evaluated by the original *ab initio* method (Figure 6.8, bottom row). This shows very promising results, pointing to the fact that the C-NNP reliably reproduces the PES within the set of candidate geometries. A more stringent test is the capability of the model to run MD. Here, the answer is slightly less unequivocally positive as we have seen both stable and unstable trajectories starting from different candidate geometries at canonical conditions and the temperature of 100 K. Typically, we observed stable trajectories starting from configurations close to the minima, whereas trajectories starting from around the TS exhibited more instabilities. We attribute this behavior to the insufficient resolution of the actual reaction by the optimized MEP: as the proton transfer is essentially described by 3 points on the MEP, there is no guarantee that the generated TTS geometries copy the actual reaction valley in the configuration space rather than cutting a corner. In turn, that would lead to an insufficient coverage of the MD-relevant PES and the observed extrapolation failures. To this end, we will need to benchmark other NEB implementations and explore the possibilities of densifying the replicas in the reactive section of the MEP, as this problem is pertinent to all surface-bound hydrogen transfers. Another obvious shortcoming of the presented procedure is the number of training structures which will very likely need to be raised to reach the stability and accuracy levels we have learned to expect from C-NNPs. However, these are practical limitations and the above correlations suggest that improving them will improve the model accordingly. These results thus serve as a proof of principle that a TTS-based sampling approach will be instrumental in a computationally affordable training of reactive machine-learning potentials for surface-bound systems. Making this approach robust and reliable will be the objective of our immediate research efforts.

# 7 | Conclusions and outlooks

AIMD simulations of condensed and surface-bound systems with explicit treatment of the quantum nature of nuclei through path integrals in imaginary time can be very insightful, but also represent a major methodological and computational challenge. In this thesis, we have contributed to new developments in the integration of MLPs into the world of molecular simulations by introducing and testing a QbC workflow for efficient C-NNPs as well as the TTS method for gas-phase reactive models. Furthermore, we have employed (*ab initio* as well as MLP-enhanced) AIMD simulations to study three different types of molecular systems: the benzene radical anion dissolved in liquid ammonia, neutral benzene in water and ammonia, and DABQDI molecules in the gas phase and on a gold surface. The discussed research was published in 4 peer-reviewed publications and one preprint attached to this thesis, as well as in several additional publications. The common theme of hydrogen bonding that connects the individual research projects was manifested in different ways: for the benzene radical anion, it played a role in the structure of the stabilizing solvent environment; for the DABQDI-containing systems, it was a centerpiece of the research focus and in the $\pi$-hydrogen bonding perhaps a combination of both.

From the methodological perspective, our tests and validation of the committee approach to NNPs points to undoubted advantages over using individual NNPs regarding accuracy and robustness. Combined with its low computational overhead and the possibility of active learning, it seems that C-NNP indeed represents a superior approach. Further research efforts will exploit model bootstrapping to achieve highly advanced levels of electronic structure theory for MD simulations. In parallel, we have proposed the TTS method to obtain C-NNPs for gas-phase reactions efficiently. The method was shown to perform excellently for the chosen examples. The next immediate step is to include the ideas behind TTS into a wider workflow to enable reactive simulations in more complex settings than the gas phase, notably focusing on solid interfaces and the condensed phase, where the "standard" AIMD-based approach (as described in Paper I) is hardly applicable due to its inherently high computational cost.

The carefully benchmarked open-shell, hybrid-DFT simulations of solvated benzene radical anion chronologically fall before the introduction of MLPs into our routine workflow, hence the explicit *ab initio* PES. These simulations let us observe several intriguing properties of the solute, including its complex electronic structure and the dynamic Jahn–Teller effect, its electronic stabilization by the liquid environment, and its solvation structure. Alongside the value of these results and the subsequent discussion from the perspective of quantum physics

and chemistry, as well as their role as a testament to the need for advanced electronic structure methods to achieve descriptive accuracy, these simulations point to an interesting fact that the representation of reaction mechanisms in organic chemistry is often very simplified. While our work here does not report a simulation of the whole mechanistic sequence of the Birch reduction from benzene all the way down to cyclohexadiene, but rather a simulation of a single intermediate within this mechanism, we can already see at this instance that the highly non-trivial and dynamic distribution of the excess electron in the benzene radical anion is in contrast with the traditional representation using a fully localized "dot" on one of the carbon atoms. Organic mechanisms, built on a set of empirical rules and chemical intuition, have undeniably succeeded in interpreting and predicting the course of various reactions. However, our observations raise the question of whether such a simplified view can lead to an erroneous understanding of the underlying reactivity in certain cases. Experimental validation of mechanisms normally relies on spectroscopic evidence of the short-lived intermediates and often represents a complicated process, if possible at all. In this light, AIMD simulations, especially enhanced by effective MLPs, can provide rigorous, insightful, and relatively easily accessible complementary evidence that includes thermal effects (unlike simpler quantum chemistry calculations). We should expect to see more MD-based insights in the field of organic chemistry as accurate simulations (and the corresponding infrastructure around them) become more and more accessible to non-expert users.

In the part focused on $\pi$-hydrogen bonds, we have performed a thorough investigation of the structure, dynamics, and vibrational spectroscopy of $\pi$-hydrogen bonds in solutions of benzene in liquid water and ammonia. This was motivated by our own previous results, as well as Raman spectroscopy experimental evidence.[80] We find that $\pi$-hydrogen bonds are a prominent structural motif in our simulations and, therefore, it is important to take care of their description in empirical force fields due to their relevance in the solvation of biological systems; currently available force fields have been shown to perform insufficiently for this purpose.[84] Our exploration of $\pi$-hydrogen bonding in the two solvents also serves as a probe of the differences between the character of hydrogen bonding in liquid water and ammonia themselves. As a particular manifestation, in our benzene–water simulations, we observed a reasonable degree of anticooperativity between the two binding sites of benzene, while in ammonia, the sites behave effectively independently. Interestingly, we could not reproduce this effect faithfully using MLPs. We have identified a possible cause of this effect due to the cutoff-related limitations of standard Behler–Parrinello NNPs, but more research will be necessary to fully grasp why precisely this particular system is a challenge and what the possible solutions are. MLPs are clearly not omnipotent, and showing their shortcomings and, more importantly, how to deal with these shortcomings, allows for a deeper understanding of these potentials and gives one finer control over their performance.

In the last application part of this thesis, we have focused on the hydrogen bonding of DABQDI molecules, intending to understand and theoretically corroborate experimental AFM findings presented in Reference93. Specifically, we

were looking for evidence of concerted proton transfer, which is required to explain the experimental findings. Using ring polymer instanton theory, we have clearly demonstrated the emergence and dominance of concerted proton transfer in the isolated DABQDI monomer at low temperatures. Our additional findings make it seem very plausible that concerted proton transfer will also be the dominant proton-sharing mechanism in the longer, surface-bound chains. However, this remains to be shown explicitly using highly accurate, reactive NNPs for the surface-bound systems. As mentioned above, obtaining such potentials will require additional method development and further research to optimize the workflow to generalize the TTS method beyond the gas phase.

The simulations presented in this thesis can be understood as an illustration of the progress that computational methodology has undergone in the past years: hybrid DFT, not so long ago reserved only for electronic structure calculations of small gas-phase systems, has been employed here to drive AIMD simulations of bulk liquid solutions on a routine basis. This is possible through rapid advances in hardware and availability of efficient computational methodology electronic structure codes. However, arguably even more stunning is the speedup offered by MLPs, where one can expedite the practical simulation runtime by many orders of magnitude in comparison to the naive *ab initio* execution, especially for computationally demanding methods like hybrid DFT and higher up the DFT Jacob's ladder. Does this imply that machine learning is the future of molecular simulations and explicit *ab initio* simulation of MD will soon be surpassed? This is probably true in a certain sense and we will gradually see more works depart from explicit quantum electronic structure PESs and rely to a larger extent on MLPs (and other machine learning tricks) to accelerate the desired calculations. For now, an AIMD expert is, at least to some degree, a specialist in multiple fields, including quantum electronic structure, statistical mechanics, and computational science. Even with the current state of the art, *ab initio* reference evaluations are still an integral part of the process, even though the production simulation is realized without them, and one has to remain in control of both aspects to deliver a successful simulation. However, with the advent of, for instance, large universal models, it can soon become a reality that one will be able to run *ab initio*-quality simulations just by using appropriate MLPs off the shelf, without needing to run any *ab initio* reference calculations at all. As such, we will likely witness a more pronounced split of the expertise of scientists engaging in AIMD simulations into one direction focusing on the development of potentials and another focusing on executing the simulations (as seen in the force field community); time and experience will show what advantages and disadvantages this effect might bring around. In any case, machine learning will keep us approaching new horizons in the field of molecular simulations by allowing us to simulate molecular systems at unprecedented time and length scales with unprecedented levels of PES theory, bringing us closer to the holy grail of simulating macroscopically relevant systems with quantum-mechanically accurate interactions and converged NQEs.

# References


[1] Arunan, E., Desiraju, G. R., Klein, R. A. et al.: Definition of the hydrogen bond (IUPAC recommendations 2011), *Pure and Applied Chemistry*, 83, 8, 1637–1641, 2011.

[2] Atkins, P. and Friedman, R.: Molecular Quantum Mechanics, Oxford University Press, New York, New York, fourth edition, 2005.

[3] Morawietz, T., Singraber, A., Dellago, C. and Behler, J.: How van der waals interactions determine the unique properties of water, *Proceedings of the National Academy of Sciences of the United States of America*, 113, 30, 8368–8373, 2016.

[4] Marsalek, O. and Markland, T. E.: Quantum dynamics and spectroscopy of ab initio liquid water: The interplay of nuclear and electronic quantum effects, *Journal of Physical Chemistry Letters*, 8, 7, 1545–1551, 2017.

[5] Schran, C., Marsalek, O. and Markland, T. E.: Unravelling the influence of quantum proton delocalization on electronic charge transfer through the hydrogen bond, *Chemical Physics Letters*, 678, 289–295, 2017.

[6] Voet, D., Voet, J. G. and Pratt, C. W.: Fundamentals of biochemistry: Life at a molecular level, John Wiley & Sons, Hoboken, New Jersey, third edition, 2008.

[7] Brela, M. Z., Wójcik, M. J., Łukasz J. Witek et al.: Born–Oppenheimer molecular dynamics study on proton dynamics of strong hydrogen bonds in aspirin crystals, with emphasis on differences between two crystal forms, *Journal of Physical Chemistry B*, 120, 16, 3854–3862, 2016.

[8] Werling, K. A., Griffin, M., Hutchison, G. R. and Lambrecht, D. S.: Piezoelectric hydrogen bonding: Computational screening for a design rationale, *Journal of Physical Chemistry A*, 118, 35, 7404–7410, 2014.

[9] Altaner, C. M., Thomas, L. H., Fernandes, A. N. and Jarvis, M. C.: How cellulose stretches: Synergism between covalent and hydrogen bonding, *Biomacromolecules*, 15, 3, 791–798, 2014.

[10] Puiggalí, J. and Brill, D. S.: Aliphatic polyamides (nylons): Interplay between hydrogen bonds and crystalline structures, polymorphic transitions and crystallization, *Polymer Crystallization*, 4, 4, e10199, 2021.

[11] Schroeder, C., Siozios, V., Mück-Lichtenfeld, C. et al.: Hydrogen bond formation of Brønsted acid sites in zeolites, *Chemistry of Materials*, 32, 4, 1564–1574, 2020.

[12] Wernet, P., Nordlund, D., Bergmann, U. et al.: The structure of the first coordination shell in liquid water, *Science*, 304, 5673, 995–999, 2004.

[13] Smith, J. D., Cappa, C. D., Wilson, K. R. et al.: Energetics of hydrogen bond network rearrangements in liquid water, *Science*, 306, 5697, 851–853, 2004.

[14] Chen, M., Ko, H. Y., Remsing, R. C. et al.: Ab initio theory and modeling of water, *Proceedings of the National Academy of Sciences of the United States of America*, 114, 41, 10846–10851, 2017.

[15] Glazier, S., Marano, N. and Eisen, L.: A closer look at trends in boiling points of hydrides: Using an inquiry-based approach to teach intermolecular forces of attraction, *Journal of Chemical Education*, 87, 12, 1336–1341, 2010.

[16] Sakurai, J. J. and Napolitano, J.: Modern Quantum Mechanics, Cambridge University Press, Cambridge, third edition, 2021.

[17] Cejnar, P.: A Condensed Course of Quantum Mechanics, Karolinum Press, Prague, 2013.

[18] Markland, T. E. and Ceriotti, M.: Nuclear quantum effects enter the mainstream, *Nature Reviews Chemistry*, 2, 3, 1–14, 2018.

[19] Markland, T. E. and Berne, B. J.: Unraveling quantum mechanical effects in water using isotopic fractionation, *Proceedings of the National Academy of Sciences of the United States of America*, 109, 21, 7988–7991, 2012.

[20] Marsalek, O., Chen, P. Y., Dupuis, R. et al.: Efficient calculation of free energy differences associated with isotopic substitution using path-integral molecular dynamics, *Journal of Chemical Theory and Computation*, 10, 4, 1440–1453, 2014.

[21] Sugimoto, H.: The Ubbelohde effect in hydrogen-bonded crystalline, *Journal of Physics: Condensed Matter*, 10, 6, 1237, 1998.

[22] Li, X. Z., Walker, B. and Michaelides, A.: Quantum nature of the hydrogen bond, *Proceedings of the National Academy of Sciences of the United States of America*, 108, 16, 6369–6373, 2011.

[23] Blahut, A., Hykl, J., Peukert, P., Vinš, V. and Hrubý, J.: Relative density and isobaric expansivity of cold and supercooled heavy water from 254 to 298 K and up to 100 MPa, *Journal of Chemical Physics*, 151, 3, 34505, 2019.

[24] Habershon, S., Markland, T. E. and Manolopoulos, D. E.: Competing quantum effects in the dynamics of a flexible water model, *Journal of Chemical Physics*, 131, 2, 2009.

[25] Ceriotti, M., Fang, W., Kusalik, P. G. et al.: Nuclear quantum effects in water and aqueous systems: Experiment, theory, and current challenges, *Chemical Reviews*, 116, 13, 7529–7550, 2016.

[26] Schran, C.: Properties of hydrogen bonding at ultra-low temperatures in superfluid quantum solvents, Ph.D. thesis, Ruhr-Universität Bochum, 2019.

[27] Frenkel, D. and Smit, B.: Understanding Molecular Simulation, Academic Press, London, 2002.

[28] Schmidtmann, M., Coster, P., Henry, P. F. et al.: Determining hydrogen positions in crystal engineered organic molecular complexes by joint neutron powder and single crystal x-ray diffraction, *CrystEngComm*, 16, 7, 1232–1236, 2014.

[29] Kawai, S., Nishiuchi, T., Kodama, T. et al.: Direct quantitative measurement of the C=O···H–C bond by atomic force microscopy, *Science Advances*, 3, 5, 2017.

[30] Feynman, R. P.: Space-time approach to non-relativistic quantum mechanics, *Reviews of Modern Physics*, 20, 2, 367, 1948.

[31] Tuckerman, M. E.: Statistical mechanics: theory and molecular simulation, Oxford University Press Inc., New York, 2010, ISBN 9787-0-19-852526-4.

[32] Born, M. and Oppenheimer, R.: Zur quantentheorie der molekeln, *Annalen der Physik*, 389, 20, 457–484, 1927.

[33] Vandevondele, J., Borštnik, U. and Hutter, J.: Linear scaling self-consistent field calculations with millions of atoms in the condensed phase, *Journal of Chemical Theory and Computation*, 8, 10, 3565–3573, 2012.

[34] Hohenberg, P. and Kohn, W.: Inhomogeneous electron gas, *Physical Review*, 136, B864–B871, 1964.

[35] Friederich, P., Häse, F., Proppe, J. and Aspuru-Guzik, A.: Machine-learned potentials for next-generation matter simulations, *Nature Materials*, 20, 6, 750–761, 2021.

[36] Behler, J. and Parrinello, M.: Generalized neural-network representation of high-dimensional potential-energy surfaces, *Physical Review Letters*, 98, 14, 146401, 2007.

[37] Hertz, J., Krogh, A. and Palmer, R. G.: Introduction to the theory of neural computation, CRC Press, 1991.

[38] Schran, C., Thiemann, F. L., Rowe, P. et al.: Machine learning potentials for complex aqueous systems made simple, *Proceedings of the National Academy of Sciences of the United States of America*, 118, 38, e2110077118, 2021.

[39] Zeni, C., Anelli, A., Glielmo, A. and Rossi, K.: Exploring the robust extrapolation of high-dimensional machine learning potentials, *Physical Review B*, 105, 16, 165141, 2022.

[40] Ceriotti, M., Tribello, G. A. and Parrinello, M.: Demonstrating the transferability and the descriptive power of sketch-map, *Journal of Chemical Theory and Computation*, 9, 3, 1521–1532, 2013.

[41] Hansen, L. K. and Salamon, P.: Neural network ensembles, *IEEE Transactions on Pattern Analysis and Machine Intelligence*, 12, 10, 993–1001, 1990.

[42] Krogh, A. and Vedelsby, J.: Neural network ensembles, cross validation, and active learning, *Advances in Neural Information Processing Systems 7*, 231–238, 1995.

[43] Schran, C., Brezina, K. and Marsalek, O.: Committee neural network potentials control generalization errors and enable active learning, *The Journal of Chemical Physics*, 153, 10, 104105, 2020.

[44] Seung, H. S., Opper, M. and Sompolinsky, H.: Query by committee, *Proceedings of the fifth annual workshop on Computational learning theory - COLT '92*, 287–294, 1992.

[45] Artrith, N. and Behler, J.: High-dimensional neural network potentials for metal surfaces: A prototype study for copper, *Physical Review B - Condensed Matter and Materials Physics*, 85, 4, 045439, 2012.

[46] Brezina, K., Beck, H. and Marsalek, O.: Reducing the cost of neural network potential generation for reactive molecular systems, *Journal of Chemical Theory and Computation*, 19, 19, 6589–6604, 2023.

[47] Mason, P. E., Uhlig, F., Vaněk, V. et al.: Coulomb explosion during the early stages of the reaction of alkali metals with water, *Nature Chemistry*, 7, 3, 250–254, 2015.

[48] Mason, P. E., Buttersack, T., Bauerecker, S. and Jungwirth, P.: A non-exploding alkali metal drop on water: From blue solvated electrons to bursting molten hydroxide, *Angewandte Chemie International Edition*, 55, 42, 13019–13022, 2016.

[49] Jortner, J. and Kestner, N. R.: Electrons in Fluids, Springer-Verlag, New York, New York, 1973.

[50] Thompson, J. C.: Electrons in Liquid Ammonia, Clanderon Press, Oxford, 1976.

[51] Zurek, E., Edwards, P. P. and Hoffmann, R.: A molecular perspective on lithium-ammonia solutions, *Angewandte Chemie International Edition*, 48, 44, 8198–8232, 2009.

[52] Buttersack, T., Mason, P. E., McMullen, R. S. et al.: Valence and core-level X-ray photoelectron spectroscopy of a liquid ammonia microjet, *Journal of the American Chemical Society*, 141, 5, 1838–1841, 2019.

[53] Faubel, M., Steiner, B. and Toennies, J. P.: Photoelectron spectroscopy of liquid water, some alcohols, and pure nonane in free micro jets, *The Journal of Chemical Physics*, 106, 22, 9013–9031, 1997.

[54] Buttersack, T., Mason, P. E., Jungwirth, P. et al.: Deeply cooled and temperature controlled microjets: Liquid ammonia solutions released into vacuum for analysis by photoelectron spectroscopy, *Review of Scientific Instruments*, 91, 4, 43101, 2020.

[55] Seidel, R., Pohl, M. N., Ali, H., Winter, B. and Aziz, E. F.: Advances in liquid phase soft-x-ray photoemission spectroscopy: A new experimental setup at BESSY II, *Review of Scientific Instruments*, 88, 7, 73107, 2017.

[56] Miedema, P. S., Quevedo, W. and Fondell, M.: The variable polarization undulator beamline UE52 SGM at BESSY II, *Journal of large-scale research facilities*, 2, A70–A70, 2016.

[57] Hüser, F., Olsen, T. and Thygesen, K. S.: Quasiparticle GW calculations for solids, molecules, and two-dimensional materials, *Physical Review B*, 87, 235132, 2013.

[58] Lundholm, M., Siegbahn, H., Holmberg, S. and Arbman, M.: Core electron spectroscopy of water solutions, *Journal of Electron Spectroscopy and Related Phenomena*, 40, 2, 163–180, 1986.

[59] Shkrob, I. A.: Ammoniated electron as a solvent stabilized multimer radical anion, *Journal of Physical Chemistry A*, 110, 11, 3967–3976, 2006.

[60] Kaplan, J. and Kittel, C.: A model of metal-ammonia solutions, with reference to electron spin resonance experiments, *The Journal of Chemical Physics*, 21, 9, 1429–1433, 1953.

[61] Glover, W. J. and Schwartz, B. J.: Short-range electron correlation stabilizes noncavity solvation of the hydrated electron, *Journal of Chemical Theory and Computation*, 12, 10, 5117–5131, 2016.

[62] Buttersack, T., Mason, P. E., McMullen, R. S. et al.: Photoelectron spectra of alkali metal-ammonia microjets: From blue electrolyte to bronze metal, *Science*, 368, 6495, 1086–1091, 2020.

[63] Bao, J. L., Gagliardi, L. and Truhlar, D. G.: Self-interaction error in density functional theory: An appraisal, *Journal of Physical Chemistry Letters*, 9, 9, 2353–2358, 2018.

[64] Marsalek, O., Uhlig, F. and Jungwirth, P.: Electrons in cold water clusters: An ab initio molecular dynamics study of localization and metastable states, *Journal of Physical Chemistry C*, 114, 48, 20489–20495, 2010.

[65] Marsalek, O., Uhlig, F., Frigato, T., Schmidt, B. and Jungwirth, P.: Dynamics of electron localization in warm versus cold water clusters, *Physical Review Letters*, 105, 4, 043002, 2010.

[66] Wilhelm, J., Ben, M. D. and Hutter, J.: GW in the gaussian and plane waves scheme with application to linear acenes, *Journal of Chemical Theory and Computation*, 12, 8, 3623–3635, 2016.

[67] Cossi, M. and Barone, V.: Solvent effect on vertical electronic transitions by the polarizable continuum model, *The Journal of Chemical Physics*, 112, 5, 2427–2435, 2000.

[68] Birch, A. J.: Reduction by dissolving metals, *Nature*, 158, 4017, 585, 1946.

[69] Birch, A. J.: The Birch reduction in organic synthesis, *Pure and Applied Chemistry*, 68, 3, 553–556, 1996.

[70] Joshi, D. K., Sutton, J. W., Carver, S. and Blanchard, J. P.: Experiences with commercial production scale operation of dissolving metal reduction using lithium metal and liquid ammonia, *Organic Process Research and Development*, 9, 6, 997–1002, 2005.

[71] Brezina, K., Jungwirth, P. and Marsalek, O.: Benzene radical anion in the context of the Birch reduction: When solvation is the key, *Journal of Physical Chemistry Letters*, 11, 15, 6032–6038, 2020.

[72] Brezina, K., Kostal, V., Jungwirth, P. and Marsalek, O.: Electronic structure of the solvated benzene radical anion, *Journal of Chemical Physics*, 156, 1, 14501, 2022.

[73] Kostal, V., Brezina, K., Marsalek, O. and Jungwirth, P.: Benzene radical anion microsolvated in ammonia clusters: Modeling the transition from an unbound resonance to a bound species, *Journal of Physical Chemistry A*, 125, 26, 5811–5818, 2021.

[74] Schewe, H. C., Brezina, K., Kostal, V. et al.: Photoelectron spectroscopy of benzene in the liquid phase and dissolved in liquid ammonia, *Journal of Physical Chemistry B*, 126, 1, 229–238, 2022.

[75] Nemirovich, T., Young, B., Brezina, K. et al.: Stability and reactivity of aromatic radical anions in solution with relevance to Birch reduction, *Journal of the American Chemical Society*, 2024.

[76] Faksness, L. G., Brandvik, P. J. and Sydnes, L. K.: Composition of the water accommodated fractions as a function of exposure times and temperatures, *Marine Pollution Bulletin*, 56, 10, 1746–1754, 2008.

[77] Arnold, D. S., Plank, C. A., Erickson, E. E. and Pike, F. P.: Solubility of benzene in water, *Journal of Chemical and Engineering Data*, 3, 2, 253–256, 1958.

[78] Mardirossian, N. and Head-Gordon, M.: ωB97M-V: A combinatorially optimized, range-separated hybrid, meta-GGA density functional with VV10 nonlocal correlation, *Journal of Chemical Physics*, 144, 21, 214110, 2016.

[79] Suzuki, S., Green, P. G., Bumgarner, R. E. et al.: Benzene forms hydrogen bonds with water, *Science*, 257, 5072, 942–945, 1992.

[80] Gierszal, K. P., Davis, J. G., Hands, M. D. et al.: π-hydrogen bonding in liquid water, *Journal of Physical Chemistry Letters*, 2, 22, 2930–2933, 2011.

[81] Perera, P., Wyche, M., Loethen, Y. and Ben-Amotz, D.: Solute-induced perturbations of solvent-shell molecules observed using multivariate Raman curve resolution, *Journal of the American Chemical Society*, 130, 14, 4576–4577, 2008.

[82] Boyer, M. A., Marsalek, O., Heindel, J. P. et al.: Beyond Badger's rule: The origins and generality of the structure-spectra relationship of aqueous hydrogen bonds, *Journal of Physical Chemistry Letters*, 10, 5, 918–924, 2019.

[83] Allesch, M., Schwegler, E. and Galli, G.: Structure of hydrophobic hydration of benzene and hexafluorobenzene from first principles, *Journal of Physical Chemistry B*, 111, 5, 1081–1089, 2007.

[84] Allesch, M., Lightstone, F. C., Schwegler, E. and Galli, G.: First principles and classical molecular dynamics simulations of solvated benzene, *Journal of Chemical Physics*, 128, 1, 14501, 2008.

[85] Choudhary, A. and Chandra, A.: Spatial and orientational structure of the hydration shell of benzene in sub- and supercritical water, *Journal of Physical Chemistry B*, 119, 27, 8600–8612, 2015.

[86] Mallik, B. S., Semparithi, A. and Chandra, A.: Vibrational spectral diffusion and hydrogen bond dynamics in heavy water from first principles, *Journal of Physical Chemistry A*, 112, 23, 5104–5112, 2008.

[87] Brezina, K., Beck, H. and Marsalek, O.: Elucidating the nature of π-hydrogen bonding in liquid water and ammonia, *arXiv:2403.12937*, 2024.

[88] Simpson, G. J., Hogan, S. W., Caffio, M. et al.: New class of metal bound molecular switches involving H-tautomerism, *Nano Letters*, 14, 2, 634–639, 2014.

[89] Simpson, G. J., Persson, M. and Grill, L.: Adsorbate motors for unidirectional translation and transport, *Nature*, 621, 7977, 82–86, 2023.

[90] Litman, Y., Donadio, D., Ceriotti, M. and Rossi, M.: Decisive role of nuclear quantum effects on surface mediated water dissociation at finite temperature, *Journal of Chemical Physics*, 148, 10, 102320, 2018.

[91] Garrett, T. R., Bhakoo, M. and Zhang, Z.: Bacterial adhesion and biofilms on surfaces, *Progress in Natural Science*, 18, 9, 1049–1056, 2008.

[92] Li, P., Jiang, Y., Hu, Y. et al.: Hydrogen bond network connectivity in the electric double layer dominates the kinetic pH effect in hydrogen electrocatalysis on Pt, *Nature Catalysis*, 5, 10, 900–911, 2022.

[93] Cahlík, A., Hellerstedt, J., Mendieta-Moreno, J. I. et al.: Significance of nuclear quantum effects in hydrogen bonded molecular chains, *ACS Nano*, 15, 6, 10357–10365, 2021.

[94] Sankey, O. F. and Niklewski, D. J.: Ab initio multicenter tight-binding model for molecular-dynamics simulations and other applications in covalent systems, *Physical Review B*, 40, 6, 3979, 1989.

[95] Gerrits, N., Smeets, E. W., Vuckovic, S. et al.: Density functional theory for molecule-metal surface reactions: When does the generalized gradient approximation get it right, and what to do if it does not, *Journal of Physical Chemistry Letters*, 11, 24, 10552–10560, 2020.

[96] Kästner, J.: Theory and simulation of atom tunneling in chemical reactions, *Wiley Interdisciplinary Reviews: Computational Molecular Science*, 4, 2, 158–168, 2014.

[97] Marx, D. and Hutter, J.: Ab initio molecular dynamics: basic theory and advanced methods, Cambridge University Press, New York, 2009, ISBN 978-0-521-89863-8.

[98] Formánek, J.: Úvod do kvantové teorie, Academia, Prague, 2004, ISBN 80-200-1176-5.

[99] Hirshberg, B., Rizzi, V. and Parrinello, M.: Path integral molecular dynamics for bosons, *Proceedings of the National Academy of Sciences of the United States of America*, 116, 43, 21445–21449, 2019.

[100] Schran, C., Behler, J. and Marx, D.: Automated fitting of neural network potentials at coupled cluster accuracy: Protonated water clusters as testing ground, *Journal of Chemical Theory and Computation*, 16, 1, 88–99, 2020.

[101] Lipavský, J.: Teorie kondenzovaného stavu I (poznámky k přednášce, Matematicko-fyzikální fakulta UK).

[102] Malhado, J. P., Bearpark, M. J. and Hynes, J. T.: Non-adiabatic dynamics close to conical intersections and the surface hopping perspective, *Frontiers in Chemistry*, 2, 1–21, 2014.

[103] Barbatti, M.: Nonadiabatic dynamics with trajectory surface hopping method, *Wiley Interdisciplinary Reviews: Computational Molecular Science*, 1, 4, 620–633, 2011.

[104] Dickhoff, W. H. and Neck, D. V.: Many-body theory exposed! Propagator description of quantum mechanics in many-body systems, World Scientific Publishing Co. Pte. Ltd., Singapore, 2005, ISBN 981-256-294-X.

[105] Lehmann, H.: Über Eigenschaften von Ausbreitungsfunktionen und Renormierungskonstanten quantisierter Felder, *Il Nuovo Cimento*, 11, 342–357, 1954.

[106] Szabo, A. and Ostlund, N. S.: Modern quantum chemistry: Introduction to advanced electronic structure theory, Dover Publications, Inc., Mineola, New York, 1996.

[107] Parr, R. G. and Yang, W.: Density-functional theory of atoms and molecules, Oxford University Press, New York, 1989.

[108] Capelle, K.: A bird's-eye view of density-functional theory, *Brazilian Journal of Physics*, 36, 1318–1343, 2006.

[109] Kohn, W. and Sham, L. J.: Self-consistent equations including exchange and correlation effects, *Physical Review*, 140, A1133–A1138, 1965.

[110] Niquet, Y. M., Fuchs, M. and Gonze, X.: Asymptotic behavior of the exchange-correlation potentials from the linear-response Sham–Schlüter equation, *The Journal of Chemical Physics*, 118, 21, 9504–9518, 2003.

[111] Perdew, J. P. and Schmidt, K.: Jacob's ladder of density functional approximations for the exchange-correlation energy, *AIP Conference Proceedings*, 577, 1, 1–20, 2001.

[112] Bagayoko, D.: Understanding density functional theory (DFT) and completing it in practice, *AIP Advances*, 4, 12, 127104, 2014.

[113] Perdew, J. P., Chevary, J. A., Vosko, S. H. et al.: Atoms, molecules, solids, and surfaces: Applications of the generalized gradient approximation for exchange and correlation, *Physical Review B*, 46, 11, 6671, 1992.

[114] Perdew, J. P., Burke, K. and Ernzerhof, M.: Generalized gradient approximation made simple, *Physical Review Letters*, 77, 18, 3865–3868, 1996.

[115] Zhang, Y. and Yang, W.: Comment on "Generalized gradient approximation made simple", *Physical Review Letters*, 80, 4, 890, 1998.

[116] Becke, A. D.: Density-functional exchange-energy approximation with correct asymptotic behavior, *Physical Review A*, 38, 6, 3098, 1988.

[117] Lee, C., Yang, W. and Parr, R. G.: Development of the Colle-Salvetti correlation-energy formula into a functional of the electron density, *Physical Review B*, 37, 2, 785, 1988.

[118] Heyd, J., Scuseria, G. E. and Ernzerhof, M.: Hybrid functionals based on a screened coulomb potential, *The Journal of Chemical Physics*, 118, 18, 8207–8215, 2003.

[119] Adamo, C. and Barone, V.: Toward reliable density functional methods without adjustable parameters: The PBE0 model, *Journal of Chemical Physics*, 110, 13, 6158–6170, 1999.

[120] Becke, A. D.: Density-functional thermochemistry. III. The role of exact exchange, *The Journal of Chemical Physics*, 98, 7, 5648–5652, 1993.

[121] Grimme, S.: Accurate description of van der waals complexes by density functional theory including empirical corrections, *Journal of Computational Chemistry*, 25, 12, 1463–1473, 2004.

[122] Grimme, S.: Semiempirical GGA-type density functional constructed with a long-range dispersion correction, *Journal of Computational Chemistry*, 27, 15, 1787–1799, 2006.

[123] Grimme, S., Hansen, A., Brandenburg, J. G. and Bannwarth, C.: Dispersion-corrected mean-field electronic structure methods, *Chemical Reviews*, 116, 9, 5105–5154, 2016.

[124] Goerigk, L. and Grimme, S.: A thorough benchmark of density functional methods for general main group thermochemistry, kinetics, and noncovalent interactions, *Physical Chemistry Chemical Physics*, 13, 14, 6670–6688, 2011.

[125] Tkatchenko, A. and Scheffler, M.: Accurate molecular van der Waals interactions from ground-state electron density and free-atom reference data, *Physical Review Letters*, 102, 7, 073005, 2009.

[126] Tkatchenko, A., Distasio, R. A., Car, R. and Scheffler, M.: Accurate and efficient method for many-body van der Waals interactions, *Physical Review Letters*, 108, 23, 236402, 2012.

[127] Vydrov, O. A. and Voorhis, T. V.: Nonlocal van der Waals density functional: The simpler the better, *Journal of Chemical Physics*, 133, 24, 2010.

[128] Klimeš, J., Bowler, D. R. and Michaelides, A.: Chemical accuracy for the van der waals density functional, *Journal of Physics: Condensed Matter*, 22, 2, 022201, 2009.

[129] Klimeš, J., Bowler, D. R. and Michaelides A.: Van der Waals density functionals applied to solids, *Physical Review B - Condensed Matter and Materials Physics*, 83, 19, 195131, 2011.

[130] Koopmans, T.: Über die Zuordnung von Wellenfunktionen und Eigenwerten zu den einzelnen Elektronen eines Atoms, *Physica*, 1, 104–113, 1934.

[131] Janak, J. F.: Proof that $\partial E/\partial n_i = \epsilon_i$ in density-functional theory, *Physical Review B*, 18, 12, 7165–7168, 1978.

[132] Bruneval, F. and Gatti, M.: Quasiparticle self-consistent GW method for the spectral properties of complex materials, *Topics in Current Chemistry*, 347, 99–136, 2014.

[133] Slavíček, P., Muchová, E., Hollas, D., Svoboda, V. and Svoboda, O.: Kvantová chemie: první čtení, VŠCHT Praha, Prague, 2019.

[134] Obara, S. and Saika, A.: Efficient recursive computation of molecular integrals over Cartesian Gaussian functions, *The Journal of Chemical Physics*, 84, 7, 3963–3974, 1986.

[135] Kühne, T. D., Iannuzzi, M., Ben, M. D. et al.: Cp2k: An electronic structure and molecular dynamics software package - quickstep: Efficient and accurate electronic structure calculations, *The Journal of Chemical Physics*, 152, 19, 194103, 2020.

[136] Vandevondele, J., Krack, M., Mohamed, F. et al.: Quickstep: Fast and accurate density functional calculations using a mixed gaussian and plane waves approach, *Computer Physics Communications*, 167, 2, 103–128, 2005.

[137] Guidon, M., Schiffmann, F., Hutter, J. and Vandevondele, J.: Ab initio molecular dynamics using hybrid density functionals, *Journal of Chemical Physics*, 128, 21, 1–15, 2008.

[138] Guidon, M., Hutter, J. and VandeVondele, J.: Robust periodic Hartree-Fock exchange for large-scale simulations using Gaussian basis sets, *Journal of Chemical Theory and Computation*, 5, 11, 3010–3021, 2009.

[139] Guidon, M., Hutter, J. and Vandevondele, J.: Auxiliary density matrix methods for Hartree-Fock exchange calculations, *Journal of Chemical Theory and Computation*, 6, 8, 2348–2364, 2010.

[140] Blum, V., Gehrke, R., Hanke, F. et al.: Ab initio molecular simulations with numeric atom-centered orbitals, *Computer Physics Communications*, 180, 11, 2175–2196, 2009.

[141] Neugebauer, J. and Scheffler, M.: Adsorbate-substrate and adsorbate-adsorbate interactions of Na and K adlayers on Al(111), *Physical Review B*, 46, 24, 16067, 1992.

[142] Feynman, R. P. and Hibbs, A. R.: Quantum mechanics and path integrals, McGraw-Hill Companies, Inc., New York, New Yrok, 1965.

[143] Trotter, H. F.: On the product of semi-groups of operators, *Proceedings of the American Mathematical Society*, 10, 545–551, 1959.

[144] Verlet, L.: Computer experiments on classical fluids. I. thermodynamical properties of Lennard-Jones molecules, *Physical Review*, 159, 98–103, 1967.

[145] Abraham, M. J., Murtola, T., Schulz, R. et al.: Gromacs: High performance molecular simulations through multi-level parallelism from laptops to supercomputers, *SoftwareX*, 1-2, 19–25, 2015.

[146] Martyna, G. J., Tuckerman, M. E., Tobias, D. J. and Klein, M. L.: Explicit reversible integrators for extended systems dynamics, *Molecular Physics*, 87, 5, 1117–1157, 2006.

[147] Leimkuhler, B. and Matthews, C.: Rational construction of stochastic numerical methods for molecular sampling, *Applied Mathematics Research eXpress*, 2013, 1, 34–56, 2013.

[148] Nosé, S.: A unified formulation of the constant temperature molecular dynamics methods, *The Journal of Chemical Physics*, 81, 1, 511–519, 1984.

[149] Hoover, W. G.: Canonical dynamics: Equilibrium phase-space distributions, *Physical Review A*, 31, 3, 1695–1697, 1985.

[150] Tuckerman, M., Berne, B. J. and Martyna, G. J.: Reversible multiple time scale molecular dynamics, *The Journal of Chemical Physics*, 97, 3, 1990–2001, 1992.

[151] Andersen, H. C.: Molecular dynamics simulations at constant pressure and/or temperature, *The Journal of Chemical Physics*, 72, 4, 2384–2393, 1980.

[152] Schneider, T. and Stoll, E.: Molecular-dynamics study of a three-dimensional one-component model for distortive phase transitions, *Physical Review B*, 17, 3, 1302, 1978.

[153] Bussi, G., Donadio, D. and Parrinello, M.: Canonical sampling through velocity rescaling, *Journal of Chemical Physics*, 126, 1, 14101, 2007.

[154] Bussi, G. and Parrinello, M.: Stochastic thermostats: comparison of local and global schemes, *Computer Physics Communications*, 179, 1-3, 26–29, 2008.

[155] Hall, R. W. and Berne, B. J.: Nonergodicity in path integral molecular dynamics, *The Journal of Chemical Physics*, 81, 8, 3641–3643, 1984.

[156] Cooley, J. W. and Tukey, J. W.: An algorithm for the machine calculation of complex Fourier series, *Mathematics of Computation*, 19, 90, 297–301, 1965.

[157] Ceriotti, M., Parrinello, M., Markland, T. E. and Manolopoulos, D. E.: Efficient stochastic thermostatting of path integral molecular dynamics., *The Journal of Chemical Physics*, 133, 12, 124104, 2010.

[158] Kapil, V., Rossi, M., Marsalek, O. et al.: i-PI 2.0: A universal force engine for advanced molecular simulations, *Computer Physics Communications*, 236, 214–223, 2019.

[159] Jónsson, H., Mills, G. and Jacobsen, K. W.: Nudged elastic band method for finding minimum energy paths of transitions, *Classical and Quantum Dynamics in Condensed Phase Simulations*, 385–404, 1998.

[160] Larsen, A. H., Mortensen, J. J., Blomqvist, J. et al.: The atomic simulation environment—a Python library for working with atoms, *Journal of Physics: Condensed Matter*, 29, 27, 273002, 2017.

[161] Kubo, R., Toda, M. and Hashitsume, N.: Statistical physics II. Nonequilibrium statistical mechanics, Springer Berlin Heidelberg, 1985, ISBN 978-3-642-96703-0.

[162] Cao, J. and Voth, G. A.: The formulation of quantum statistical mechanics based on the Feynman path centroid density. IV. algorithms for centroid molecular dynamics, *The Journal of Chemical Physics*, 101, 7, 6168–6183, 1994.

[163] Craig, I. R. and Manolopoulos, D. E.: Quantum statistics and classical mechanics: Real time correlation functions from ring polymer molecular dynamics, *The Journal of Chemical Physics*, 121, 8, 3368–3373, 2004.

[164] Habershon, S., Manolopoulos, D. E., Markland, T. E. and Miller, T. F.: Ring-polymer molecular dynamics: Quantum effects in chemical dynamics from classical trajectories in an extended phase space, *Annual Reviews of Physical Chemistry*, 64, 387–413, 2013.

[165] Hele, T. J., Willatt, M. J., Muolo, A. and Althorpe, S. C.: Communication: Relation of centroid molecular dynamics and ring-polymer molecular dynamics to exact quantum dynamics, *Journal of Chemical Physics*, 142, 19, 191101, 2015.

[166] Habershon, S., Fanourgakis, G. S. and Manolopoulos, D. E.: Comparison of path integral molecular dynamics methods for the infrared absorption spectrum of liquid water, *Journal of Chemical Physics*, 129, 7, 2008.

[167] Rossi, M., Ceriotti, M. and Manolopoulos, D. E.: How to remove the spurious resonances from ring polymer molecular dynamics, *Journal of Chemical Physics*, 140, 23, 2014.

[168] Lee, H. S. and Tuckerman, M. E.: Dynamical properties of liquid water from ab initio molecular dynamics performed in the complete basis set limit, *Journal of Chemical Physics*, 126, 16, 2007.

[169] Hunt, P., Sprik, M. and Vuilleumier, R.: Thermal versus electronic broadening in the density of states of liquid water, *Chemical Physics Letters*, 376, 1-2, 68–74, 2003.

[170] Morawietz, T., Marsalek, O., Pattenaude, S. R. et al.: The interplay of structure and dynamics in the Raman spectrum of liquid water over the full frequency and temperature range, *Journal of Physical Chemistry Letters*, 9, 4, 851–857, 2018.

[171] Morita, A. and Hynes, J. T.: A theoretical analysis of the sum frequency generation spectrum of the water surface, *Chemical Physics*, 258, 2-3, 371–390, 2000.

[172] Miller, W. H., Schwartz, S. D. and Tromp, J. W.: Quantum mechanical rate constants for bimolecular reactions, *The Journal of Chemical Physics*, 79, 10, 4889–4898, 1983.

[173] Craig, I. R. and Manolopoulos, D. E.: A refined ring polymer molecular dynamics theory of chemical reaction rates, *Journal of Chemical Physics*, 123, 3, 034102, 2005.

[174] Chandler, D.: Statistical mechanics of isomerization dynamics in liquids and the transition state approximation, *The Journal of Chemical Physics*, 68, 6, 2959–2970, 1978.

[175] Richardson, J. O. and Althorpe, S. C.: Ring-polymer molecular dynamics rate-theory in the deep-tunneling regime: Connection with semiclassical instanton theory, *Journal of Chemical Physics*, 131, 21, 2009.

[176] Richardson, J. O.: Derivation of instanton rate theory from first principles, *Journal of Chemical Physics*, 144, 11, 2016.

[177] Althorpe, S. C.: On the equivalence of two commonly used forms of semiclassical instanton theory, *Journal of Chemical Physics*, 134, 11, 2011.

[178] Rommel, J.: Improvements to the instanton method: Tunneling rates in the enzyme glutamate mutase, Ph.D. thesis, Universität Stuttgart, Stuttgart, 2012.

[179] Litman, Y.: Tunneling and zero-point energy effects in multidimensional hydrogen transfer reactions: From gas phase to adsorption on metal surfaces, Ph.D. thesis, Freie Universität Berlin, Berlin, 2020.

[180] Litman, Y. and Rossi, M.: Multidimensional hydrogen tunneling in supported molecular switches: The role of surface interactions, *Physical Review Letters*, 125, 21, 216001, 2020.

[181] Rumelhart, D. E., Hinton, G. E. and Williams, R. J.: Learning representations by back-propagating errors, *Nature*, 323, 6088, 533–536, 1986.

[182] Levenberg, K. and Arsenal, F.: A method for the solution of certain nonlinear problems in least squares, *Quarterly of Applied Mathematics*, 2, 2, 164–168, 1944.

[183] Broyden, C. G.: The convergence of a class of double-rank minimization algorithms 1. general considerations, *IMA Journal of Applied Mathematics*, 6, 1, 76–90, 1970.

[184] Fletcher, R.: A new approach to variable metric algorithms, *The Computer Journal*, 13, 3, 317–322, 1970.

[185] Goldfarb, D.: A family of variable-metric methods derived by variational means, *Mathematics of Computation*, 24, 109, 23, 1970.

[186] Shanno, D. F.: Conditioning of quasi-Newton methods for function minimization, *Mathematics of Computation*, 24, 111, 647, 1970.

[187] Byrd, R. H., Lu, P., Nocedal, J. and Zhu, C.: A limited memory algorithm for bound constrained optimization, *SIAM Journal on Scientific Computing*, 16, 5, 1190–1208, 2006.

[188] Kalman, R. E.: A new approach to linear filtering and prediction problems, *Journal of Basic Engineering*, 82, 1, 35–45, 1960.

[189] Imbalzano, G., Anelli, A., Giofré, D. et al.: Automatic selection of atomic fingerprints and reference configurations for machine-learning potentials, *Journal of Chemical Physics*, 148, 24, 241730, 2018.

[190] Gastegger, M., Schwiedrzik, L., Bittermann, M., Berzsenyi, F. and Marquetand, P.: WACSF - weighted atom-centered symmetry functions as descriptors in machine learning potentials, *Journal of Chemical Physics*, 148, 24, 241709, 2018.

[191] Singraber, A., Morawietz, T., Behler, J. and Dellago, C.: Parallel multistream training of high-dimensional neural network potentials, *Journal of Chemical Theory and Computation*, 15, 5, 3075–3092, 2019.

[192] Singraber, A., Behler, J. and Dellago, C.: Library-based LAMMPS implementation of high-dimensional neural network potentials, *Journal of Chemical Theory and Computation*, 15, 3, 1827–1840, 2019.

[193] Bogojeski, M., Vogt-Maranto, L., Tuckerman, M. E., Müller, K. R. and Burke, K.: Quantum chemical accuracy from density functional approximations via machine learning, *Nature Communications*, 11, 1, 1–11, 2020.

[194] Schütt, K. T., Kindermans, P.-J., Sauceda, H. E. et al.: SchNet: A continuous-filter convolutional neural network for modeling quantum interactions, *Advances in Neural Information Processing Systems*, 991–1001, 2017.

[195] Schütt, K. T., Unke, O. T. and Gastegger, M.: Equivariant message passing for the prediction of tensorial properties and molecular spectra, *Proceedings of Machine Learning Research*, 139, 2021.

[196] Kondor, R. and Trivedi, S.: On the generalization of equivariance and convolution in neural networks to the action of compact groups, *Proccedings of Machine Learning Research*, 80, 2747–2755, 2018.

[197] Batzner, S., Musaelian, A., Sun, L. et al.: E(3)-equivariant graph neural networks for data-efficient and accurate interatomic potentials, *Nature Communications*, 13, 1, 2022.

[198] Batatia, I., Kovács, D. P., Simm, G. N., Ortner, C. and Csányi, G.: MACE: Higher order equivariant message passing neural networks for fast and accurate force fields, *Advances in Neural Information Processing Systems*, 35, 2022.

[199] Takamoto, S., Shinagawa, C., Motoki, D. et al.: Towards universal neural network potential for material discovery applicable to arbitrary combination of 45 elements, *Nature Communications*, 13, 1, 1–11, 2022.

[200] Batatia, I., Benner, P., Chiang, Y. et al.: A foundation model for atomistic materials chemistry, *arXiv:2401.00096*, 2023.

[201] Westermayr, J., Gastegger, M., Vörös, D. et al.: Deep learning study of tyrosine reveals that roaming can lead to photodamage, *Nature Chemistry*, 14, 8, 914–919, 2022.

[202] Smith, J. S., Isayev, O. and Roitberg, A. E.: ANI-1: an extensible neural network potential with DFT accuracy at force field computational cost, *Chemical Science*, 8, 4, 3192–3203, 2017.

[203] Gordon, M. S., Freitag, M. A., Bandyopadhyay, P. et al.: The effective fragment potential method: A QM-based MM approach to modeling environmental effects in chemistry, *Journal of Physical Chemistry A*, 105, 2, 306–307, 2000.

[204] Pysanenko, A., Bergmeister, S., Scheier, P. and Fárník, M.: Stabilization of benzene radical anion in ammonia clusters, *Physical Chemistry Chemical Physics*, 24, 44, 27128–27135, 2022.

[205] Nemirovich, T., Kostal, V., Copko, J. et al.: Bridging electrochemistry and photoelectron spectroscopy in the context of Birch reduction: Detachment energies and redox potentials of electron, dielectron, and benzene radical anion in liquid ammonia, *Journal of the American Chemical Society*, 144, 48, 22093–22100, 2022.

[206] Winter, B. and Faubel, M.: Photoemission from liquid aqueous solutions, *Chemical Reviews*, 106, 4, 1176–1211, 2006.

[207] Weigend, F. and Ahlrichs, R.: Balanced basis sets of split valence, triple zeta valence and quadruple zeta valence quality for H to Rn: Design and assessment of accuracy, *Physical Chemistry Chemical Physics*, 7, 18, 3297–3305, 2005.

[208] Grimme, S., Ehrlich, S. and Goerigk, L.: Effect of the damping function in dispersion corrected density functional theory, *Journal of Computational Chemistry*, 32, 7, 1456–1465, 2011.

[209] Epifanovsky, E., Gilbert, A. T., Feng, X. et al.: Software for the frontiers of quantum chemistry: An overview of developments in the Q-Chem 5 package, *Journal of Chemical Physics*, 155, 8, 84801, 2021.

[210] Henkelman, G., Uberuaga, B. P. and Jónsson, H.: Climbing image nudged elastic band method for finding saddle points and minimum energy paths, *Journal of Chemical Physics*, 113, 22, 9901–9904, 2000.

[211] Smedarchina, Z., Siebrand, W., Fernández-Ramos, A. and Meana-Pañeda, R.: Mechanisms of double proton transfer. theory and applications, *Zeitschrift fur Physikalische Chemie*, 222, 8-9, 1291–1309, 2008.

[212] Lenthe, E. V., Snijders, J. G. and Baerends, E. J.: The zero-order regular approximation for relativistic effects: The effect of spin–orbit coupling in closed shell molecules, *The Journal of Chemical Physics*, 105, 15, 6505–6516, 1996.

[213] Bilić, A., Reimers, J. R. and Hush, N. S.: Adsorption of pyridine on the gold(111) surface: Implications for "alligator clips"" for molecular wires, *Journal of Physical Chemistry B*, 106, 26, 6740–6747, 2002.

[214] Bilić, A., Reimers, J. R., Hush, N. S., Hoft, R. C. and Ford, M. J.: Adsorption of benzene on copper, silver, and gold surfaces, *Journal of Chemical Theory and Computation*, 2, 4, 1093–1105, 2006.

# List of Abbreviations

**STM** scanning tunneling microscopy . . . . . 7

**HF** Hartree–Fock . . . . . 26

**DFT** density functional theory . . . . . 8

**PES** potential energy (hyper)surface . . . . . 7

**GF** Green's function . . . . . 26

**SCF** self-consistent field . . . . . 30

**RHF** restricted HF . . . . . 38

**UHF** unrestricted HF . . . . . 38

**KS** Kohn–Sham . . . . . 26

**RKS** restricted KS . . . . . 39

**UKS** unrestricted KS . . . . . 39

**XPS** X-ray photoelectron spectroscopy . . . . . 10

**LCAO** linear combination of atomic orbitals . . . . . 41

**ERI** electron repulsion integral . . . . . 40

**GGA** generalized-gradient approximation . . . . . 16

**NQE** nuclear quantum effect . . . . . 6

**MD** molecular dynamics . . . . . 6

**RPMD** ring polymer molecular dynamics . . . . . 54

**TRPMD** thermostatted RPMD . . . . . 54

**ACF** autocorrelation function . . . . . 55

**VDOS** vibrational density of states . . . . . 56

**NN** neural network . . . . . 8

**ACSF** atom centered symmetry functions . . . . . 62

**MBD** many-body dispersion . . . . . 35

**PILE-L** local path-integral Langevin equation . . . . . 51

**PILE-G** global path-integral Langevin equation . . . . . 51

**FFT** fast Fourier transform . . . . . 51

**CMD** centroid molecular dynamics . . . . . 54

**MC** Monte Carlo . . . . . 7

**NEB** nudged elastic band . . . . . 53

**ASE** Atomic Simulation Environment . . . . . 53

**NMS** normal mode sampling . . . . . 71

**MEP** minimum energy path . . . . . 71

**SDF** spatial distribution function . . . . . 78

**RDF** radial distribution function . . . . . 78

**PDOS** projected density of states . . . . . 78

**TS** transition state . . . . . 58

# List of Publications

[43] Schran, C., Brezina, K. and Marsalek, O.: Committee neural network potentials control generalization errors and enable active learning, *The Journal of Chemical Physics*, 153, 10, 104105, 2020

[46] Brezina, K., Beck, H. and Marsalek, O.: Reducing the cost of neural network potential generation for reactive molecular systems, *Journal of Chemical Theory and Computation*, 19, 19, 6589–6604, 2023

[71] Brezina, K., Jungwirth, P. and Marsalek, O.: Benzene radical anion in the context of the Birch reduction: When solvation is the key, *Journal of Physical Chemistry Letters*, 11, 15, 6032–6038, 2020

[72] Brezina, K., Kostal, V., Jungwirth, P. and Marsalek, O.: Electronic structure of the solvated benzene radical anion, *Journal of Chemical Physics*, 156, 1, 14501, 2022

[87] Brezina, K., Beck, H. and Marsalek, O.: Elucidating the nature of $\pi$-hydrogen bonding in liquid water and ammonia, *arXiv:2403.12937*, 2024

# A | Derivations

In this Appendix, we present a compilation of mathematical derivations that are important for the completeness of the discussion of important concepts in the main text, but are too detail-oriented to be included there.

## A.1 | Fourier transform of the step function

For the reason of completeness of the non-trivial derivation of the Lehmann representation of the one-particle GF, we will now derive for future convenience the Fourier transform of the Heaviside step function

$$\Theta(t-t_0) = \begin{cases} 1, & t \geq t_0 \\ 0, & t < t_0, \end{cases} \tag{A.1}$$

which can be represented as the following limit

$$\Theta(t-t_0) = \lim_{\epsilon \to 0^+} \begin{cases} e^{-\frac{\epsilon}{\hbar}(t-t_0)}, & t \geq t_0 \\ 0, & t < t_0. \end{cases} \tag{A.2}$$

With this definition, the Fourier transform

$$\Theta(\omega) = \int_{-\infty}^{+\infty} \mathrm{d}\tau \; e^{i\omega\tau}\Theta(\tau), \tag{A.3}$$

where we use $\tau = t - t_0$, can be written as

$$\Theta(\omega) = \lim_{\epsilon \to 0^+} \int_0^{+\infty} \mathrm{d}\tau \; e^{i\omega\tau} e^{-\frac{\epsilon}{\hbar}\tau} = -\lim_{\epsilon \to 0^+} \frac{\hbar}{i} \frac{1}{\hbar\omega + i\epsilon}. \tag{A.4}$$

When the time argument of $\Theta$ is flipped to $t_0 - t$, the Fourier transform changes the sign both before the whole expression and before the regularizer $i\epsilon$, because of the need to evaluate a growing exponential $e^{\frac{\epsilon}{\hbar}(t-t_0)}$ between $-\infty$ and 0 rather than a decaying one between 0 and $\infty$.

## A.2 | Lehmann representation

Equipped with the Fourier transform of the step function, we can proceed to derive the Fourier transform of the one-particle GF, which is the Lehmann representation introduced in Equation 2.16. First, we transform the time-dependent

GF into a more convenient form. Expanding its Heisenberg-picture definition in Equation 2.14, we have

$$\begin{aligned} G^{(1)}(\mathbf{r},\mathbf{r}',t-t_0) = &-\frac{i}{\hbar}\Theta(t-t_0)\,\langle\psi_0|\,e^{\frac{i}{\hbar}\widehat{H}t}\widehat{\psi}(\mathbf{r}')e^{-\frac{i}{\hbar}\widehat{H}t}e^{\frac{i}{\hbar}\widehat{H}t_0}\widehat{\psi}^\dagger(\mathbf{r}')e^{-\frac{i}{\hbar}\widehat{H}t_0}\,|\psi_0\rangle \\ &+\frac{i}{\hbar}\Theta(t_0-t)\,\langle\psi_0|\,e^{\frac{i}{\hbar}\widehat{H}t_0}\widehat{\psi}(\mathbf{r}')e^{-\frac{i}{\hbar}\widehat{H}t_0}e^{\frac{i}{\hbar}\widehat{H}t}\widehat{\psi}^\dagger(\mathbf{r}')e^{-\frac{i}{\hbar}\widehat{H}t}\,|\psi_0\rangle\,. \end{aligned} \tag{A.5}$$

Straightforward operator manipulations give

$$\begin{aligned} G^{(1)}(\mathbf{r},\mathbf{r}',t-t_0) = &-\frac{i}{\hbar}\Theta(t-t_0)e^{\frac{i}{\hbar}E_0(t-t_0)}\,\langle\psi_0|\,\widehat{\psi}(\mathbf{r}')e^{-\frac{i}{\hbar}\widehat{H}(t-t_0)}\widehat{\psi}^\dagger(\mathbf{r}')\,|\psi_0\rangle \\ &+\frac{i}{\hbar}\Theta(t-t_0)e^{\frac{i}{\hbar}E_0(t_0-t)}\,\langle\psi_0|\,\widehat{\psi}^\dagger(\mathbf{r}')e^{-\frac{i}{\hbar}\widehat{H}(t_0-t)}\widehat{\psi}(\mathbf{r}')\,|\psi_0\rangle\,. \end{aligned} \tag{A.6}$$

At this point, we introduce an identity operator to the right of the remaining propagators in the form of a full set of states of a system with an added particle $|\psi_k^+\rangle$ to the first term (particle part) and a full set of states with a missing particle $|\psi_l^-\rangle$ to the second term (hole part), which yields

$$\begin{aligned} G^{(1)}(\mathbf{r},\mathbf{r}',t-t_0) = &-\sum_k \frac{i}{\hbar}\Theta(t-t_0)e^{\frac{i}{\hbar}(E_k^+-E_0)(t-t_0)}\,\langle\psi_0|\,\widehat{\psi}(\mathbf{r}')\,|\psi_k^+\rangle\,\langle\psi_k^+|\,\widehat{\psi}^\dagger(\mathbf{r}')\,|\psi_0\rangle \\ &+\sum_l \frac{i}{\hbar}\Theta(t_0-t)e^{\frac{i}{\hbar}(E_0-E_l^-)(t-t_0)}\,\langle\psi_0|\,\widehat{\psi}^\dagger(\mathbf{r}')\,|\psi_l^-\rangle\,\langle\psi_l^-|\,\widehat{\psi}(\mathbf{r}')\,|\psi_0\rangle\,. \end{aligned} \tag{A.7}$$

From this point, evaluating the Fourier transform

$$G^{(1)}(\mathbf{r},\mathbf{r}',\omega) = \int_{-\infty}^{+\infty} \mathrm{d}\tau\; G^{(1)}(\mathbf{r},\mathbf{r}',\tau)e^{i\omega\tau} \tag{A.8}$$

is performed easily term by term by invoking the above-derived Fourier representation of the step function and gives the Lehmann representation

$$\begin{aligned} G^{(1)}(\mathbf{r},\mathbf{r}',\omega) = &\lim_{\epsilon\to 0^+}\sum_k \frac{\langle\psi_0|\,\widehat{\psi}(\mathbf{r}')\,|\psi_k^+\rangle\,\langle\psi_k^+|\,\widehat{\psi}^\dagger(\mathbf{r})\,|\psi_0\rangle}{\hbar\omega-(E_k^+-E_0)+i\varepsilon} \\ &+\sum_l \frac{\langle\psi_0|\,\widehat{\psi}^\dagger(\mathbf{r})\,|\psi_l^-\rangle\,\langle\psi_l^-|\,\widehat{\psi}(\mathbf{r}')\,|\psi_0\rangle}{\hbar\omega-(E_0-E_l^-)-i\varepsilon}, \end{aligned} \tag{A.9}$$

as shown in Equation 2.16.

## A.3 | $\omega^2$-theorem

We assume a function $f(t)$ that has a finite integral over the real axis so that its Fourier image

$$\widehat{f}(\omega) = \int_{-\infty}^{\infty} \mathrm{d}t\; e^{-i\omega t}f(t) \tag{A.10}$$

exists. Then, for the Fourier image of the derivative of $f(t)$ it holds that

$$\begin{aligned}\widehat{\frac{\mathrm{d}f}{\mathrm{d}t}}(\omega) &= \int_{-\infty}^{\infty} \mathrm{d}t\ e^{-i\omega t}\frac{\mathrm{d}f}{\mathrm{d}t} \\ &= \left[e^{-i\omega t}f(t)\right]_{-\infty}^{\infty} - \int_{-\infty}^{\infty} \mathrm{d}t\ f(t)\frac{\mathrm{d}}{\mathrm{d}t}e^{-i\omega t} \\ &= i\omega \int_{-\infty}^{\infty} \mathrm{d}t\ e^{-i\omega t}f(t) \\ &= i\omega \widehat{f}(\omega),\end{aligned} \tag{A.11}$$

which is known as the derivative theorem. Next, we define a function $g(t)$, which is has the same properties as $f(t)$ (actually, it can even be the same function). Then, for the Fourier transform of the convolution of $f * g$, we have

$$\begin{aligned}\widehat{f * g}(\omega) &= \int_{-\infty}^{\infty}\int_{-\infty}^{\infty} \mathrm{d}t\mathrm{d}\tau\ e^{-i\omega\tau}f(t)g(t+\tau) \\ &= \int_{-\infty}^{\infty}\int_{-\infty}^{\infty} \mathrm{d}t\mathrm{d}t'\ e^{-i\omega t'}e^{i\omega t}f(t)hgt') \\ &= \overline{\widehat{f}(\omega)}\widehat{g}(\omega),\end{aligned} \tag{A.12}$$

which is the convolution theorem. Now, by combination of the two theorems, we can evaluate that the Fourier image of the convolution of derivatives

$$\widehat{\frac{\mathrm{d}f}{\mathrm{d}t} * \frac{\mathrm{d}g}{\mathrm{d}t}}(\omega) = (-i\omega)(i\omega)\overline{\widehat{f}(\omega)}\widehat{g}(\omega) = \omega^2\overline{\widehat{f}(\omega)}\widehat{g}(\omega), \tag{A.13}$$

which is the $\omega^2$-theorem discussed in Chapter 2. Clearly, for the case $g = f$ the Fourier image is represented by the power spectrum $\omega^2|\widehat{f}(\omega)|^2$, which is known in the literature specifically as the Wiener–Khinchin theorem.

# B | A small experimental detour

The research presented in this thesis is theoretical. However, the research project discussed in Chapter 4 has an integral experimental component; therefore, we provide a short comment on liquid microjet XPS in this Appendix.

In XPS, a sample under ultra-high vacuum is illuminated with a beam of X-ray photons with well-defined and known energies up to several hundreds of eV, typically originating from a synchrotron light source, which liberates electrons bound inside the sample through the photoelectric effect. Measuring the kinetic energies of the outgoing electrons then allows one to map the distribution of electron binding energies (*cf.* Equation 4.1) in the sample. The measurement of condensed static samples in this way is only possible for solids since, in liquid samples, the high vapor pressure obscures the beam from efficiently reaching the bulk of the liquid. The door to bulk liquid spectra is opened by the so-called liquid microjet technique pioneered by Faubel,[53] in which a thin laminar-flowing filament of the liquid (Figure B.1) is collided with the beam, which allows measuring a combined but resolvable spectrum of the gas and liquid phases. Since its discovery, the method has been routinely used for room temperature samples; however, making a stable microjet of liquid ammonia presents an additional challenge as it needs to be maintained in its liquid window between −77 and −33 °C

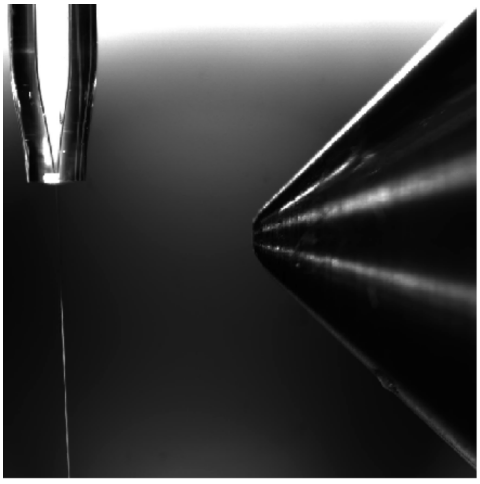

Figure B.1: A neat liquid ammonia microjet. In the top left corner, one can notice the glass nozzle from which the microjet escapes as a thin stream of liquid. To the right is the entrance to the electron analyzer, which reports the kinetic energies of the detached photoelectrons. The photography is a courtesy of Dr. H. Christian Schewe.

and thus requires a cryogenic kit. The technical solution for our purpose was developed primarily by Mason, Buttersack and Schewe[54] at the Institute of Organic Chemistry and Biochemistry of the Czech Academy of Sciences in Prague and mounted to the SOL$^3$PES experimental beamline set up built and maintained by Seidel and coworkers[55] at the BESSY II synchrotron facility[56] at the Helmholtz-Zentrum Berlin (Berlin-Adlershof research campus) where our XPS spectra were measured.

# C | Attached papers

The following Appendix contains reprints of the publications presented in the main text of this thesis and listed in the above List of Publications. Copyrighted publications without open access rights are reprinted with permission of the respective publishing houses, as detailed in each subsection.